UC San Diego

UC San Diego Electronic Theses and Dissertations

Title

Opportunities and Challenges in Silicon Photonics for Systems

Permalink

https://escholarship.org/uc/item/65d5p9rk

Author

Grant, Hannah Rae

Publication Date

2018

Peer reviewed|Thesis/dissertation

eScholarship.org Powered by the California Digital Library
University of California

UNIVERSITY OF CALIFORNIA SAN DIEGO

Opportunities and Challenges in Silicon Photonics Systems

A dissertation submitted in partial satisfaction of the
requirements for the degree
Doctor of Philosophy

in

Electrical Engineering (Photonics)

by

Hannah Rae Grant

Committee in charge:

Professor George Papen, Chair
Professor Shayan Mookherjea, Co-Chair
Professor Joseph Ford
Professor George Porter
Professor Alex Snoeren

2018

Copyright
Hannah Rae Grant, 2018
All rights reserved.

The dissertation of Hannah Rae Grant is approved, and it is acceptable in quality and form for publication on microfilm and electronically:

_____

_____

_____

_____
Co-Chair

_____
Chair

University of California, San Diego

2018

EPIGRAPH

A common mistake that people make when trying to design something completely foolproof is to underestimate the ingenuity of complete fools.

—Douglas S. Adams *Hitchhikers Guide to the Galaxy*

TABLE OF CONTENTS

LIST OF FIGURES

LIST OF TABLES

ACKNOWLEDGEMENTS

I want to thank Prof. George Papen, who became my advisor at the end of my second year my graduate school. From him, I have learned a lot about being a good researcher not just technically but also, professionally. I have also had the pleasure to take and T.A. his classes, which have been some of my favorite optics classes here at U.C. San Diego. I am very fortunate to have had the chance to be advised by him.

I want to thank Prof. Shayan Mookherjea, who took me on as an undergraduate researcher and was paramount to starting my career in silicon photonics. Aside from being my initial advisor here at UC San Diego, he stayed on as a co-advisor and has allocated me the space and tools in his Micro/Nano-Photonics Lab to conduct my research. I cannot thank him enough for his professional mentoring that has guided me over the years as well as giving me feedback on future career decisions.

My committee members are Prof. Joseph Ford, Prof. George Porter and Prof. Alex Snoeren. Each member of my committee has been very supportive to me finishing my doctoral work. Prof. Joseph Ford has been a major supporter of my completion of my doctoral work, and his passion to teach optics is truly inspiring. Both Prof. Alex Snoeren's and Prof. George Porter's feedback on my work has allowed me to reflect on the bigger picture on the impact of silicon photonics for systems.

I acknowledge my collaborators from IBM, Dr. Benjamin G. Lee and Dr. Laurent Schares, who have contributed key tools such as the IBM SiP Switch Chip for my research and have given valuable input to my research projects over the years.

I thank my labmates: Dr. Ryan Aguinaldo, Mr. Alex Forencich, Dr. Ranjeet Kumar, Ms. Jie Zhao, Mr. Xiaoxi Wang, Dr. Peter Weigel, Dr. Marc Savanier, Dr. Jung Rong Ong, Ms. Chaoxuan Ma and Mr. Forrest Valdez. Each member has been a pleasure to work with over the years. I personally thank Dr. Ryan Aguinaldo, whom I was lucky to shadow my first year and a half in graduate school. Mr. Alex Forencich deserves my many thanks as without his FPGA

expertise some of my research would not be possible.

I thank my support from the the Center of Integrated Access Networks (CIAN), which supported me for the majority of my doctoral work. CIAN has been a key player in my research, and the center has also been a source of professional development resources that I have personally benefited from. The CIAN Chip-Scale Photonics-Testing Laboratory at U.C. San Diego allowed for measurements that contributed to my research. CIAN has provided opportunities for me to collaborate with students at other universities such as U.C. Berkeley.

Thank the ECE GSC community for which was a great outlet and allowed me to find a sense of myself in this very-large department. I thank all my other friends not only at UC San Diego, but those from the University of Arizona who continuously show support for me.

I thank Mrs. Teri and Mr. Byron Conrad who have supplied me with very good fair-trade coffee for a large portion of my doctoral work. Graduate students typically run off of caffeine, but good coffee can really make a difference.

I want to thank my parents, Mrs. Eileen and Mr. Henry Grant, who instilled in me a desire to learn and a sense of dedication to my work. I doubt they initially imagined that I would one day pursue a doctoral degree. However, they have always been supportive and ensuring that my hard work will pay off.

Finally, I acknowledge my significant other, Mr. Charles Conrad. Graduate school is emotionally exhausting and time consuming, and he has been my number one fan through out all of this. He has made efforts for the past three and a half years to make our long distance relationship work when I was overwhelmed with graduate school responsibilities. Moreover, he has taught me to be more assertive of myself but also, to soften self-inflicted limitations. His support has aided me in maintaining my sanity during my doctoral work.

Thank you,

Hannah Grant

San Diego, CA

August 1, 2018

Chapter 3 in part, contains material, published in the following, of which the dissertation author was the primary investigator:
H.R. Grant, A. Forencich, G. Papen, N. Dupuis, L. Schares, R.A. Budd, and B.G. Lee, "Bit error rate measurements of a 4x4 Si-Photonic switch using synchronous and asynchronous data" *IEEE Optical Interconnects Conference (OI)*, 2016, 32-33.

Chapter 4 in part, contains material, published in the following, of which the dissertation author was the primary investigator:
H.R. Grant, G. Papen, S. Mookherjea, L. Schares and B.G. Lee, "Heuristic Model for Rapid Characterization of a SiP Switch-Chip," accepted for publication at *Journal of Lightwave Technology*, 2018.

Chapter 4 in part, contains material, published in the following, of which the dissertation author was the primary investigator:
H.R. Grant, G. Papen, S. Mookherjea, L. Schares, and B.G. Lee, "Heuristic Characterization of SiP Switches," in *Advanced Photonics Conference 2017 (PS)*, PTu3C.1.

Chapter 5 in part, contains material, published in the following, of which the dissertation author was the primary investigator:
H.R. Grant, S. Mookherjea and G. Papen, "All-Optical Barrel Shifting using Silicon Photonics," in-submission to *Journal of Lightwave Technology*, (2018).

VITA

2013	B. S. in Optical Sciences and Engineering with minors in Mathematics, University of Arizona
2010-2013	Undergraduate Student Researcher, College of Optical Sciences, University of Arizona
2012	Undergradaute Student Researcher, Micro/Nano-Photoncis Group, University of California San Dieg0
2013-2018	Graduate Student Researcher, Dept. of Electrical and Computer Engineering, University of California San Diego
2014-2017	Teaching Assistant, Dept. of Electrical and Computer Engineering, University of California San Diego
2018	Ph. D. in Electrical Engineering (Photonics), University of California San Diego

PUBLICATIONS

H. R. Grant, S. Mookherjea and G. Papen, "All-Optical Barrel Shifting using Silicon Photonics," in-preparation, (2018).

H.R. Grant, G. Papen, S. Mookherjea, L. Schares and B.G. Lee, "Heuristic Model for Rapid Characterization of a SiP Switch-Chip," accepted for publication at *Journal of Lightwave Technology*, 2018.

H.R. Grant, G. Papen, S. Mookherjea, L. Schares, and B.G. Lee, "Heuristic Characterization of SiP Switches," in *Advanced Photonics Conference 2017 (PS)*, PTu3C.1.

H. Y. Hwang, J. S. Lee, T. J. Seok, A. Forencich, H. R. Grant, D. Knutson, N. Quack, S. Han, R. S Muller, G. C Papen, M. C. Wu, and P. O'Brien, "Flip Chip Packaging of Digital Silicon Photonics MEMS Switch for Cloud Computing and Data Centre," IEEE Photonics Journal 9 (3), 1-10 (2017).

T. J. Seok, H. Y. Hwang, J. S. Lee, A. Forencich, H. R. Grant, D. Knutson, N. Quack, S. Han, R. S Muller, L. Carroll, G. C. Papen, P. O'Brien, and M. C. Wu, "12 12 packaged digital silicon photonic MEMS switches," Photonics Conference (IPC), 2016 IEEE, 629-630.

H.R.Grant, A. Forencich, G. Papen, N. Dupuis, L. Schares, R.A. Budd, and B.G. Lee, "Bit error rate measurements of a 4x4 Si-Photonic switch using synchronous and asynchronous data," *IEEE Optical Interconnects Conference (OI)*, 2016, 32-33.

R. Aguinaldo, H. R. Grant, C. DeRose, D. Trotter, A. Pomerene, A. Starbuck, and S. Mookherjea, "Silicon photonic integrated components for add, drop and VOA in a 24x10 Gbps WDM data-center network," IEEE Photonics Conference, post-deadline PD.3 (2014).

R. Aguinaldo, P.O Weigel, H. R. Grant, C. DeRose, D. Trotter, A. Pomerene, A. Starbuck, A. Tkacenko, and S. Mookherjea, "A silicon photonic channelized spectrum monitor for UCSDs multi-wavelength ring network," CLEO: Science and Innovations (OSA 2014), STu1G. 4.

R. Aguinaldo, P.O Weigel, H. R. Grant, C. DeRose, D. Trotter, A. Pomerene, A. Starbuck, and S. Mookherjea, "Characterization of a silicon-photonic multi-wavelength power monitor," *2014 Optical Interconnects Conference*, San Diego, CA, 2014, pp. 139-140.

ABSTRACT OF THE DISSERTATION

Opportunities and Challenges in Silicon Photonics Systems

by

Hannah Rae Grant

Doctor of Philosophy in Electrical Engineering (Photonics)

University of California, San Diego, 2018

Professor George Papen, Chair
Professor Shayan Mookherjea, Co-Chair

Silicon photonics has become a key solution to tackle the demands on current communication systems and information processing because the use of this platform can reduce power consumption, eliminate electrical to optical conversion and leverage mature CMOS fabrication techniques. As silicon photonic devices are introduced into system-level applications, new challenges need to be addressed. This thesis will present some solutions to these challenges. These challenges range from device design and functionality to the post-processing and testing of silicon photonic devices. First, the system-level testing of a silicon photonic switch with crosstalk using real Ethernet datastreams is presented. Next, a rapid characterization technique for post-

processing of silicon photonic switches is shown. Finally, the functionality of barrel shifting is demonstrated in silicon photonics. The challenges and the solutions presented in this thesis are key steps to realizing the promise of system-level applications of silicon photonic devices.

Chapter 1

Introduction

Silicon photonics (SiP) is an emerging device platform that combines photons and electrons for cost-effective solutions for system-level applications. While utilizing optics for large-bandwidth, power-conserving solutions has been known, SiP has additional benefits that make the platform potentially cost-effective and competitive. First, SiP devices are much smaller than bulk optical components. This alleviates the costly issues that come from operating and cooling bulk optical components. Next, SiP is an integrated platform that combines CMOS with photonics. This means SiP can utilize a highly scalable CMOS fabrication process with well-established foundries [1]. Additionally, multi-project wafers have allowed broad access of SiP fabrication for prototyping and R&D [1–3]. The compatibility with CMOS processing makes monolithic integration of SiP with electronics possible [4]. By leveraging current CMOS processing, this can lead to monolithic integration of system-level functionalities with electronic control [5–9]. As SiP device technology matures, a deeper understanding of the system-level aspects of SiP is required. That is the topic of this thesis.

There exists a broad spectrum of system-level applications for SiP devices. With the advent of ”big data” and the Internet of Things (IoT), there is a demand for large bandwidth optical interconnect solutions in communication and information processing systems [10]. This

has led to SiP becoming an important technology that can address the bandwidth bottleneck occurring in communication systems [11–16] and information processing [17]. SiP has also been implemented for high capacity computing [18, 19] and sensing applications such as lidar [20].

Given the broad scope of SiP devices for optical communication systems and information processing, there are opportunities and challenges that need to be addressed. These system-level opportunities and challenges can be characterized into four broad categories: design & fabrication, packaging, system-level testing, and characterization & post-processing. Each challenge must be overcome for the widespread use of SiP in system-level applications. This thesis discusses several of these challenges and presents promising methods to overcome some of these issues.

1.1 Design and Fabrication

Design & fabrication addresses device design and fabrication techniques. While there is a large body of research in this area [1, 6, 7], there are still major challenges in the fabrication processes, design platforms, and specific device design for system-level applications.

The fundamental value proposition of SiP is that it can leverage mature fabrication processes using lower resolution CMOS processing compared to current state-of-the-art microelectronic chips [21]. However, the existing fabrication techniques for high-quality electronic devices do not necessarily realize high-quality optical devices in large volumes [1]. Monolithic integration of CMOS with photonics in SiP devices is strongly dependent on the design rules of the specific fabrication processes leading to devices that currently have to be post-processed to achieve high-yield [4, 22].

Mature design platforms that support complex simulations of photonic devices exist and is commonly utilized [1, 23, 24]. However, design and fabrication software that are common to CMOS processing such as layout versus schematic (LVS) tools are still being developed to

streamline the design-to-fabrication process of SiP devices [25, 26].

There also exists a range of challenges for devices designed and fabricated for system-level applications. These challenges include the design of microrings to mitigate crosstalk [27] to the design of polarization insensitive devices [28]. Additionally, optimized system-level design of SiP devices requires a co-optimization between the functions implemented in photonics and the functions implemented in electronics so that the limitations of one technology can be overcome by the other technology [29].

This challenge presents an opportunity to explore linear optical transformations in SiP for signal-processing systems [30]. As electronic functionalities are reaching their limits in terms of bandwidth and power consumption, exploring optical implementations of key functionalities is evident. The implementation of these functionalities lead to new design and fabrication challenges. One of these functionalities, called barrel shifting, is explored in a SiP platform in Chapter 5.

1.2 Packaging

Packaging is not specifically addressed in this thesis, but it plays a major role in system-level implementations of SiP devices. This section provides a brief overview of these challenges.

Cost-effective robust packaging is required for SiP devices to be marketable. In order for silicon photonics to be a viable platform, there is a requirement for the automation of packaging [31]. Major problems in packaging are high-volume optical connections, thermal stability, and proper packaging of electronic components [32–35].

Most commercial SiP devices are transceivers [16, 36]. Typically electronic connections are provided by wire-bonded or flip-chip bonded to an electrical PCB [35]. Optical connections are typically provided by grating-couplers. Grating couplers are less sensitive to misalignment compared to edge-coupling [35]. However, grating couplers are wavelength selective making

their use for large spectral-bandwidth solutions difficult. To solve the issue of spectral bandwidth, development of packaged edge-coupled fibers and fiber arrays for low-loss, high-volume packaging has been on-going area of research and development [31, 35, 37]. The sensitivity to misalignment for edge-coupling makes high-volume manufacturing difficult. Solutions are being developed to address this issue [38, 39].

Thermal stability is also a major issue in the packaging of SiP devices [17]. Because some SiP devices use the large thermally-induced change in the refractive index [1], the devices must be packaged such that external temperature fluctuations do not alter the operation of the device. Packaging with thermal electric coolers (TEC) is becoming more common. However, these components add to the over all power and cost of the device.

1.3 System-Level Testing

System-level testing is required to validate the device functionality in a system-level environment. System-level testing procedures have been developed for SiP devices such as transceivers and variable-optical-attenuators (VOAs) [16, 36, 40]. Devices such as SiP switches are more difficult to test for system-level performance due to large port counts and crosstalk sensitivity. To date, most of the characterization of SiP switches has been at a device level measuring crosstalk power or measuring the bit error rate (BER) of a single channel without considering the additional interference from other channels. Specifically, there are few studies of the effect of interference within a switch-chip on the BER performance of a SiP switch-chip under real Ethernet traffic. For SiP switch-chips, this measurement can be difficult as significant calibration is required to ensure proper testing. Chapter 3 of this thesis will present the characterization of a SiP switch-chip for crosstalk generated from clock-synchronous or clock-asynchronous operation. This study underscores the importance of a system parameter such as the type of clocking on the switch performance as quantified by the crosstalk.

1.4 Characterization and Post-Processing

Characterization & post-processing is essential for SiP devices to enter the market. Previously, these functions were done on a small scale in research laboratories. It has been shown that high-volume characterization techniques for photonic devices are currently expensive [41]. While some characterization techniques used for CMOS characterization can be used for SiP [1], there is a need for scalable optical characterization techniques [42–45]. Wafer-level optical characterization is enabled when using grating-couplers, but these components have limited spatial bandwidth and high losses [1]. In some instances, brute-force characterization techniques have been implemented, but these are not scalable [42, 43]. Cost-effective and scalable characterization techniques for large-port count SiP devices is a critical requirement for wide-spread use of SiP in systems. Chapter 4 presents a simple solution for the rapid characterization of planar SiP switch-chips.

1.5 Conclusion

This thesis presents several approaches to overcome key challenges for system-level applications of SiP. Chapter 2 describes current figures-of-merit for system applications and describes current figures-of-merit for SiP devices. Chapter 3 presents a system-level characterization of a SiP switch using real Ethernet data of the crosstalk. Chapter 4 presents a methodology for rapid characterization of SiP switches. Chapter 5 presents an optical implementation of barrel shifting in a SiP platform. The combined impact of this work leads to an improved understanding for the design, system-level testing, and characterization & post processing of SiP devices for system-level applications.

Chapter 2

Background

This chapter presents background material for SiP devices designed for system-level applications. First, several system-level figures-of-merit are discussed, focusing on optical interconnects and switching. Similar figures-of-merit apply to other system-level applications. Next, device-level figures-of-merit are discussed for optical communication systems.

2.1 System-Level Figures-of-Merit

There are several key figures-of-merit that apply to the majority of optically-switched network architectures. These figures-of-merit are optical link budget, power consumption, scalability, and throughput.

2.1.1 Optical Link Budget

Optical link budget is a calculation of the total optical power required for a reliable link and includes all losses. The optical link budget is calculated for each data rate over a set distance in a given fiber. For example, the standard 100GBASE-LR4 has a maximum link budget of $-8.6\,\mathrm{dB}$ for a distance of $10\,\mathrm{km}$ and 100GBASE-ER4 has a maximum link budget of $-21.4\,\mathrm{dB}$

for a distance of 40 km [46]. Since this is the overall budget for an optical link, components with higher losses can be balanced with lower-loss components or higher-power input sources. However, compensating for higher-loss components leads to higher power consumption.

2.1.2 Power Consumption

Power consumption is the total power required to operate and maintain a communication system. The dominant source of power consumption in conventional communication systems is the electrical-to-optical (EO) and optical-to-electrical (OE) conversion [47, 48] and the clock-data recovery circuits. Optical solutions using either bulk-optical components or SiP components can eliminate EO/OE conversion to reduce power consumption in communication systems [21, 49–52]. This is particularly important as faceplate power densities in data centers are becoming a major issue at 400G where conventional transceiver designs lead to a max power consumption of 16 W [53, 54]. Reducing the amount of power consumption at the faceplate is a key opportunity for SiP.

2.1.3 Throughput

Throughput is how much data can be transported between the desired end-points of a system per unit time [55]. Two major factors contribute to the throughput in an optically-switched network: the bandwidth and the duty cycle. Bandwidth is the average rate in which data is transferred. The duty cycle is the fraction of time the switch remains in a state compared to the overall cycle of the switch. The product of these two factors is the communication system throughput. A large throughput requires large bandwidth with a high duty cycle.

The bandwidth is typically the bisection bandwidth, which is the bandwidth between two partitions of a communication system. Optical components are advantageous for low-loss, high-data-rate systems. In comparison, electronic components can have high loss for increasing

bandwidths. Bulk optical components and fibers are commonly used in data centers [52, 56]. For example, Google's Jupiter data center, which already leverages optics, in 2012 reported a bisection bandwidth of $1.3\,\mathrm{Pbit\,s^{-1}}$ [52]. The push for SiP devices to replace current bulk-optical components is driven by the reduction in power consumption (cf. Section 2.1.2).

The duty cycle is also affected by the reconfiguration time. The reconfiguration time is the time a switch is change state. A fast reconfiguration time leads to a higher duty cycle and a larger throughput. A fast reconfiguration time also leads to lower latency in the network.

2.1.4 Scalability

As a system grows larger, the characteristics of the devices may change affecting the scalability of the system. For example, the port-to-port loss of an optical switch is a function of the number of ports (or the radix) of the switch. Generally, each physical-layer component of a communication system needs to effectively scale for the overall system to scale. Scalability is dependent on device-level parameters such as loss, crosstalk and power consumption. Each of these device figures-of-merit is discussed separately.

2.2 Device-Level figures-of-merit

Key figures-of-merit for SiP devices are loss, modulation bandwidth, crosstalk, and spectral bandwidth.

2.2.1 Loss

Loss plays a major role in the ability to use SiP devices at a system-level. Loss can occur on the device, which is referred to as on-chip loss, or at the coupling interfaces, which is referred to as off-chip loss. On-chip loss and off-chip loss will be discussed separately.

On-Chip Losses

The predominant on-chip loss is the loss per unit length α in inverse meters, which leads to the total loss a over the optical path length given by

$$a = \exp(-\alpha * L) \tag{2.1}$$

where L is the total optical path length in meters [57]. The dominant mechanism for propagation loss is surface scattering. Typically, the propagation loss is $2-3\,\mathrm{dB\,m^{-1}}$ for standard CMOS processing [1]. Additional on-chip losses can occur from bends [5] and dopant implantation [58].

Off-Chip Losses

Appendix A addresses various coupling losses for different SiP platforms. This section provides an overview of the current state-of-the-art for coupling losses.

The predominant off-chip loss is the coupling loss between the off-chip optics, such as an optical fiber, and the SiP device. Coupling optics are required to direct light on and off a device. Typical optical coupling components used are optical fibers or arrays of optical fibers. Coupling losses directly affect the cost of incorporating SiP devices into a system.

Currently, there are two classes of solutions for low-loss coupling. Coupling losses on the order of $-1.5\,\mathrm{dB}$ at 1550 nm using a standard 220 nm silicon-on-insulator (SOI) platform have been shown. The best performance is edge-coupling using Si_3Ni_4 layers to create a taper at the edge of the SOI die, which resulted in a coupling loss of $-0.5\,\mathrm{dB}$ at 1550 nm for a range 100 µm [59]. While this was shown using a 220 nm platform, the amount of post-processing to achieve this loss is not typically compatible with wafer-level fabrication. A grating coupler using a 260 nm platform was shown to have $-0.9\,\mathrm{dB}$ of loss with a 38.8 nm range of operate at 1550 nm [60]. Were a 220 nm platform used, this grating coupler would have an expected loss of $-1.5\,\mathrm{dB}$ loss.

The most robust solution has been shown by IBM Beauxmont [38, 39] where a slot v-groove is created on the SI die to allow to place the coupling optic and a polymer lid is used to seal the structures into place. While this solution is costly in terms of required die space, it reproducibly yields losses of $-1.3\,\text{dB}$ of loss at $1310\,\text{nm}$ and $-1.4\,\text{dB}$ at $1550\,\text{nm}$.

Given these state-of-the-art coupling solutions, the best edge-coupling is around $-1.5\,\text{dB}/\text{facet}$. This means there is a total of $-3\,\text{dB}$ for on/off chip coupling. Comparing this to the optical link budgets mentioned in Section 2.1.1 leaves $-5.6\,\text{dB}$ of optical link budget for a 100GBASE-LR4 transceiver. This calculation neglects any on-chip losses. More conventional solutions suffer from higher coupling losses, which are presented in Appendix A.

2.2.2 Modulation Bandwidth/Switch Time

The modulation bandwidth is a key figure of merit for active components. Communication system components such as transmitters require high modulation bandwidth. SiP offers significant advantages for high-speed optical communications and processing. These devices can use the electric-optic effect [58, 61–65] for high speed operation. The current state-of-the-art planar SiP optical switch utilizes carrier-depletion with Mach-Zehnder interferometers. This leads to switching times on the order of $1\,\text{ns}$ [64].

2.2.3 Crosstalk

Crosstalk describes the amount of energy coupled from one channel of a device to another channel of a device. Crosstalk is an inherent property of devices based on mode coupling. When crosstalk is treated as noise, crosstalk can significantly reduce the optical-signal-to-noise-ratio (OSNR) leading to detection error. Fig. 2.1 shows an example of crosstalk on a signal channel. As shown, a crosstalk signal is called an aggressor, and the desired output is called the signal channel.

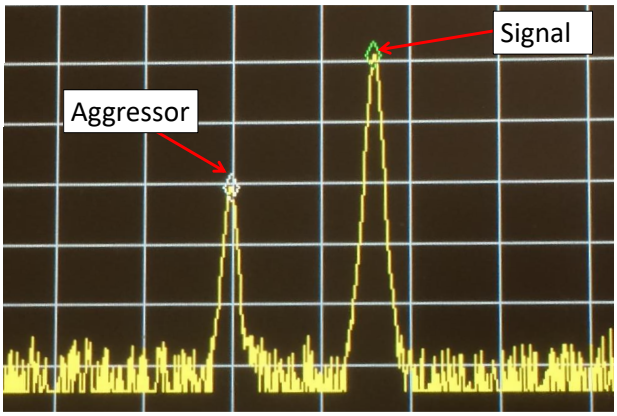

Figure 2.1: Crosstalk Example: a signal channel being afflicted by an aggressor.

Different SiP structures lead to different levels of crosstalk. For a single standard Mach-Zehnder interferometer, the best reported crosstalk is $-27\,\text{dB}$ [66]. The crosstalk can be improved by incorporating tunable couplers [67] or using nested Mach-Zehnder interferometers [68]. For microring resonators, a second-order coupled microring have been reported to achieve crosstalk on the order of $-50\,\text{dB}$ to $-70\,\text{dB}$ [29, 61, 69, 70]. The trade-offs of using higher-order coupled microrings are discussed in detail in Chapter 5.

2.2.4 Spectral Bandwidth

The spectral bandwidth is the operational frequency (or wavelength) range of the device. It is typically a specification of the system. For communication system architectures, wavelengths are chosen from an International Telecommunication Union's (ITU) Telecommunication Standardization Sector (ITU-T) frequency grid [71].

Typically a SiP Mach-Zehnder interferometer will have a large passive spectral bandwidth on the order of $30\,\text{nm}$ [66]. On the other hand, a microring resonator will have a much narrower spectral bandwidth on the order of $1\,\text{nm}$ [63, 69, 72, 73].

Chapter 3

System-Level Testing of a Silicon Photonic Switch-Chip

A major issue for commercially-viable SiP devices is the development of system-level testing. This chapter discusses a specific system-level testing methodology for a SiP switch-chip.

Conventionally, the characterization of a SiP switch-chip has been at the device level. This characterization measured the crosstalk power and bit error rate (BER) of a single channel without additional interference using test patterns that were not real data. Instead, this chapter presents the first characterization of a SiP switch-chip for crosstalk using $10\,\mathrm{Gbit\,s^{-1}}$ Ethernet frames for clock-synchronous and clock-asynchronous operation. The key contribution of this work is providing a deeper understanding of how the crosstalk and BER of a switch-chip is affected by system-level parameters such as the type of clocking.

3.1 Experimental Setup and Measurements

The experimental set-up is shown in Figure 3.1. The experiments used four 10 Gb/s ethernet data streams generated in a Virtex-6 FPGA development board. The channel under test

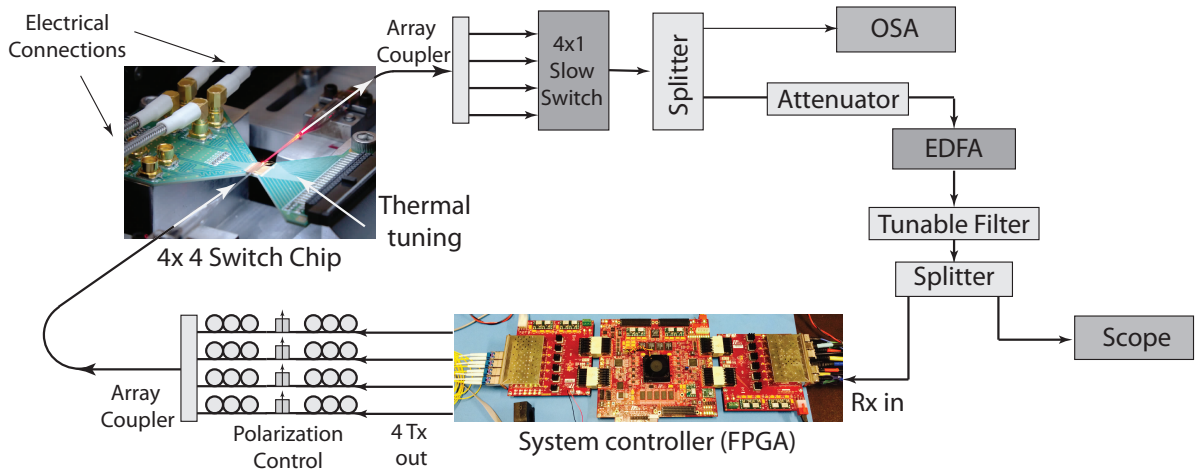

Figure 3.1: Experimental setup.

consisted of Ethernet frames filled with a PRBS sequence, while the aggressors were 64b/66b idles. One of the four channels is utilized for system level bit error rate and packet loss rate measurements from the FPGA, which generates 1000 byte Ethernet frames consisting of a 4 byte sequence number and 996 bytes of a PRBS, attaches a standard Ethernet FCS, then 64b/66b encodes and transmits the data with a standard 10GBASE-R PHY. On the receive side, the frame check sequence (FCS) is used to determine good packets. Frames with an invalid FCS are saved for BER analysis.

For the 64b/66b code, any single bit error at the receiver produces two additional errors after decoding, any of which may fall outside of the frame. Therefore, a compensation method to remove these duplicates was developed, differing from the true BER by a worst case value of 0.73%. By utilizing multiple 10G network interface cards, clock-synchronous or -asynchronous driven data is achieved.

For the experiments, one signal datastream and three agressor datastreams were used to drive a separate SFP+ module at one of four wavelengths (1563.05nm, 1563.77nm, 1564.60nm, 1565.42nm), each input to a port on the switch. The switch is fabricated at the Institute of Microelectronics, Singapore, using a standard 220-nm thick silicon photonic platform. The switch consists of four directional-coupler-based Mach Zehnder interferometers (MZI) arranged

in a butterfly topology with a center wavelength near 1565 nm. Each of the eight MZI arms employ a low-speed thermo-optic (TO) tuner and a nanosecond-scale carrier-injection based p-i-n diode phase shifter. For this work, only the TO tuners are used. The polarization input to the switch was controlled using a combination of polarization controllers and in-line polarizers. Custom array couplers were aligned to the input and output ports of the switch chip using a 6-axis stage [74]. The four spatial channels had a uniform loss of 11.0 ± 1.2 dB, including 6 dB of loss in the couplers.

The 4×4 switch has sixteen switch configurations, of which three were used for testing. For the first and second configuration, all of the 2×2 MZI units within the switch chip are set to the through state or to the cross state. The third configuration was a combination of states such that the datastreams interact first with a through state MZI then with a cross state MZI.

Using a slow mechanical switch, each output port of the switch chip can be routed into the measurement suite shown in Figure 3.1. The OSA is used for crosstalk measurements. After fixed amplification, attenuation and filtering, the signal is split with one port sent to a limiting amplifier SFP+ module on the FPGA for BER measurements, and the second port is sent to measure the eye-pattern on an oscilloscope using a linear detector. Due to the fact that we are operating with regards to the limiting amplifier in the SFP+ modules, there will be some noise not accounted for on the Oscilloscope measurements. The BER measurements were calibrated to the eye-patterns using a two-step process. The first step was a loopback mode without the switch chip or the optical amplifier. The value of the BER measured using the FPGA was compared to the values of the Q-factor measured for the same module using an evaluation board that exposed the electrical output of the SFP+ module. In the next step, the EDFA was added to account for the optical amplifier and to ensure that the amplifier was saturated.

Table 3.1: Switch Chip Insertion Loss.

Input Channel	Insertion Loss (dBm)
Channel 1	-4.89
Channel 2	-6.89
Channel 3	-7.00
Channel 4	-7.2

Table 3.2: Signal and crosstalk power of synchronous data for three switch configurations.

Switch state	**Through**	**Mixed**	**Cross**	**Through (One channel)**
Test Signal (dBm)	-14.8	-14.1	-15.0	-11.6
Aggressor 1 (dBm)	-41.6	-44.8	-30.3	NA
Aggressor 2 (dBm)	-54.0	-37.1	-51.2	NA
Aggressor 3 (dBm)	-40.9	-43.5	-46.2	NA

3.1.1 Results

Figure 3.2 shows the measured BER vs. OMA for the clock-synchronous and the clock-asynchronous datastreams. The leftmost curve for each plot is a baseline BER measurement for a single input with no aggressors for the "all-through" configuration of the switch. The other three curves shown are for the three switch configurations (all-through, all-cross and mixed) with three additional aggressor datastreams that produce crosstalk within the first channel. The all-cross curve reached a power budget limitation at an OMA of about -12 dBm precluding lower BER characterization. The corresponding insertion loss, and the crosstalk values for each of these cases are tabulated in Table 3.2 and Table 3.3. To determine if the crosstalk power can be used to predict the BER, another set of experiments was run using a single aggressor. For this test, the measured crosstalk power was divided by the OMA to derive a normalized crosstalk power. This value was then varied by changing the switch state.

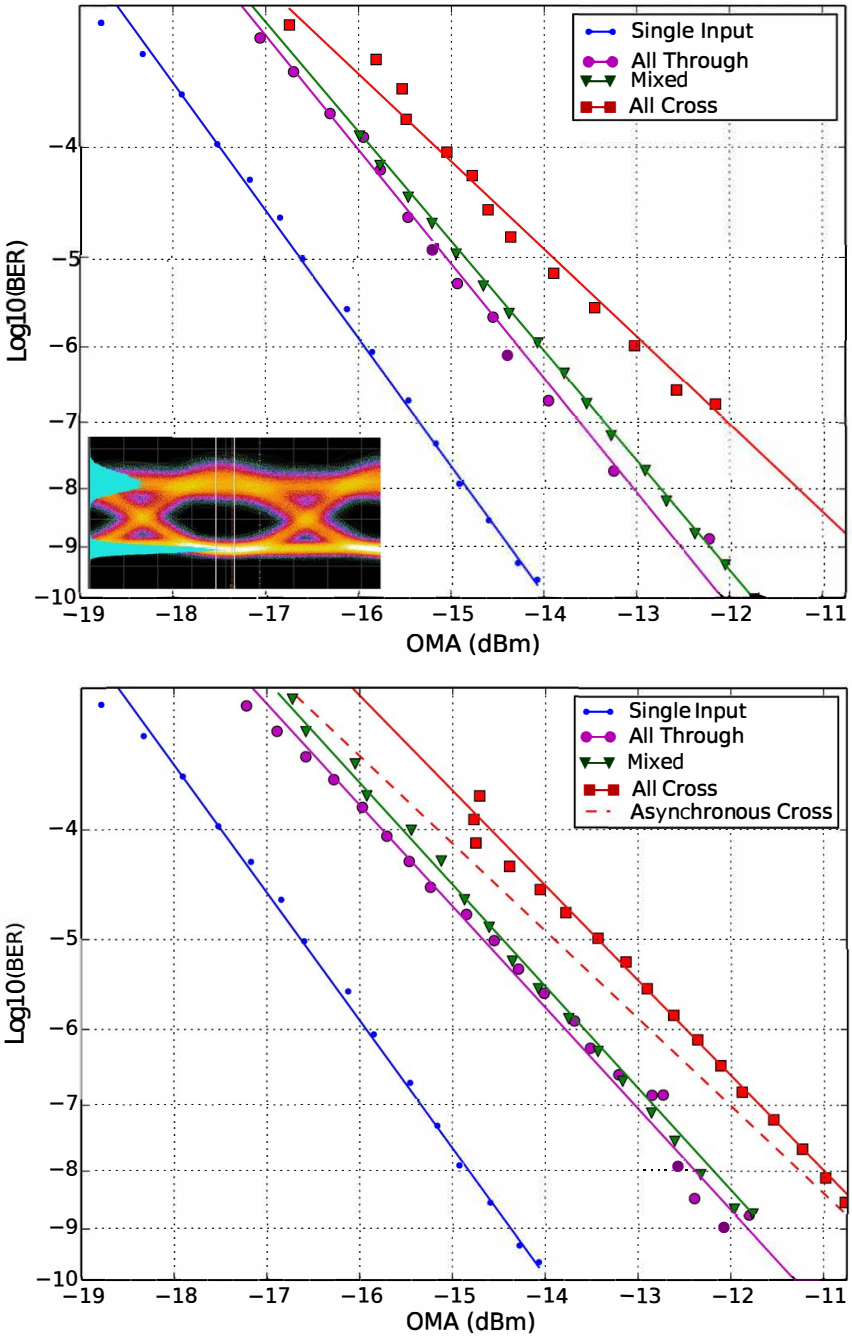

Figure 3.2: BER vs. optical modulation amplitude (OMA) for datastreams at several switch-states. Top: synchronous data with an inset of the Eye Diagram for all-through state at a BER of 10^{-6}. Bottom: asynchronous data. Also shown is the synchronous data (dashed line) for the all-cross state.

Table 3.3: Signal and crosstalk power of Asynchronous data for three switch configurations.

Switch state	Through	Mixed	Cross	Through (One channel)
Test Signal	-16.5	-14.1	-15.6	-11.6
Aggressor 1	-42.8	-44.8	-34.6	NA
Aggressor 2	-52.4	-37.1	-53.0	NA
Aggressor 3	-37.2	-43.5	-44.2	NA

3.2 Discussion

Examining the synchronous data in Figure 3.2 in a low error rate regime, the power penalty is about 3 dB from no aggressors to three aggressors for the all-cross state with -15.3 dB of crosstalk. The penalty is reduced to about 1.5 dB for the all-through state that has -26 dB of crosstalk. The difference in crosstalk between the all-through state and all-cross state is attributed to the limited bandwidth of the MZI directional couplers, which can be alleviated using more complex coupler designs. Similar trends are seen for the asynchronous data in the bottom of Figure 3.2.

Comparing the two different forms of clocking, there is a slight additional penalty for asynchronous clocking compared to synchronous clocking. This could be a result of a beneficial phase relationship between the victim and aggressor channels for the synchronous case. This offset can be seen in the bottom of Figure 3.2 where the BER curve for synchronous clocking using the all-cross switch state is shown as a dashed line. Additionally, synchronous clocking adds a noise power interference term that can be seen as a change in slope of the BER.

The slope of the BER curves changes as the amount of crosstalk is varied with this change being more pronounced for larger values of the crosstalk. This result indicates that the effect of the crosstalk cannot be modeled as a simple power penalty. The amount of slope change for asynchronous versus synchronous varies as well with the synchronous case producing a greater change in slope. The variance in the change of slopes can be seen for the all-cross switch state

in Figure 3.2. It can be seen that for the asynchronous case, the crosstalk adds as a noise power when the crosstalk is increased (Figure 3.2). For the synchronous case, the addition of crosstalk does not simply add as crosstalk noise power, but now has some noise power interference term. This is seen as a change in slope of the BER.

3.3 Conclusion

These initial results demonstrate that a deeper understanding of the requirements for crosstalk in scaled multi-stage switch fabrics in system-level networks and the relationship between those requirements and the particular data patterns of the network, is essential to the realization of this technology, and he experimental characterization of the BER for an optical switch chip as a function of the switch state and the crosstalk power is essential to the development of networks that use optical switching. The work presented in this chapter is one step towards achieving this required understanding, and emphasizes the importance of optimizing nanosecond photonic switches for the lowest possible crosstalk over a broad spectral range. The degree of complexity that is attributed to system-level testing of large port-count, silicon photonic switches emphasizes the uniqueness of the work presented in this chapter.

Chapter 3 in part, contains material, published in the following, of which the dissertation author was the primary investigator:
H.R. Grant, A. Forencich, G. Papen, N. Dupuis, L. Schares, R.A. Budd, and B.G. Lee, ”Bit error rate measurements of a 4x4 Si-Photonic switch using synchronous and asynchronous data” *IEEE Optical Interconnects Conference (OI)*, 2016, 32-33.

Chapter 4

High-Yield Characterization of Mach-Zehnder-based Silicon Photonic Switches

This chapter presents a novel method to characterize and post-process silicon photonics devices to provide higher-yield for system-level applications [9, 33, 41, 75]. This method addresses the challenge of rapid characterization of high port count silicon photonic switches to accurately predict system-level performance before the costly process of packaging.

While many characterization techniques have been developed for radio-frequency components used in mobile handsets, the end-to-end design of silicon photonic devices including high-volume testing and calibration techniques to "tune" devices after fabrication so as to realize targeted system-level metrics is lacking. Some approaches for the characterization of SiP switch-chips use brute-force techniques that do not scale to large port count switches [42, 43]. The development of a simple method to aid in the characterization process is developed in this chapter using a specific silicon photonic switch. The key contribution of this work is providing a simple methodology to characterize and model silicon photonic switch-chips to predict

system-level performance.

4.1 Model Motivation

When developing a practical model for predicting system-level performance of a device, there is an inevitable trade-off between the level of abstraction of the physics to the level of complexity of the model. Ideally, the desired model should fully characterize the physics of a device, but exhaustive physical-level models are difficult to develop. On the other hand, a model that is defined by arbitrary fit parameters results in limited functionality for the prediction of system-level performance. Practical models must balance these two goals.

Modeling a complex device with multiple active structures that have a nonlinear behavior can be difficult. Previous work has been done to explore the nonlinearty voltage dependence in the Mach-Zehnder interferometer transfer function [76–78]. This chapter demonstrates the modeling of an optical switch based on Mach-Zehnder interferometers in which the parameter extraction for the model does not use voltages corresponding to a switch-state. Instead, an intermediate quadrature point with a nearly linear response is used to obtain a robust fit that can accurately predict the performance of an actual switch-state. This method is based on the sinusoidal dependence of the power as a function of the phase $\Delta\phi$ of a switch that uses Mach-Zehnder interferometers. A through or cross switch-state is obtained when $\sin^2(\Delta\phi/2)$ equals zero or one, which is at an extremum of the $\sin^2(\Delta\phi/2)$ function. At an extremum, the derivative is zero. This behavior is undesirable for the purpose of parameter extraction. An intermediate switch-state at the quadrature point is obtained when $\Delta\phi = \pi/2$ such that $\sin^2(\Delta\phi/2) = 1/2$. The derivative at a quadrature point with a positive slope is one. This linear behavior means that using model parameters extracted using a quadrature point can lead to a more robust fit.

Here, we present a heuristic model derived from a transfer matrix model, which itself is an abstraction of the device physics based on the transmission and reflection coefficients.

Parameter extraction via transfer matrix models have been commonly used to characterize silicon photonic devices [79–83], but these studies have all been for single component devices with limited complexity. Additionally, it has been shown that heuristic transfer matrix models can easily be established for silicon photonic devices [44]. Because it is based on simple matrices, this model is computationally efficient compared to numerical methods such as Finite-Difference Time-Domain (FDTD) modeling. A transfer matrix based model also permits for a hierarchical design of a multi-component device. However, as is the case for all abstractions, some physics is lost because the model depends on a plane-wave approximation for the modes. Moreover, because of the limited number of parameters that can realistically be varied and fit, an in-depth analysis of the root cause of fabrication errors may not be possible. Nevertheless, this simple model can be developed with a restricted set of measurements for initial characterization so as to predict the system-level performance of a SiP switch-chip. The initial characterization and predictions from this model can be used in conjunction with more detailed measurements.

4.2 Model Description

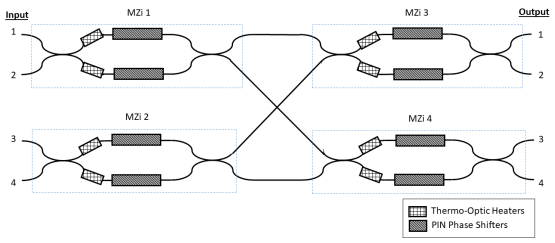

Figure 4.1: Input and output configuration of an optical switch-chip composed of Mach-Zehnder interferometers (MZi) in a butterfly topology.

The heuristic model described in this chapter is a transfer matrix model, which uses a combination of physical parameters as well as heuristic parameters to balance the complexity and the functionality of the model. The device used to develop the model is a 4×4 SiP switch-

chip fabricated at the Institute of Microelectronics (IME-A*STAR) Singapore using a standard 220 nm thick SiP platform [45]. The switch consists of four directional-coupler-based Mach-Zehnder interferometers (MZi) arranged in a butterfly topology as shown in Figure 4.1. Each MZi has two directional couplers. To switch an input port to an output port, each MZi utilizes one thermal resistive heater on each arm and one current injection phase shifter on each arm. For the purposes of this chapter, only the two thermal heating elements for each MZi are used because they set the optimal bias point for the switch compensating for any fabrication errors. The use of thermal heating elements means the overall phase shift in each MZi will depend on the applied thermal power which translates to a squared relation to the biasing voltages V^2. The determination of the bias voltages is a key goal of the predicted outcomes of the model.

In a passive switch-state with no applied voltage, the optical path length difference between the arms of each MZi is designed to be $\lambda/4$. This means that an ideally-fabricated device designed to operate at a quadrature point would couple an equal fraction of the power at each input port to each output port. A unicast switch state, in which only one output port has the desired signal will be considered later.

The heuristic transfer matrix model [66] for the passive switch-state uses a single average wavelength-dependent coupling coefficient term $\kappa(\lambda)_{\text{avg}}$ to describe the directional couplers in every MZI. The switching behavior is modeled using a separate wavelength-dependent phase shift $\Delta\phi_n(\lambda, V = 0)$ at zero bias voltage V for each of the four MZis. Four phase parameters are used because the phase is a sensitive function of process variations. The parameter $\Delta\phi_n$ is the estimate of the actual phase of each MZi. Each of the four MZis also has a separate wavelength independent excess loss term α_n. This gives nine parameters for the passive switch-state model of which five parameters are wavelength dependent. The parameters for the passive switch-state model are augmented with several additional parameters to model an active switch-state in which a non-zero voltage is applied to one or more MZis. Small variations due to thermal effects caused by biasing can be accommodated within the active switch-state model. This voltage dependence

is parameterized by a voltage-dependent differential phase $\Delta\phi_n(\lambda, V)$ for each MZi. This gives four additional wavelength-dependent parameters for the active switch-state model.

The passive switch-state model also has a wavelength-independent excess loss parameter α_n for each MZi where $n = 1, ..., 4$. To ensure a robust fit algorithm, an appropriate functional form is used to describe the wavelength dependence of each parameter as described below.

4.2.1 Coupling Coefficient

The wavelength-dependent coupling coefficient $\kappa(\lambda)$ describes the fraction of the power coupled from one waveguide to another waveguide in a single directional coupler. This coefficient depends on several geometrical parameters. Using coupled-mode theory [84], the functional form of the wavelength-dependent coupling coefficient $\kappa(\lambda)$ is

$$\kappa(\lambda) = \sin\left(\frac{\pi}{2}\frac{L}{L_C(\lambda)}\right)^2, \tag{4.1}$$

where L is the length of the interaction region and $L_C(\lambda)$ is a wavelength-dependent length that depends on the geometry. When $L = L_C(\lambda)/2$, $\kappa(\lambda) = 1/2$. Therefore, $L_C(\lambda)$ is called the crossover length. Over this length, the power transfers from one path to the other path. The crossover length $L_C(\lambda)$ corresponds to the difference of the propagation constants for the symmetric and anti-symmetric modes in the structure [84]. The functional form for $L_C(\lambda)$ is estimated from a numerical solution using a 2D FDTD model of the device as the wavelength λ is varied over the desired range about the design wavelength. The fabrication fluctuations in the coupling regions over a single device are presumed to be small such that a single average coupling coefficient is used in the model where $L = L_C(\lambda)/2$. This was motivated to allow for the model to effectively scale for larger port count devices. Were each 3 dB coupler were fit with a unique L_C, a minimum of seven additional parameters would need to be added to the model, thus, increasing computational time and possibly affecting convergence. The numerical solution

for an average coupling coefficient is parameterized by three ratios as discussed in Appendix B. This appendix also discusses the validity of using an average coupling coefficient.

Parameterized Average Coupling Coefficient

4.2.2 Differential Phase

The second parameter is the differential phase at zero bias voltage where $\Delta\phi_n(\lambda) = 2\pi n(\lambda)\Delta L\Gamma/\lambda$ and ΔL is the overall path length difference. The wavelength-dependent differential phase $\Delta\phi_n(\lambda, V = 0)$ for each of the four MZis is approximated as the sum of a wavelength-independent phase offset $\Delta\phi_n$ and a linear term $d\phi/d\lambda$ as given by

$$\Delta\phi_n(\lambda, 0) = \Delta\phi_n + \frac{d\phi}{d\lambda}\lambda. \tag{4.2}$$

For the passive switch-state, no voltage is applied to the MZi. Therefore $V = 0$, and the model uses only a single slope $d\phi/d\lambda$ for all four MZis. Over a 100 nm range, the wavelength dependence when treated as a linear approximation results in a .11% error in the phase compared to the exact functional form for the phase, $\Delta\phi_n(\lambda) = 2\pi n(\lambda)\Delta L\Gamma/\lambda$. Given that the MZi was designed such that $\Delta L = \lambda/4$, fitting the overall phase difference was deemed to be easier then fitting ΔL even though ΔL represents a physical length. The details of this approach are discussed in Appendix C.

4.2.3 Biasing Voltages

The switching behavior for the ratio of intensity input to intensity output $I_n(V)/I_{\text{in}} = \cos^2(\Delta\phi_n(V)/2)$ of the nth MZi as a function of the voltage dependent phase offset is

$$\frac{\Delta\phi_n(V)}{2} = \frac{\pi}{2}\left(\frac{V}{V_{\pi n}}\right)^2 + \frac{\Delta\phi_n}{2}, \tag{4.3}$$

where $n = 1, ..., 4$, where V_π is the voltage required to generate a π phase shift between the two arms, where $\Delta\phi_n$ is the passive offset phase for each MZi in isolation, and where $\Delta\phi_n(V)$ is the active offset phase for each MZi in isolation when a voltage is applied. It is important to reiterate that the voltage-dependent offset phase is induced by the thermal-optic effect. This means that the phase shift is proportional to the electrical power, or equivalently, proportional to V^2 where V is the applied voltage. For a device designed to operate at the quadrature point with no voltage applied is $\Delta\phi_n = \pi/2$ and $I_n(V = 0)/I_{\text{in}} = 1/2$. Using this expression in Equation 4.3, V_π can be derived as discussed below.

In addition to the passive switch-state parameters that are used to characterize the device, there are several voltage-dependent parameters for the active switch-state model. The nth MZi in an active switch state ($V \neq 0$) is characterized by a wavelength-dependent differential phase $\Delta\phi_n(\lambda, V)$. Similar to the approximation for the differential phase in the passive switch-state for which $V = 0$, each differential phase term $\Delta\phi_n(\lambda, V)$ for the active switch-state is treated as a sum of a wavelength-independent, voltage-dependent phase $\Delta\phi_n(V)$ and a linear term $d\phi_n/d\lambda$ that models the thermally-induced phase change in each arm of the MZi. Including the active switch-state parameters increases the number of parameters in the model to 21. These parameters are summarized in Table 4.1.

For a switch with n ports, the number of parameters for the passive switch-state model is $5 + 2n$ and the number parameters for the active switch-state model is $2n$ giving a total of $5 + 4n$. The scalability of the model is discussed later in the chapter.

4.3 Modeling Procedure

The fitting procedure for the heuristic model is a sequential two-step process. In the first step, the passive switch-state model is parametrically fit using experimental data for the passive switch-state. In the second step, the active switch-state model is parametrically fit using exper-

Table 4.1: Summary of Fit Parameters

Model Parameters[1]	**Term**
Coefficients for Coupling	a/b, c/d, g/d
3dB Coupling Wavelength	λ_0
Phase term at zero bias	$\Delta\phi_n$
Change in Phase	$d\phi/d\lambda$
Excess Loss	α_n
Voltage-Dependent Phase	$\Delta\phi_n(V)$
Voltage-Dependent change in phase	$d\phi_n(V)/d\lambda$

[1] The parameters that depend on a specific Mach-Zhender interferometer (MZi) are subscripted by n and have four separate terms leading to 21 parameters.

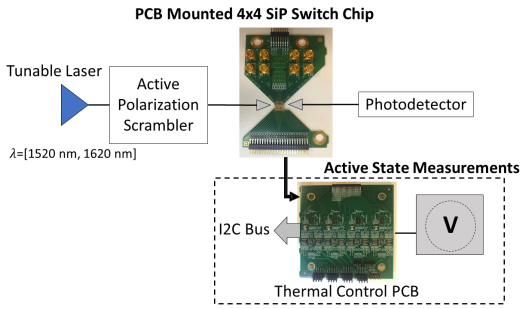

Figure 4.2: Experimental set-up for wavelength-resolved measurements of a 4×4 silicon photonic switch-chip.

imental data for the active switch-state. The active switch-state model includes the extracted coupling coefficient and excess loss from the passive switch-state model plus the additional active switch-state parameters. The two model fits are then used to determine $V_{\pi n}$ for each MZi in isolation. Given $V_{\pi n}$ and $\Delta\phi_n$ for each MZi, Equation 4.3 can be used to predict the voltage for each switch-state.

4.3.1 Measurements

The sequential fit requires a set of measurements for the passive state and a set of measurements for the active state. Ideally, were there no fabrication errors, the first set of measurements would be conducted at a quadrature point for each MZi. A second set of measurements would use a set of voltages to bias each MZi to a different quadrature point to determine the voltage-dependent parameters. The device used to develop the model had fabrication errors. This led to the passive switch-state for some devices not being at a quadrature point. However, these passive switch-states are sufficiently close to the quadrature point, and operate in a perturbative regime, which permits optimization and determination of the best biasing voltages. The active switch-state measurements are collected each MZi actively biased to a quadrature point. The voltages V_{qn} required to set the switch to a quadrature point are determined separately for each MZi such that each MZi has approximately the same output power on each arm. Since each on-chip path utilizes two MZis, an initial estimation of the passive differential phase is used to determine the initial voltages for each quadrature point. This process is discussed in Appendix D. These quadrature point voltages are incorporated into the model for the active switch-state.

Both the passive and active datasets are collected using the set-up as shown in Figure 4.2. A tunable laser is coupled to each input port using a lensed fiber. The power out of each of the four output ports is measured over the range of $1520\,\text{nm} - 1620\,\text{nm}$. The process is then repeated for the other three input ports leading to sixteen wavelength-resolved datasets. In order to prevent state-of-polarization drifts in the setup from affecting the measurements and the subsequent

fitting, an active polarization scrambler is used during the acquisition time of the wavelength-resolved measurements. Then, the polarization state of the laser is scrambled at high speed, which is faster than the inverse of the integration time of the detector. Because the switch-chip is designed for TE polarization, the scrambler introduces a 3 dB loss from the power coupled into TM mode at the interface of the waveguide. The additional TM loss is verified using the straight waveguide. For the purpose of characterization, this step was deemed more practical than aligning the input polarization to the TE mode because only the relative optical power is required for the fits. The measurements for the passive switch-state are shown in Figure 4.3. The measurements for the active switch-state with each MZi biased to the quadrature point are shown in Figure 4.4. Due to the limitations of the power supply board, the range of voltages used are between 0 V to 4 V for each of the heaters. Since each MZi has two heaters, the isolated phase shift of one of the heaters will correspond to a positive or negative differential phase shift for each MZi. Thermal crosstalk between the Mach-Zehnder interferometers was measured by applying voltage to one Mach-Zehnder interferometer and measuring the change of the passive states of the other Mach-Zehnder interferometers on the device. Minimal variation in the passive states was seen.

The total measured on/off chip loss is -9 dB from a straight test waveguide fabricated on-chip for this purpose. This value is used to normalize the measurements.

4.3.2 Fitting Procedure

The extraction of the parameters of the model from the experimental data used a sequential fitting process for both the passive switch-state model and the active switch-state model. Some spectral ripple (typical rms magnitude 2 dB) is present on all the traces, typically from imperfect mode matching at the input and output couplers. We do not model this artifact using the transfer matrices. Therefore, prior to running the fit algorithm, the data is smoothed using a (15^{th})-order polynomial. This smoothed data is shown in black dashed lines in both Figure 4.3

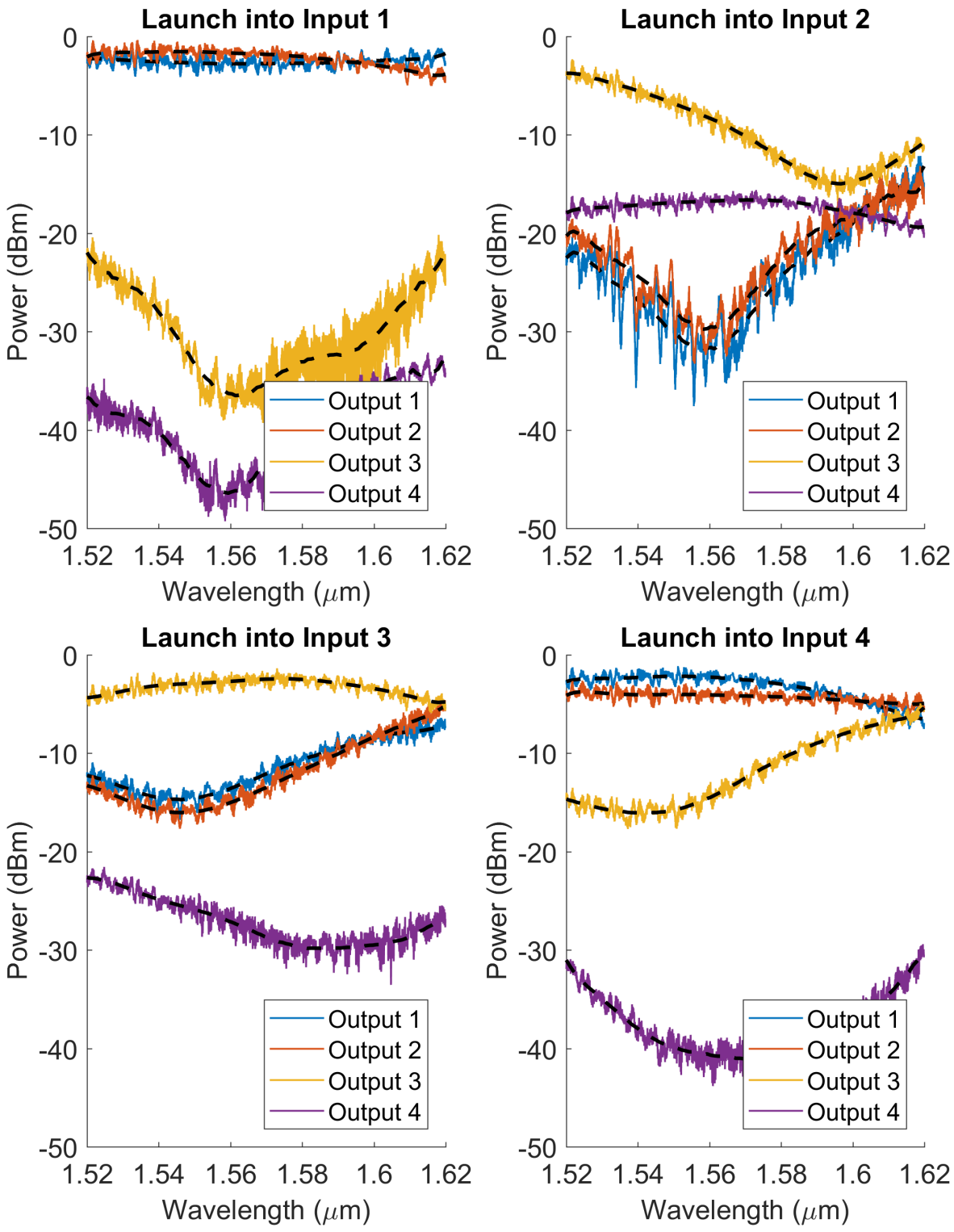

Figure 4.3: Solid Lines: spectral measurements of the passive switch-state for all sixteen input-to-output port configurations. Dashed Lines: the 15^{th}-order polynomial fit of each dataset.

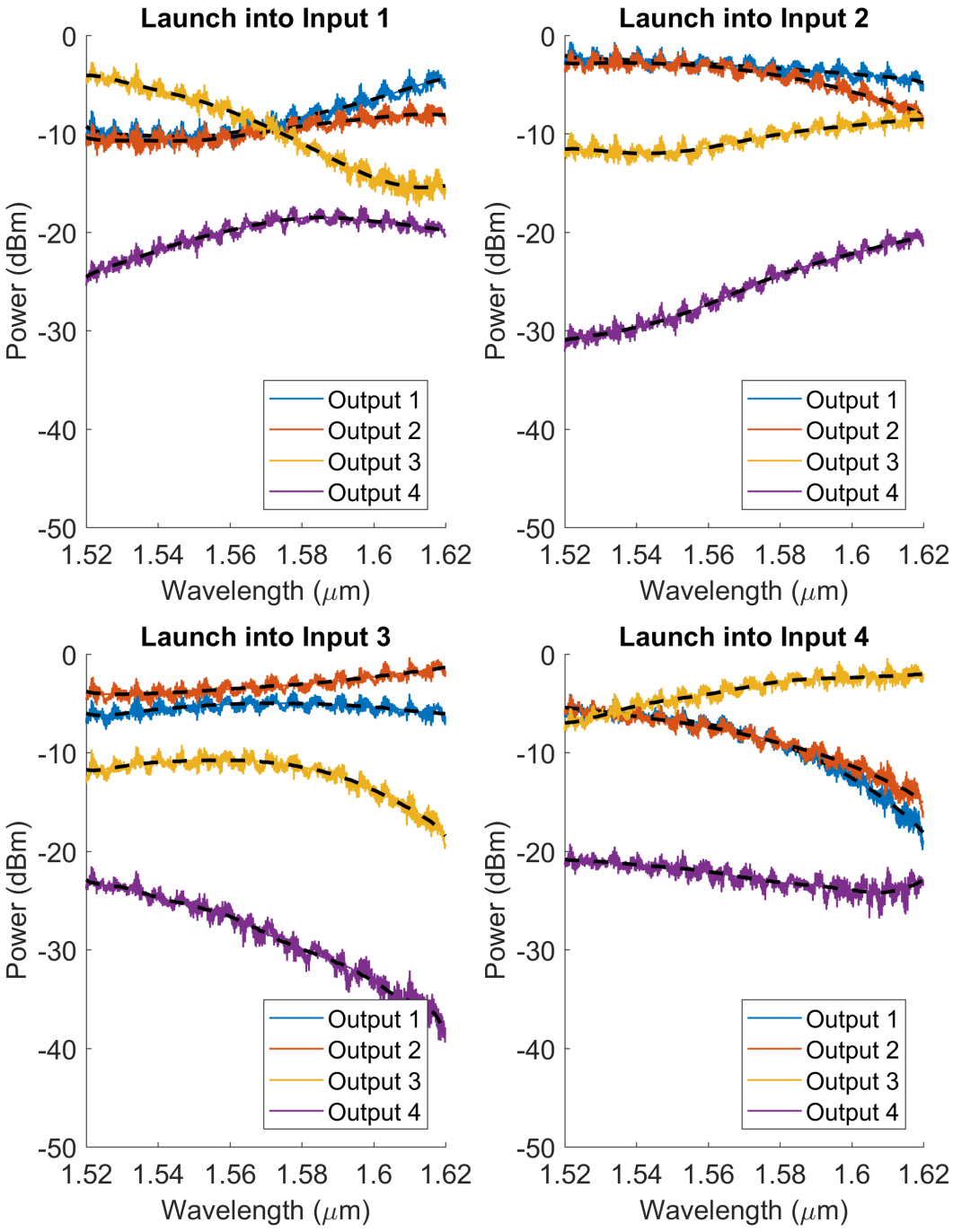

Figure 4.4: Solid Lines: spectral measurements of the active intermediate switch-state for all sixteen input-to-output port configurations. Dashed lines: the 15th-order polynomial fit of each dataset.

and Figure 4.4.

Given a set of initial estimates of the parameters to be fitted, a multivariate parametric nonlinear fit algorithm in Matlab [85] is used to find a final set of parameters that minimizes an objective function $F(\lambda)$ that is the sum of squared terms $f_m(\lambda;\mathbf{x})$ for $m = 1,\ldots 16$. Each of the sixteen terms describes an input to output configuration. This minimization is written as

$$F(\lambda) = \min_{\mathbf{x}} \left(f_1(\lambda;\mathbf{x})^2 + \ldots + f_{16}(\lambda;\mathbf{x})^2 \right). \tag{4.4}$$

The objective function $F(\lambda)$ is minimized by varying the vector $\mathbf{x}$ of parameters. Each term $f_m(\lambda,\mathbf{x})$ in Equation 4.4 is a parameterized function of the wavelength λ given by

$$f_m(\lambda;\mathbf{x}) = \frac{P_{m,\text{model}}(\lambda;\mathbf{x}) - P_{m,\text{data}}(\lambda)}{P_{m,\text{data}}(\lambda)} \tag{4.5}$$

which is the difference between the smoothed wavelength-resolved data $P_{m,\text{data}}(\lambda)$ and the parameterized wavelength-dependent model $P_{m,\text{model}}(\lambda;\mathbf{x})$, normalized by the wavelength-resolved smoothed data $P_{m,\text{data}}(\lambda)$. For the passive switch-state, the vector $\mathbf{x}$ has thirteen parameters. Using these fitted parameters, the active switch-state is then fit using a different vector $\mathbf{x}'$ of fit parameters, which is of length eight.

To obtain the final fit, a Monte-Carlo simulation is run in which the initial value of every parameter is randomly varied within an upper and lower bound as described below. One thousand sets of randomized initial values are generated using this procedure. This method is used because convergence is not guaranteed owing to the nonlinear nature of the model. By choosing random initial values, multiple solutions can be generated and then assessed with regard to other constraints. For some sets of initial values, the fit parameters are tightly clustered. For other initial sets of values, the fit parameters have a considerable spread. Ideally, the randomization of the initial estimates should result in a distribution of the fitted values where the statistical average can be taken to determine the final parametric model with a small spread about the mean

values. The statistical average of the fitted values should highlight solutions that are global minimums. The initial estimates for the parameters and the bounds for the parameters are discussed in Appendix D.

Table 4.2: The initial estimates and the final fit solution for each passive state parameter along with their standard deviations.

Passive Parameters	Initial Estimates	Final Fit Solutions$\pm\sigma$
$\Delta\phi_1$	π	3.09 ± 0.00022
$\Delta\phi_2$	0	-0.55 ± 0.0018
$\Delta\phi_3$	$\pi/2$	1.45 ± 0.0029
$\Delta\phi_4$	$\pi/2$	0.60 ± 0.0046
$d\phi/d\lambda$ [rad μm^{-1}]	-0.0011	-0.0088 ± 0.021
α_1 [dB]	$-.32$	$-.38 \pm 0.000035$
α_2 [dB]	$-.32$	$-.36 \pm 0.010$
α_3 [dB]	$-.32$	0.0 ± 0.000076
α_4 [dB]	$-.32$	$-.48 \pm 0.00032$
α_{Output_4} [dB]	-20	$-17.84 \pm 2.3 \times 10^{-4}$

The passive model fit is shown in Figure 4.5. The active model fit is shown in Figure 4.6. The average solutions for each parameter along with their initial estimates over the 1000 runs are given in Table 4.2 for the passive switch-state model and Table 4.3 for the active switch-state model. The fitted coupling coefficient is plotted in Figure 4.7 using the functional form of Equation B.2 in Appendix B.

The fitted passive differential phases shown in Table 4.2 are typically close to their initial estimates because of how the device was fabricated. The exception is MZi_4 which had a defect on one of its outputs and MZi_2 which had a passive differential phase that is offset from $\Delta\phi_0 = 0$. Moreover, the model can predict the waveguide defect on Output 4, which is important for screening devices in post processing. Additionally, there is no excess loss α_3 for MZi_3 in ad-

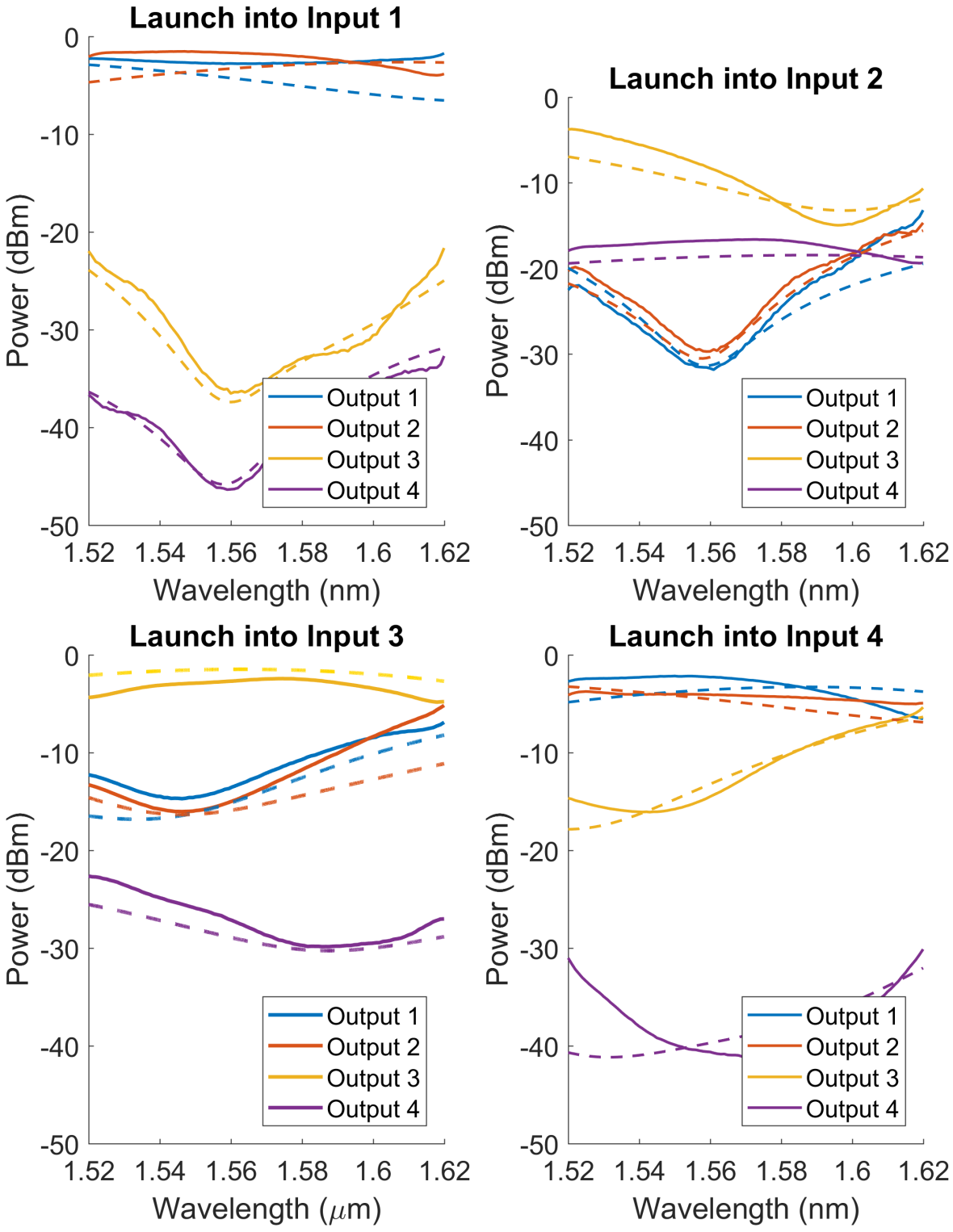

Figure 4.5: Dashed Lines: the parametric fit of the passive switch-state data. Solid Lines: the 15^{th}-order polynomial fit of each dataset.

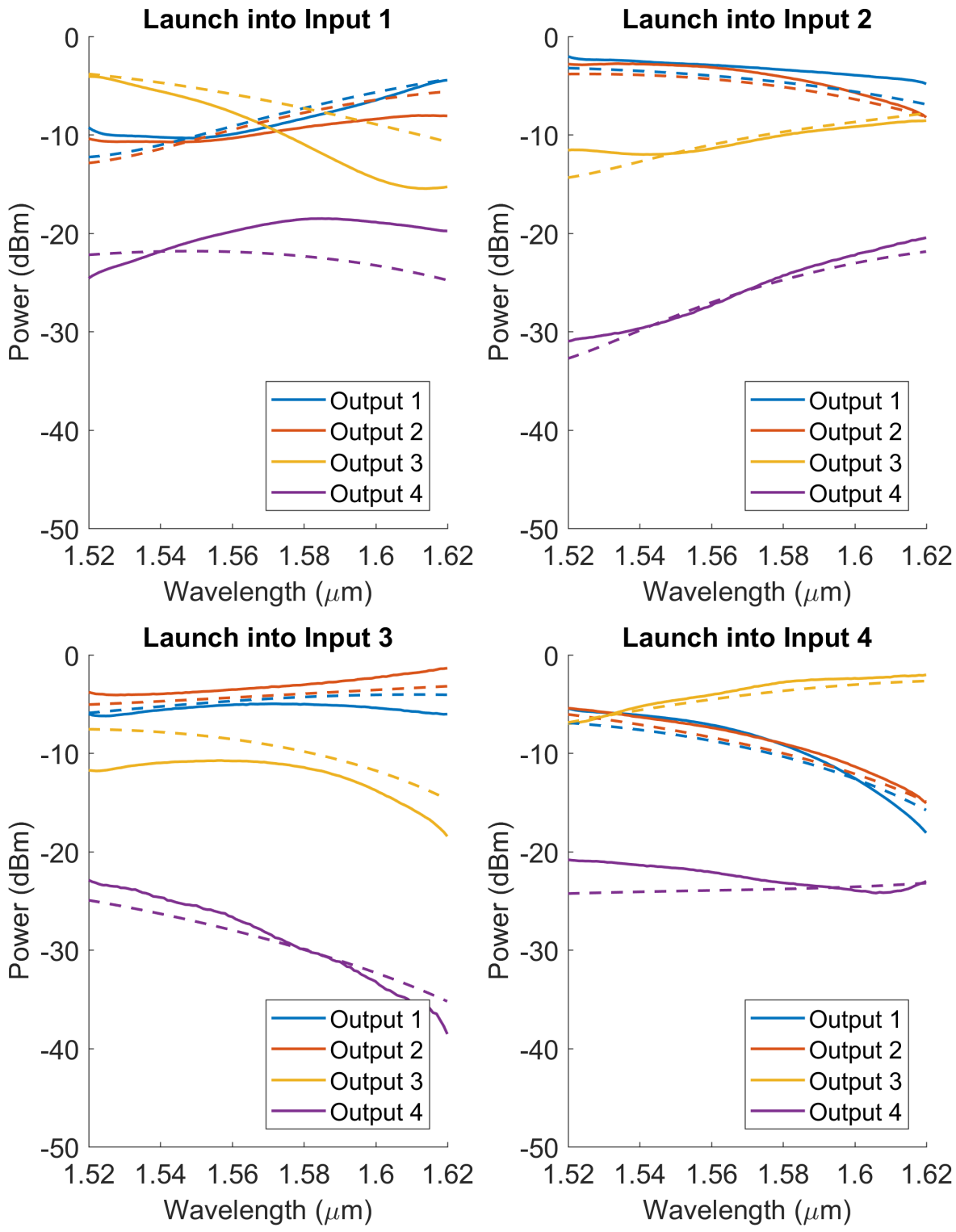

Figure 4.6: Dashed Lines: the parametric fit of the data biased to the quadrature point. Solid Lines: the 15^{th}-order polynomial fit of each dataset.

Table 4.3: The initial estimates and the complete fit parameter for each active switch-state parameter along with their standard deviations.

Active Parameters	Initial Estimates	Final Fit Solutions $\pm\sigma$
$\Delta\phi_1$	$\pi/2$	$1.07 \pm 2.0 \times 10^{-11}$
$\Delta\phi_2$	$\pi/2$	$2.07 \pm 0.041 \times 10^{-6}$
$\Delta\phi_3$	$\pi/2$	$1.61 \pm 0.48 \times 10^{-6}$
$\Delta\phi_4$	$\pi/2$	$1.237 \pm 17.1 \times 10^{-6}$
$d\phi_1/d\lambda$ [rad μm^{-1}]	-0.0088	$0.0023 \pm 6.6 \times 10^{-6}$
$d\phi_2/d\lambda$ [rad μm^{-1}]	-0.0088	$0.0089 \pm 8.8 \times 10^{-6}$
$d\phi_3/d\lambda$ [rad μm^{-1}]	-0.0088	$0.000\,12 \pm 10.0 \times 10^{-6}$
$d\phi_4/d\lambda$ [rad μm^{-1}]	-0.0088	$-0.0136 \pm 6.8 \times 10^{-6}$

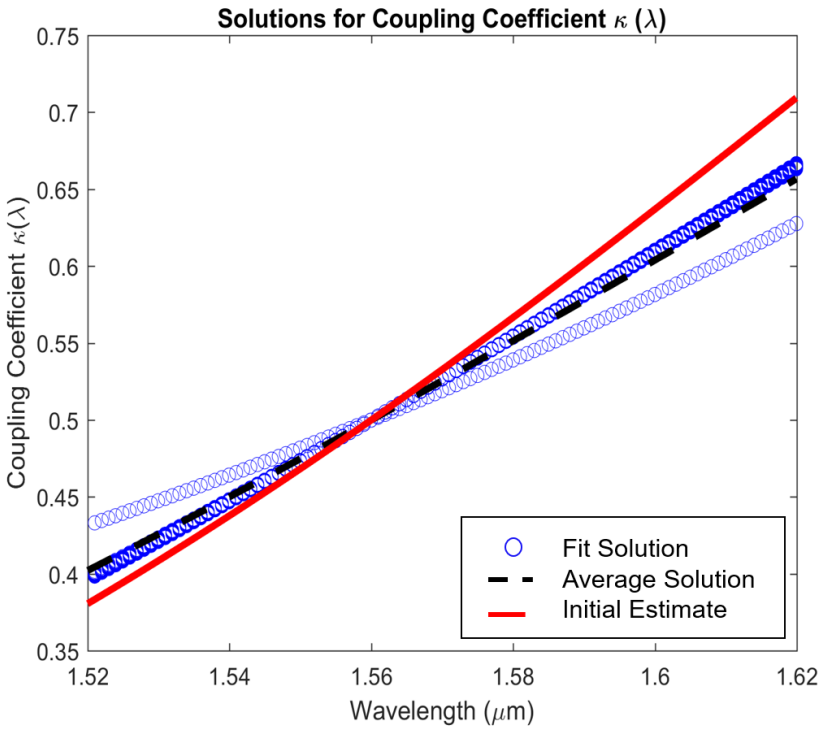

Figure 4.7: Circles: Fit for the coupling coefficient. Dashed line: the average fit solution for the coupling coefficient. Solid line: The initial estimate of the coupling coefficient.

dition to the loss determined from the straight waveguide because this fabricated MZi was close to the desired passive design. The distribution of fit parameters shown in Table 4.2 and Table 4.3 showed a small statistical variation about their mean values. This indicates with significant confidence that an optimal fit was obtained.

4.3.3 Sensitivity of Fit

The final fitted values for both the wavelength-independent differential phase $\Delta\phi_0$ and the coupling coefficient $\kappa(\lambda)$ for the couplers were found to be sensitive functions of the initial estimates and the bounds for those estimates. In comparison, other fit parameters such as the change in phase $d\phi/d\lambda$ and the excess loss are not sensitive functions of their initial estimates. Understanding the sensitivity of each parameter is essential to establishing good initial estimates for the algorithm to properly converge.

An example of this sensitivity is shown in Figure 4.7 where the fit for the coupling coefficient $\kappa(\lambda)$ for the couplers converges to two closely spaced solutions with one solution occurring on 98% of the runs as the initial estimates used in the procedure were varied. Thus, the overall average solution is biased by the solution that occurs more frequently. In Figure 4.7, the plot of the two solutions for $\kappa(\lambda)$ are shown in circles, the weighted average of $\kappa(\lambda)$ is shown as a dashed line, and the initial estimate of $\kappa(\lambda)$ is shown as a solid line.

The sensitivity of $\kappa(\lambda)$ to the bounds on the estimates is a consequence of the simplifications used to develop the model. These simplifications resulted in $\kappa(\lambda)$ containing derived parameters. Comparing the final solution for $\kappa(\lambda)$, which is biased by the more frequently occurring solution, to the initially estimated solution for $\kappa(\lambda)$, it can be seen that maximum relative variation between these two solutions is 6.3% at 1620 nm. Moreover, the variation in $\kappa(\lambda)$ is small compared to the variation from the differential phase mismatch. This residual error is an inevitable trade-off between the level of abstraction of the physics with the predictive power of the model.

4.3.4 Incorporating the Switching Behavior

Once the fitting procedure is complete, the extracted passive differential phases $\Delta\phi_n$ for each MZi, the extracted quadrature point differential phases $\Delta\phi_n(V_{qn})$, and the voltages V_{qn} required to set each MZi to a quadrature point are used to determine V_π. Equating the phase terms in Equation 4.3 gives

$$V_\pi = \sqrt{\frac{\pi V_{qn}^2}{\Delta\phi_n(V_{qn}) - \Delta\phi_n}} \tag{4.6}$$

showing the dependence of the phase on the square of the voltage, which is proportional to the thermal power dissipated in the device.

Because the offset from the quadrature point is included in the model, it is not necessary that the device be biased at exactly a quadrature point. The only requirement is that it is close enough to a quadrature point to provide a nearly linear response. This requirement is quantified in Section 4.4.3.

Were the device ideally biased to the quadrature point, $\Delta\phi_n(V) = \pi/2$, $\Delta\phi_n = 0$ and $V_{\pi n} = \sqrt{2}V_{qn}$ as expected. Once $V_{\pi n}$ is determined for each MZi, Equation 4.6 is used to determine other switch-state voltages. The through switch-state is determined by setting $\Delta\phi_n(V) = \pi$. The cross switch-state is determined by setting $\Delta\phi_n(V) = 0$ or 2π.

4.4 Discussion

This section discusses four aspects of the modeling procedure. First, the accuracy of the model is assessed in terms of its ability to predict biasing voltages for an actual switch-state using measurements derived from the quadrature points. Second, the ability of the model to estimate the crosstalk power is discussed. Then, the robustness of the fit using the quadrature point data is quantified. Finally, the scalability of the model is assessed. Only the C band data is analyzed ($\lambda = 1530\,\text{nm} - 1565\,\text{nm}$).

The fitted results for Output 4 were not included because of the -20 dB defect on the output. However, $\Delta\phi_4$ was still derived to predict switch states that traversed MZi_4.

4.4.1 Validation of Bias Voltages

.

Table 4.4: The "ground-truth" bias voltages and bias voltages from the fitted model for each Mach-Zehnder interferometer (MZi) set to both the through and cross switch-state.

Through Swith-State		
MZi_n	"Ground-truth" Bias Voltages	Bias Voltages from the Model
MZi_1	0.5 V	0.56 V
MZi_2	4 V	3.89 V
MZi_3	3 V	3.17 V
MZi_4	3.5 V	3.0 V
Cross Swith-State		
MZi_n	"Ground-Truth" Bias Voltages	Bias Voltages from the Model
MZi_1	4 V	4 V
MZi_2	1.5 V	1.64 V
MZi_3	2.7 V	2.92 V
MZi_4	2.5 V	1.44 V

The predicted bias voltages to set the switch-chip to a through and cross switch-state from the model are compared to a "ground-truth" set of bias voltages. The "ground-truth" bias voltages are determined manually in a similar manner to how the devices were biased to the quadrature point for the active measurements. Instead of balancing the output powers, the desired output signal is first maximized. Then the crosstalk is minimized for a voltage close to the voltage that produced the maximum output signal power. For this second part of the "ground-truth" measurement, it was seen that on average a 10% change of the bias voltage produced up to a 9 dB change in the crosstalk. This sensitivity indicates that precise crosstalk measurements

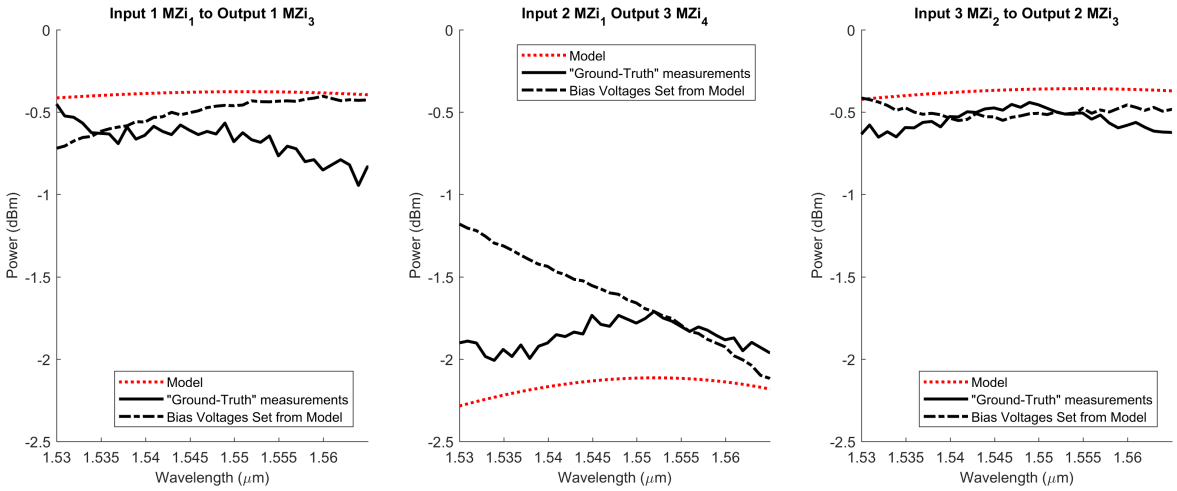

Figure 4.8: Dotted lines: predicted output signal power. Solid Lines: measured output signal power using the "ground-truth" bias voltages. Dash-dot lines: measured output signal power using the predicted bias voltages. MZi_4 is not included because of the -20 dB excess loss on Output 4.

require accurate bias voltages. This precision was difficult to achieve for the device used because of the fabrication errors.

The "ground-truth" bias voltages and the predicted bias voltages from the model for both the through and cross switch-state are shown in Table 4.4. The predicted voltages are in good agreement with "ground-truth" voltages with most predicted voltages close to the "ground-truth" voltages. The largest variation 42.4% in the predicted voltage from the "ground-truth" voltage is for MZi_4 for the cross switch-state. This is attributed to the defect on Output 4.

To confirm the model can accurately predict the biasing voltages for each MZi, the predicted voltage to set a switch-state using the fitted model is compared to the actual measured voltage to set that switch-state. Each MZi is set to the through state a that Input 1 routes to Output 1, Input 2 routes to Output 3, Input 3 routes to Output 2 and Input 4 routes to Output 4. This through switch-state is not a quadrature point and thus was not used to generate the model fit. Therefore it provides a good test case for the predictive power of the model. The measured output powers using the "ground-truth" bias voltages, the measured output powers using the bias voltages predicted by the model, and the predicted output power voltages are shown in Figure

4.8.

In comparing the ”ground-truth” measurements to the predictions from the model and the measurements using the predicted bias voltages, the heuristic model is able to predict the output signal powers for the switch configurations within 1 dB as shown in Figure 4.8. The largest variation is when Input 2 on MZi_1 is routed to Output 3 from MZi_4. This variation in output signal powers is 0.25 dB, which is attributed to the 0.5 V deviation in the predicted voltage for MZi_4 compared to the ”ground-truth” voltage. The deviation in the predicted voltage is likely due to the fabrication defect. A higher overall output loss of 2 dB was also seen when Input 2 on MZi_1 is routed to Output 3 on MZi_4. This was attributed to the higher loss for MZi_4 of $\alpha_4 = -0.48$ dB. The curve showing Input 4 on MZi_2 to Output 4 on MZi_4 is not included because of the -20 dB excess loss.

4.4.2 Crosstalk Power

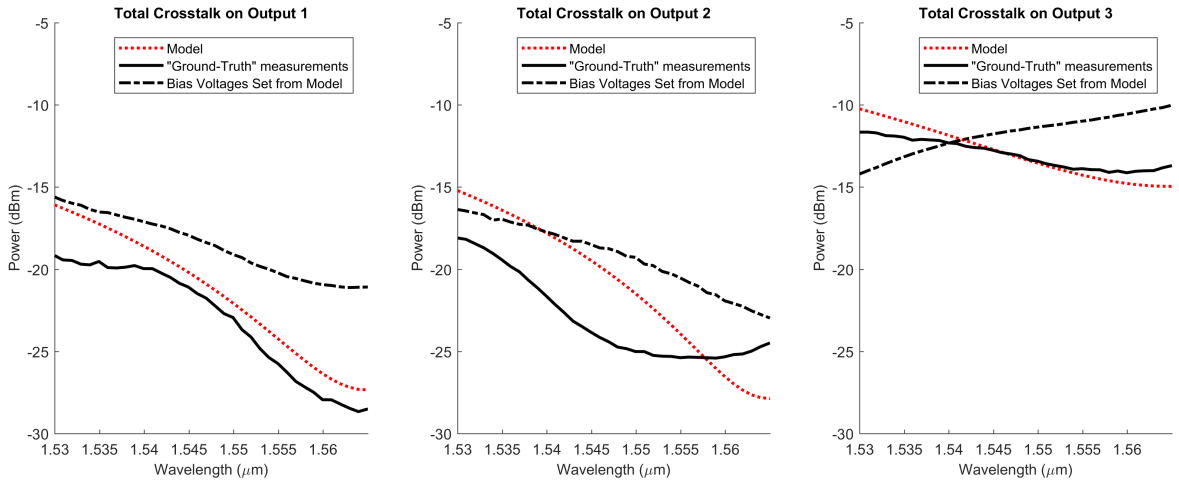

Figure 4.9: Dotted lines: total predicted crosstalk power. Solid Lines: total measured crosstalk powers using ”ground-truth” bias voltages. Dash-dot lines: total measured crosstalk power using the predicted biasing voltages. MZi_4 is not included because of the -20 dB excess loss on Output 4.

To assess the model’s ability to predict the crosstalk for each output channel, the total

crosstalk power per output channel measured using the "ground-truth" bias voltages is compared to the total crosstalk power per channel measured for the set of predicted bias voltages from the model. The results are shown in Figure 4.9 using the through switch-state described earlier.

The largest variation in the per channel crosstalk between the predicted bias voltages and the "ground-truth" bias voltages is 7 dB for the crosstalk measured on output channel 1. The discrepancy between the crosstalk measurements using the "ground-truth" voltages and the crosstalk measurements using the predicted bias voltages is attributed to the error in the predicted bias voltages compared to the "ground-truth" bias voltages for MZi_1 and MZi_4. As stated previously, an average error of 10% in the predicted bias voltages can produce a change of 9 dB in the crossatlk power. This error is a consequence of the crosstalk being a sensitive function of optical phase, which is not directly measured using intensity measurements. The sensitivity of the crosstalk to the bias voltage and phase between the optical paths within the switch means that accurate prediction of crosstalk requires precise fabrication.

4.4.3 Robustness of the Quadrature Point

Using a switch-state at the quadrature point for model characterization results in a more robust fitting procedure because the power at each output port of the device is better balanced compared to an actual switch-state that uses a through or a cross state. As a consequence, compared to the case when a through or cross switch-state is used to fit the model, the sequential fit algorithm is not as sensitive to the initial estimates of the parameters or the bounds on those parameters. This also means that a single measurement at a quadrature point can be used to predict the performance of both the cross and the through state as was done in the previous section. In comparison, poor results would be obtained when a cross switch-state is used to predict the characteristics of a through switch-state.

In order to assess the robustness of the quadrature point, the bounds of the linear regime about the quadrature point are analyzed. As shown in the active quadrature point measurements,

the output powers were not exactly balanced. This resulted in the voltage-dependent offset phases $\Delta\phi_n$ for each MZi having values between $\pi/3$ and $2\pi/3$. A power series expansion of $\cos^2(\Delta\phi/2)$ about the quadrature point when $\Delta\phi = \pi/2$ shows that the largest error is caused when the bias point is at $\pi/3$. For this bias point, the relative error between the linear term of the power series and $\cos^2(\Delta\phi/2)$ is approximately 4%. This shows that the region about the quadrature point is nominally linear over a moderate range of bias points leading to a robust fitting algorithm.

4.4.4 Scalability

There is a trade-off in the quality of the sequential fit and the number of parameters used in the model. The rate as which the parameters scale with increasing device topology is called the scaling factor. The scaling factors of the model for a switch with n MZis are $5+2n$ for the passive switch-state model and $2n$ for the active switch-state model leading to a total scaling factor of $5+4n$. The number of model parameters also determines the minimum number of datasets required for the sequential fit without the system being under-determined. To test the number of datasets required, the sequential fit is run for eight datasets, which is half the data used in the fit procedure as described previously. The sets are chosen such that the optical paths maximized the path diversity. The optical paths in order to maximize the optical path diversity were Input 1 to Output 1 and Output 4, Input 2 to Output 2 and Output 3, Input 3 to Output 2 and Output 3 and Input 4 to Output 1 and Output 4. These data sets were chosen for both the passive measurements and the active quadrature point measurements. Fig. 4.10 shows the eight sets of optical paths chosen.

The normalized differences between the average solution using sixteen datasets and the average solution using eight datasets is .34% for the passive switch-state model and -1.03% for the active switch-state model. This small difference indicates that halving the required number of measurements may be useful when the number of ports used for testing is constrained. However,

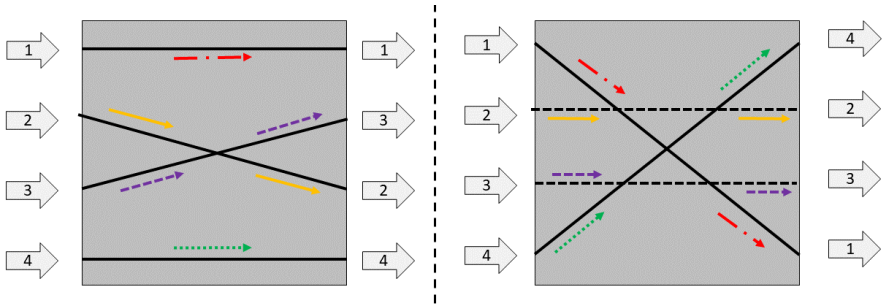

Figure 4.10: Eight optical paths used for the reduced datasets to maximize path diversity.

when integrated fiber arrays [86] [34] are used for testing, the number of ports is not constrained. For this case, a total number of n^2 measurements for each switch-state may be used to develop the model.

4.5 Conclusion

A heuristic parametric model of a silicon photonic switch-chip using a set of quadrature state measurements has been presented in this chapter. The novel approach of fitting the model using an quadrature state leads to a robust fit compared to using actual switch-states for the model fit. The model has been shown to be effective at predicting the bias voltages for an actual switch state that has small fabrication errors in the passive state. The heuristic characterization methodology presented here is one step in establishing scalable testing for large port-count switch chips. This heuristic model developed in this chapter is an approach to tackling the issues of high-yeild characterization and post-pprocessing of silicon photonic switches.

Chapter 4 in part, contains material, published in the following, of which the dissertation author was the primary investigator:

H.R. Grant, G. Papen, S. Mookherjea, L. Schares and B.G. Lee, "Heuristic Model for Rapid Characterization of a SiP Switch-Chip," accepted for publication at *Journal of Lightwave Technology*, 2018.

Chapter 4 in part, contains material, published in the following, of which the dissertation

author was the primary investigator:

H.R. Grant, G. Papen, S. Mookherjea, L. Schares, and B.G. Lee, ”Heuristic Characterization of SiP Switches,” in *Advanced Photonics Conference 2017 (PS)*, PTu3C.1.

Chapter 5

All-Optical Barrel Shifting

The unique ability of SiP to integrate both photonics and electronics on a single platform motivates research into the co-optimization of the functionalities that are best implemented optically and those functionalities that are best implemented electronically. Optical functionalities within SiP can offer clear advantages in terms of bandwidth and energy efficiency for the transport of information in comparison to electronic implementations [18]. However, optical components within SiP lack a viable nonlinearity that can be used for large-scale optical memory or sequential logic. This means that SiP cannot readily implement functionalities in the optical domain that require conventional digital logic. The functionalities that can be realistically implemented in SiP are limited to to linear "stateless" functions that do not require memory.

While optical components within SiP cannot currently implement digital logic, there are many other processing functions that could be implemented optically that are currently implemented electronically. Characterizing the class of functions that could be implemented optically leads to an informed choice on the delineation of functions that are best implemented optically and the functions that are best implemented electronically for a co-optimized SiP chip design. To this purpose, this chapter considers the optical implementation of one processing function, called a barrel shifter, in a SiP platform. We discuss and experimentally characterize the im-

plementation of this function in several standard SiP platforms and draw conclusions on the feasibility of using SiP for optical-domain barrel shifting. The key contribution of this work is analyzing and demonstrating how a linear "stateless" functionality such as barrel shifting can be implemented in a SiP platform with conventional SiP devices.

5.1 Barrel Shifting Background

This section will describe conventional electronic barrel shifting as well as investigate previous approaches to optical barrel shifting.

5.1.1 Conventional Barrel Shifters

A conventional barrel shifter is a digital circuit operating on multiple bit lines that can shift a block of data by a specified number of bits without the use of any sequential logic. This functionality is usually implemented as a cascade of multiplexers [87]. In the 1980's, Intel developed a programmable numerical processor that had the capability to shift arbitrary numbers of bits in a single clock cycle [88]. Soon other work evolved to include rotation functionality and bi-directional capability [89, 90].

In general, barrel shifters have $\log_2 n$ stages for an n-bit data word [87]. Therefore, a 4-bit barrel shifter has two stages with shifts in values of one and four. An 8-bit barrel shifter has three stages with shifts in values of one, two and four. More specifically, barrel shifters have $n \log_2 n$ multiplexers for an n-bit word. A 4-bit barrel shifter has eight multiplexers. An 8-bit barrel shifter has 24 multiplexers. Barrel shifters are commonly used in modern microprocessors for operations such as floating-point arithmetic.

5.1.2 Optical Barrel Shifters

Given that barrel shifting is a ubiquitous transformation in electronic data processing, there is a significant body of work that describes implementing this function optically. The basic operation of an optical barrel shifter can be implemented using a cyclic interferometer. This kind of device can be used to test bulk optical components [91, 92]. A key feature of the cyclic interferometer is that the optical path in the interferometer is a periodic function. All-optical barrel shifting, which can be regarded to as cyclic shifting, was first introduced in the late 1980s using bulk optical components [93–95]. In these devices, the shift or the direction of the shift was done mechanically.

Different implementations of all-optical barrel shifting are known. Diffractive elements were a common approach to implement barrel shifting in optics. Diffractive lenslet arrays [96] incurred high losses and suffered fabrication errors. Diffractive lenslets were also used in a $4f$ imaging system to demonstrate optical barrel shifting with passive discrete phase structures [97]. Liquid crystal light valves have been used to implement bit wise barrel shifting [98], but this required encoding the shift in the lightwave polarization. Finally, acousto-fiber-optic barrel shifting was demonstrated with a speed of 1.2 Gbit/s and a loss of $-26\,\mathrm{dB}$. This approach was also sensitive to polarization because of the birefringence of the acousto-optic cell [99]. In summary, previous approaches to implementing all-optical barrel shifting operated were too slow, were sensitive to errors, had significant loss, and required more power consumption compared to the integrated SiP solutions considered in this chapter.

5.1.3 Optical Barrel Shifters in SiP

Existing realizations of optical barrel shifting in SiP take advantage of wavelength-multiplexing (WDM) capability of microrings [100]. However, these devices still require electrical to optical (EO) conversion which adds complexity and increases the overall power. The

power consumed without including EO conversion is $A \times \log_2 N$ joules per bit where N is the number of microring resonators and A is the energy consumed in joules per bit for each 2×1 electrical multiplexer at the given CMOS node [101].

In contrast to previous work, this chapter considers an all-optical barrel shifter in a silicon photonics platform that does not require EO conversion. This improvement is realized by using a set of microring resonators plus a 4×4 Mach-Zehnder switch used as an optical spatial multiplexer. Mach-Zehnder interferometers are used for spatial multiplexing because they can be broadband. Microring resonators are used to provide wavelength selectivity. Combining these two features, our implementation has the potential to improve power consumption and eliminate costly analog to digital conversion. We examine this design in terms of the shifting speed, loss, and crosstalk to determine the required device characteristics so that the optical implementation of this functionality is competitive with alternative optical approaches, such as an approach that uses only spatial multiplexing.

Both microring resonators and Mach-Zehnder interferometers have been extensively studied in silicon photonics [57, 69, 102], and both types of silicon photonic structures can use heating elements to tune or shift the device [2, 61]. By combining WDM with spatial multiplexing, there is a smaller thermal load on the microrings thereby mitigating any loss due to the reduction of the Q-factor and errors in resonance. Moreover, limiting the required tuning range for each microring simplifies the operation of the microring without limiting the overall bandwidth of the device. Recently, waveguide-integrated microheaters [61,62] have demonstrated the possibility of fast, sub-microsecond-scale thermal tuning of microrings and coupled microring filters. Microring resonators are also smaller compared to Mach-Zehnder interferometers [69], so the combination of these two kinds of functionalities within a single device can lead to a smaller footprint.

5.2 All-Optical Barrel Shifter Design

This section presents the proposed designs of a four-channel and an eight-channel all-optical SiP barrel shifter.

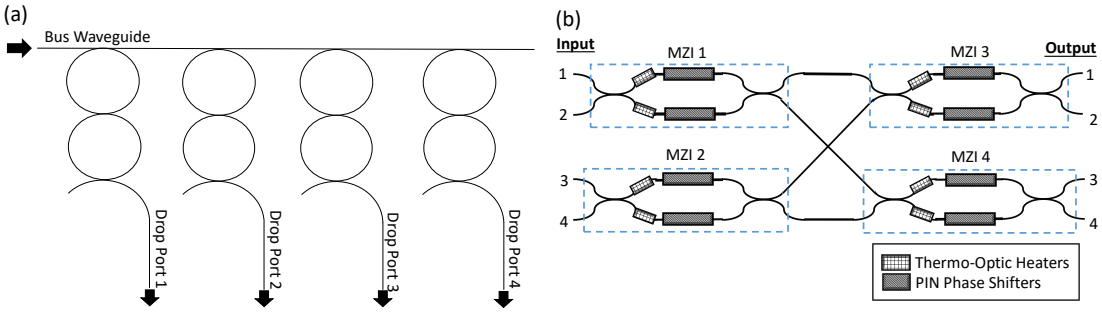

Figure 5.1: (a) Four-channel coupled microring Resonators; (b) 4×4 Mach-Zehnder interferometer switch used as a spatial multiplexer.

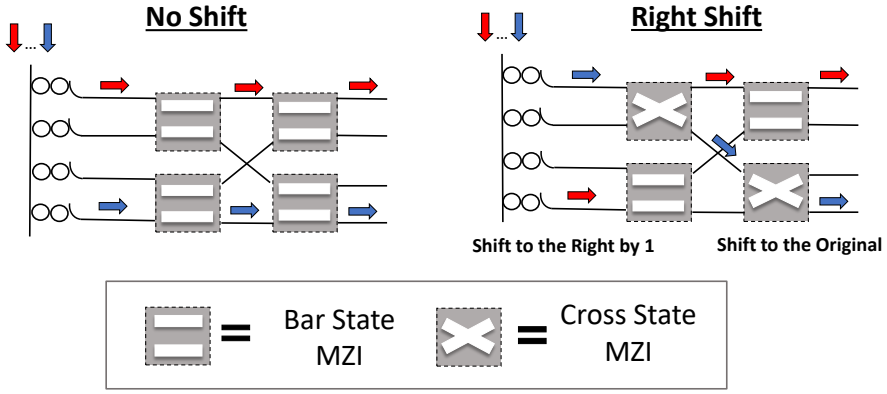

Figure 5.2: Four-channel barrel-shifter design. Left: no barrel shift. Right: a shift by one stage to the right.

The proposed four-channel design consisted of two stages. Stage one is a bus waveguide that can drop an appropriately-tuned lightwave signal into any one of four second-order microring resonators (MRR) as shown Fig. 5.1(a). The microring resonators are based on the device described by Wang *et al.* in [103]. Stage two shown in Fig. 5.1(b) is based on a 4×4 blocking Mach-Zehnder interferometer (MZI) switch chip as described by Dupuis *et al.* [45, 66]. The design connects each drop port of the set of coupled microrings to one input of a 4×4

Mach-Zehnder switch that is used as a spatial multiplexer. The Mach-Zehnder interferometers are arranged in a butterfly topology. This results in a total of four sets of coupled microrings and four Mach-Zehnder interferometers. The block diagram of the four-channel barrel shifter is shown in Fig. 5.2.

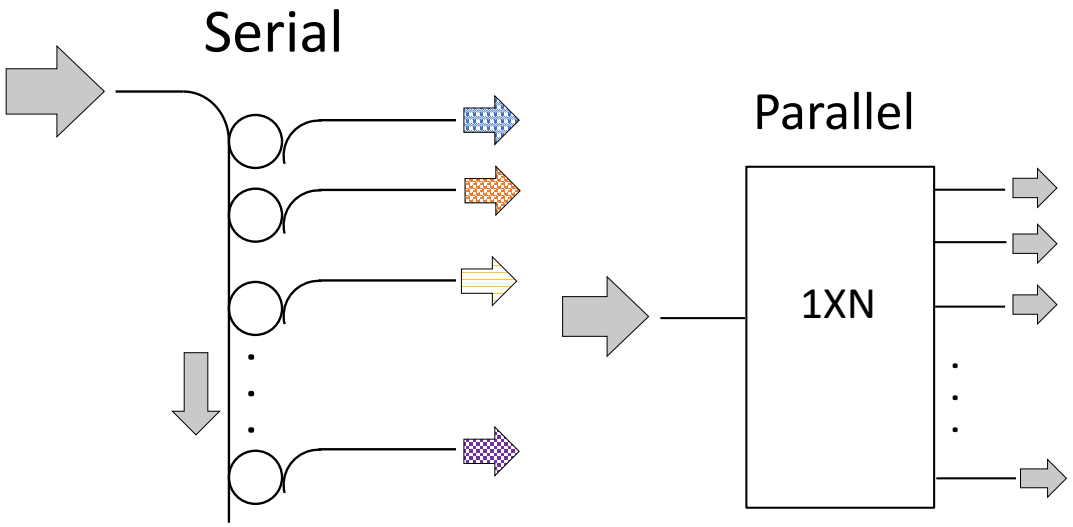

Figure 5.3: Demultiplexer architectures: serial bus waveguide versus parallel $1 \times$ N splitter.

5.2.1 Demultiplexer Architectures

A microring-based wavelength demultiplexer was deemed a better choice compared to a passive $1 \times$ N splitter as the input architecture. In comparing the operations of these wavelength-demultiplexing architectures, the microring-based demultiplexer operates as a serial port where desired wavelengths are filtered off individually. The $1 \times$ N splitter operates as a parallel port, where all signals are separated in one operation. The operations of each demultiplexing architecture is shown in Fig. 5.3. There are several advantages to using a microring-based demultiplexer. The microring-based demultiplexer allows for the separate tuning of each microring response. Therefore, for a properly-designed device, if a port fails, another microring can be tuned to the spectral wavelength used without loss of functionality. The $1 \times$ N splitter does not have this

fault-tolerant functionality. The microring-based demultiplexer can also have lower insertion loss for some channels. The 1 $\times$ N passive splitter has a higher insertion loss on every channel.

5.2.2 Microring Filter Responses

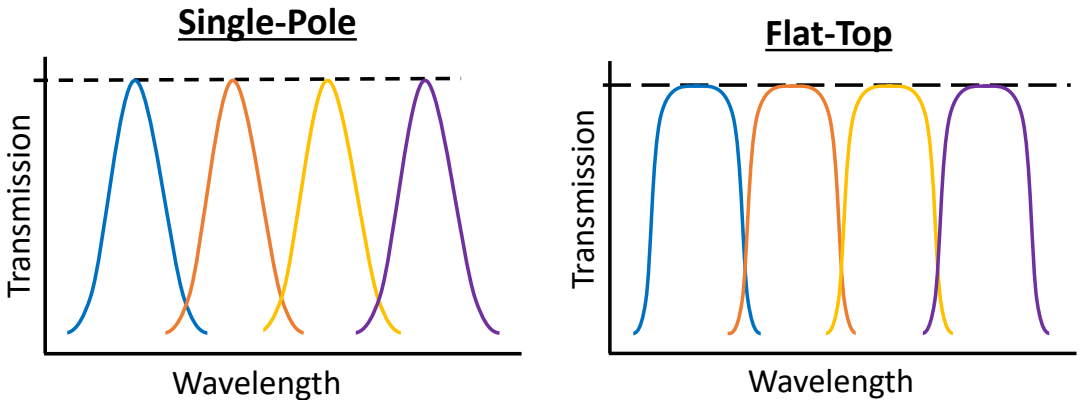

Figure 5.4: Filter responses for a single-pole filter and a flat-top filter.

Microring resonators act as filters that drop appropriate wavelengths. A single-pole response for a single-microring resonator and a multiple-pole response using coupled microring resonators are shown in Fig. 5.4. A single-pole response using a single microring resonator is simpler to fabricate and allows for more non-resonant wavelengths to pass through. However, this kind of device suffers from temperature sensitivity, which can be difficult to mitigate. A flat-top response using coupled microrings is more temperature-insensitive but suffers from higher losses and allows for fewer non-resonant wavelengths to pass through. The spectral roll-off of a flat-top response can be improved by using higher-order microring filters, but this will result in an increase in insertion loss and a higher sensitivity to fabrication errors. The physical devices shown later in this chapter used coupled microring resonators. The simulations used single microring resonators because single microring resonators have lower losses and better crosstalk compared to higher-order microrings.

5.2.3 Eight-Channel Barrel Shifter Design

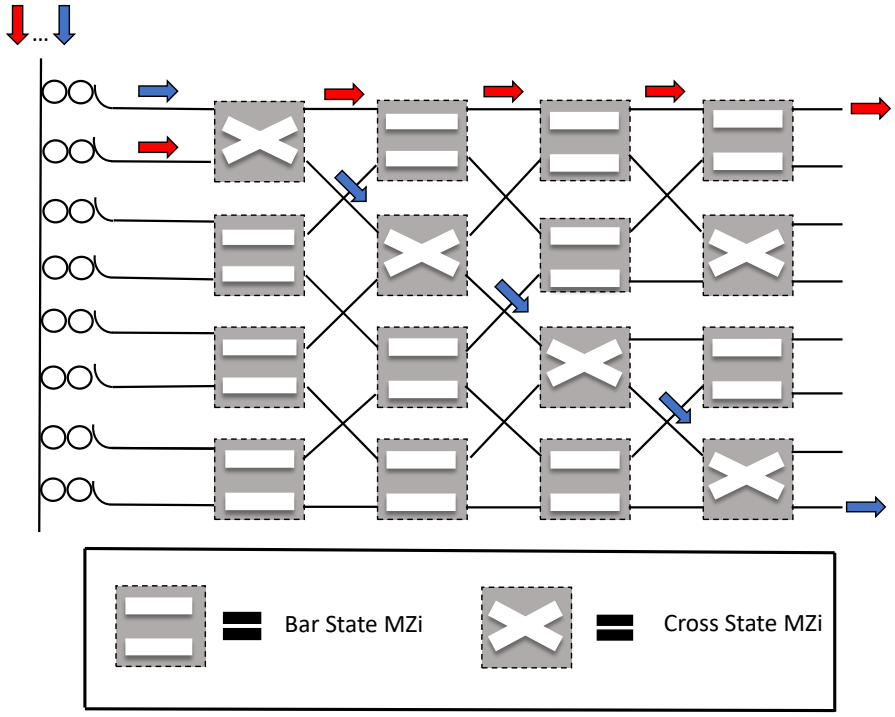

Figure 5.5: Block diagram of the eight-channel barrel shifter that is a combination of 1×8 coupled microrings and an 8×8 Mach-Zehnder spatial multiplexer. The arrows shown are for channel 1 (red) and channel 8 (blue).

The proposed eight-channel design is an extension of the four-channel design. A block diagram of this design is shown in Fig. 5.5. The eight-channel barrel shifter is composed of eight sets of coupled microrings and a multi-stage Mach-Zehnder interferometer-based blocking spatial switch. Similar to the four-channel barrel shifter, each drop port of a microring resonator connects to one input port of the spatial switch. The spatial switch has a total of 16 Mach-Zehnder interferometers connected in an blocking banyan topology [104] resulting in eight waveguide crossings. The eight-channel design uses the same free-spectral range (FSR), but a smaller resonance wavelength separation compared to the four-channel design.

5.2.4 Experimental Implementation of Barrel Shifting

The experimental feasibility of optical barrel shifting was assessed using separately fabricated SiP devices for the coupled microrings [103] and the 4×4 Mach-Zehnder switch used as a spatial multiplexer [45, 66]. The characterization of the devices to be implemented in a barrel shifter is discussed in Section 5.4.

5.3 Simulating a Barrel Shifter

The two barrel-shifting topologies described in Section 5.2 were assessed using Lumerical [1,24]. First, the microring resonator and the Mach-Zehnder interferometer components were broken down into substructures. These substructures were then simulated in Lumerical Device and Mode. Then, the substructures of each component were combined to create a hierarchical design of the barrel shifter in Lumerical Interconnect. The underlying process of Lumerical Interconnect is scattering matrices [1, 24].

5.3.1 Modeling Methods

The device parameters for the simulated barrel shifters were chosen to produce a high-performance device. Practical issues of realizing these design choices are discussed in Section 5.5.3. Metal heaters were used to ensure lower losses. A fully-etched ridge waveguide structure of 500 nm in width and 220 nm in height was used as the waveguide cross-section. The motivation for this choice is that fully-etched waveguides have less variation in group index in the C-band and L-band compared to partially-etched waveguides.

The filter response of the microrings was designed to drop four or eight separate signal channels. The four-channel barrel shifter was designed such that each microring had an approximate free-spectral range (FSR) of 6 nm with each resonant wavelength separated by 1 nm. The microrings used in the eight-channel barrel shifter were also designed for an approximate FSR

of 6 nm but with a resonant wavelength separation near 0.5 nm. The Mach-Zehnder 4×4 spatial multiplexer was implemented using parameters derived from the fabricated device discussed in Section 5.4.

Substructures

While Lumerical Interconnect offers both microring resonators and Mach-Zehnder interferometers as standard library components, these standard components have limited degrees of freedom. To allow for more design flexibility, both the microring resonators and the Mach-Zehnder interferometers were built as a combination of substructures. The use of substructures can incorporate results from lower-level simulations such as the change in index as a function of temperature applied from a heating element. Wavelength dependence and heater tunability can be easily altered to reflect a realistic case of a SiP structure.

The substructures for both the microring resonators and the the Mach-Zehnder interferometers were waveguides, couplers, and active phase tuners. With the exception of the couplers, these substructures were designed to be the same for both the microring resonators and Mach-Zehnder interferometers. These substructures are categorized as either passive or active.

Passive Substructures The passive substructures were the waveguides and the couplers. With the waveguide cross-section fixed, the passive effective index n_{eff} and the group index n_g for the waveguides were simulated in Lumerical Mode. The simulated n_{eff} and n_g were incorporated into the measured waveguide component in Lumerical Interconnect.

The microring resonators and the Mach-Zehnder interferometers required different power-coupling coefficients. The Mach-Zehnder interferometers used a power coupling coefficient of $\kappa^2 = 0.5$ for the 3 dB couplers, and the microring resonators used a power coupling coefficient of $\kappa^2 = 0.1$. Given the small spectral range of interest (6 nm), the built-in Lumerical Interconnect coupler component with fixed power-coupling coefficients was used.

The passive waveguide loss was set to $3\,\mathrm{dB\,cm^{-1}}$ [1] in order to account for surface scattering losses. The radii of the microring resonators and the bending regions of the Mach-Zehnder interferometers were chosen such that the bending losses were nominal [5].

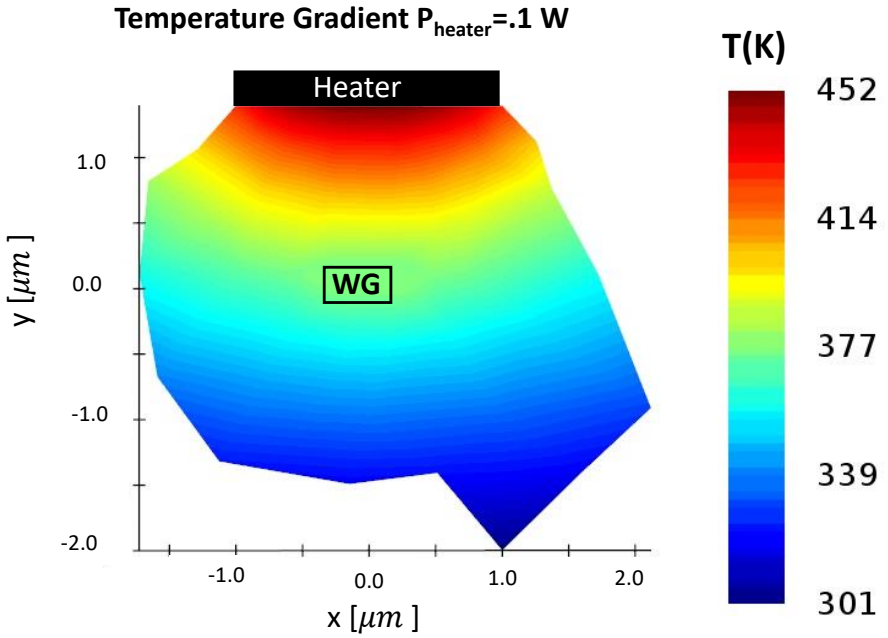

Figure 5.6: Simulated temperature gradient at 0.1 W applied to heater in Lumerical Device. Color indicates the temperature in kelvin.

Active Substructures In Lumerical Device, the thermal dissipation from a metal heater above a waveguide was simulated in the X-Y plane over a fully-etched ridge, 500 nm wide waveguide structure on a 220 nm silicon-on-insulator (SOI) platform. The aluminum heating element [105] was 2 µm wide, 0.2 µm tall and 1.2 µm above the top plane of the waveguide. The power applied to the heater varied from 0.01 W to 0.3 W.

Using a 2D z-normal solver geometry in Lumerical Device, a thermal steady-state solver was used to determine thermal gradients within the simulation region at each power level applied to the heater. The base temperature for the simulation was held at 300 K. An example of the thermal gradient when 0.1 W is applied to the heater is shown in Fig. 5.6.

To determine the effect of the thermal dissipation on the optical mode, the simulated thermal gradients in Lumerical Device were imported to Lumerical Mode. A finite difference eigenmode (FDE) solver was used to extract the effective index n_{eff} and group index n_g for each thermal gradient.

The results for n_{eff} as a function of the power applied to the heater were used to construct a component in Lumerical Interconnect that reflected the real index change as a function of temperature applied by a heater. This was implemented using the Measured Phase Modulator component in Lumerical Interconnect. The Measured Phase Modulator component is referred to as the Heater for the rest of this chapter.

Barrel Shifter Composition

Both microring resonators and Mach-Zehnder interferometers were composed of two heaters, two passive waveguides and two directional couplers. The properties of each of these substructures were imported to Lumerical Interconnect to create each component. Each substructure has a set of input and output ports that create a microring resonator or a Mach-Zehnder interferometer. The final interconnect models for the microring resonator and Mach-Zehnder interferometers in Lumerical Interconnect are shown in Fig. 5.7(a) and Fig. 5.7(b).

For the microring resonators, the round-trip length L_{rt} of the entire microring was determined for an approximate FSR of 6 nm and an approximate resonant wavelength spacing of 1 nm or 0.5 nm. For the Mach-Zehnder interferometers, the difference in optical path length ΔL between the two arms is determined for quadrature-point operation at 1550 nm.

The microring resonators round-trip lengths L_{rt} were defined as the total circumference of the microring resonators. The total L_{rt} was related to the FSR by

$$L_{\text{rt}} = \frac{\lambda^2}{n_{\text{g}} FSR}. \tag{5.1}$$

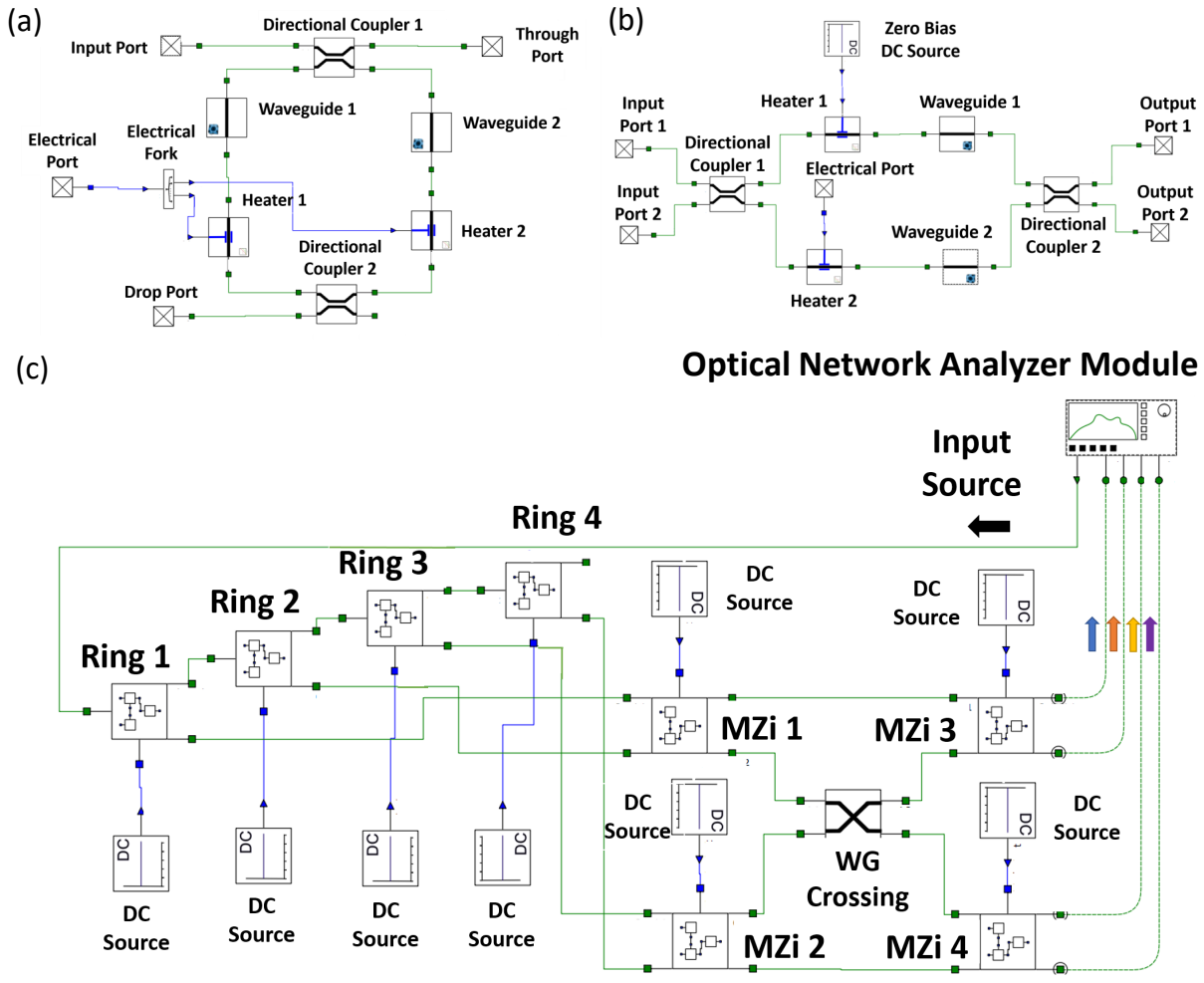

Figure 5.7: Lumerical Interconnect models for (a) microring resonators, (b) Mach-Zehnder interferometers and (c) the four-channel barrel shifter.

Using the simulated group index n_g, the desired FSR and the desired resonant wavelength, a total round-trip length was calculated for each of the four microrings.

The optical path length difference ΔL for the Mach-Zehnder interferometers was determined to be at $\lambda/4$ for 1500 nm. This corresponds to quadrature point operation. For an ideally fabricated Mach-Zehnder interferometer at a quadrature point, the optical phase difference between the arms should be $\Delta\Phi = \pi/2$.

For control of the heating structures, a DC voltage source was used in Lumerical Interconnect. The independent variable of the DC voltage source corresponds to power applied to the heater in Watts. As shown in Fig.5.7(a), the heaters for the microring resonator were connected to the same electrical output via a lossless electrical splitter. This ensured each heater received the same amount of applied power. The Mach-Zehnder interferometer heaters each had their own DC source. One source was set to a zero bias, and one source was set to a non-zero bias to ensure push-pull operation.

A script in Lumerical Interconnect configured the input and output ports of the microrings and Mach-Zehnder interferometers to build the two barrel shifter designs. The drop ports of the microrings were each connected to one input port of the Mach-Zehnder spatial multiplexers. Both 4×4 and 8×8 Mach-Zehnder spatial multiplexers were modeled by directly connecting the Mach-Zehnder interferometers or using waveguide crossings. To simplify the simulation, the built-in Lumerical Interconnect waveguide crossing was used with a loss of 0.05 dB [106–109] and a crosstalk of -40 dB [108, 109]. The final four-channel barrel shifter is shown in Fig. 5.7(c). The eight-channel model was composed in a similar manner.

5.3.2 Results

Simulated spectral results for the two barrel shifter models were obtained by connecting an optical network analyzer (ONA) module to the input of the barrel shifters with the output traced back to the ONA module. The ONA module can monitor the optical power for one input

with respect to multiple outputs at once.

Four-Channel Barrel Shifter

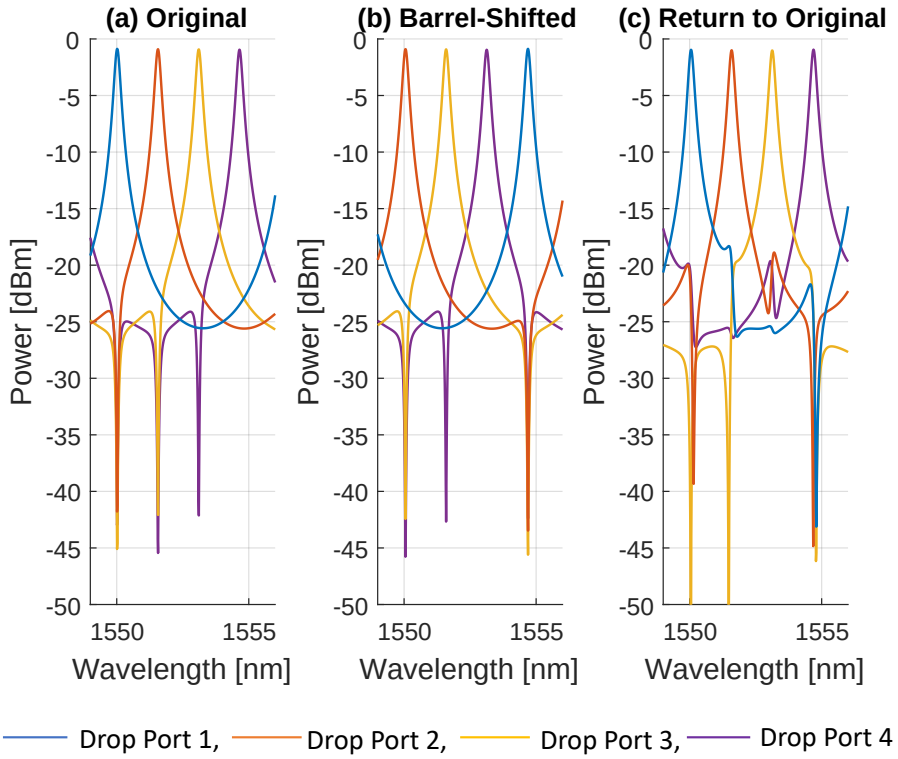

Figure 5.8: Simulated four-channel barrel shifter spectra for (a) the original spectrum after the microring resonators, (b) the barrel shifted spectrum after the microring resonators and (c) the original ordering after the 4×4 Mach-Zehnder spatial multiplexer

The output spectrum before shifting is shown in Fig. 5.8(a) The simulated resonant wavelengths were 1550.02 nm, 1551.55 nm, 1553.11 nm, 1554.65 nm with a resonant wavelength separation of 1.5 nm. The resolved average free spectral range (FSR) is 6.53 nm.

Fig. 5.8(a) also shows nulls in the spectra for Drop Port 2, Drop Port 3 and Drop Port 4 because the previous ring has dropped that wavelength. The average loss is -0.9 dBm. The full-width-half-max (FWHM) of each resonance is ≈ 0.2 nm, which results in Q-factors on the order of 8000. In comparison, the fabricated SiP coupled microring resonators characterized later in this chapter have a Q-factor of 1890.

The resonant wavelength of the microrings were shifted by applying 154 mW to Ring 1 and 165 mW to Ring 2, Ring 3, and Ring 4 . This resulted in a tuning efficiency of $0.0301\,\mathrm{nm\,mW^{-1}}$ for Ring 1 and tuning efficiency of $0.0208\,\mathrm{nm\,mW^{-1}}$ for Ring 2, Ring 3 and Ring 4. The shifted spectrum is shown in Fig. 5.8(b). The smaller tuning power for the first microring (shown in blue) caused the resonance wavelength to "jump" the other three rings, which were shifted by a change in resonance wavelength that was greater than the FSR. The shift resulted in the response wavelength of Drop Port 1 shifting to 1554.65 nm, Drop Port 2 shifting to 1550.02 nm, Drop Port 3 shifting to 1551.55 nm and Drop Port 4 shifting to 1553.11 nm. This spectrum was used in combination of the Mach-Zehnder 4×4 spatial multiplexer to show how the barrel shifter can re-order the shifted spectrum back to the original spectrum.

The simulated 4×4 Mach-Zehnder spatial multiplexer was analyzed separately from the microring resonator structure. The two structures were then combined to simulate barrel shifting. The power required to set the through switch-state was 150 mW applied to Heater 1. The same amount of power was applied to Heater 2 to set the cross switch-state. The configuration of the 4×4 Mach-Zehnder spatial multiplexer used to recover the original spectrum set MZI 1 to the through switch-state, set MZI 2 to the cross switch-state, set MZI 3 to the cross switch-state and set MZI 4 to the through switch-state. A single simulated 2×2 Mach-Zehnder interferometer had a -25 dB of crosstalk at 1550 nm.

The shifted spectrum from the microring resonators as shown in Fig. 5.8(b) was shifted back to the original ordering using the 4×4 Mach-Zehnder spatial multiplexer. The resulting output spectrum is shown in Fig. 5.8(c). Each output of the barrel shifter corresponds to a resonant wavelength of the original spectrum with the spectral artifacts compared to Fig. 5.8(a) a result of the two operations used to barrel shift.

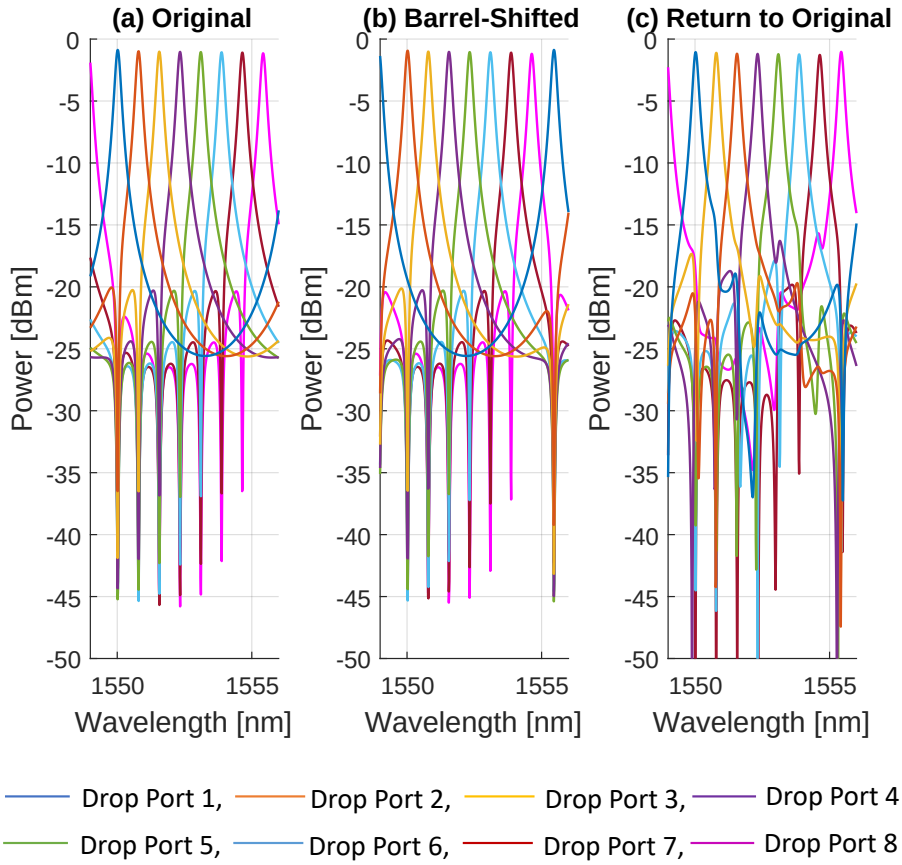

Figure 5.9: Simulated eight-channel barrel shifter spectra for (a) the original spectrum after the microring resonators, (b) the barrel shifted spectrum after the microring resonators and (c) the original ordering after the 8×8 Mach-Zehnder spatial multiplexer

8 Channel Barrel Shifter

The output spectrum from the eight-channel microrings before shifting is shown in Fig. 5.9(a). The resulting resonant wavelengths were 1550.02 nm, 1551.79 nm, 1551.56 nm, 1552.34 nm, 1553.15 nm, 1553.88 nm, 1554.65 nm, 1555.42 nm with a resonant wavelength separation of 0.77 nm. The same tuning efficiencies were observed as the four-channel barrel shifter. The resolved average free spectral range (FSR) was 6.53 nm, which is the same value as the four-channel barrel shifter. The barrel-shifted spectrum is shown in Fig. 5.9(b). The barrel-shifted spectrum was then shifted back to the original ordering using the 8×8 Mach-Zehnder spatial multiplexer with Mach-Zehnder interferometers configured to the states shown in Fig. 5.5. This spectrum is shown in Fig. 5.9(c). The average loss was -1 dB. The FWHM and Q-factors were approximately the same as the simulated four-channel barrel shifter.

5.4 Measured Performance Using Fabricated SiP Devices

This section discusses a barrel shifter using existing SiP structures. This design is based on a two stage structure that utilizes both wavelength selectivity and spatial multiplexing. Stage one was a set of coupled microring resonators [103], and stage two was a 4×4 Mach-Zehnder switch used as a spatial multiplexer [45, 66]. The combination of these devices was used to first barrel shift a set of four channels and then reverse shift the channels back to their original spectrum. These structures were not designed for barrel shifting. The set of coupled microrings was originally designed to work as an Add filter for an optical network. The Mach-Zehnder interferometer was designed to be used as a part of a spatial switch. However, both structures implement the functionalities required for a barrel shifter. Therefore, the experimental demonstration of barrel shifting using these devices is informative because it can highlight the design requirements for an optimized all-optical barrel shifter.

The first stage of the barrel shifter was implemented using a set of four coupled micror-

ings fabricated at Sandia National labs using 230 nm ridge waveguides where the waveguide width is varied from 400 nm to 800 nm about the major diameter of 29 µm. The second order microring resonators free spectral range (FSR) was 850 GHz so as to support a single channel of the 100 GHz ITU-T telecommunications grid. Each ring uses N-type dopant implants for the thermal resistive heaters. Because of the large radius of the rings, only a few nanometers of spectral shift can be realized from the thermal resistive heaters. The electrical control of the device was established via wirebonds to a printed circuit board (PCB). The $10\% - 90\%$ transition times as reported in [103] are 24 µs and 47 µs for the rise and fall transitions. The rings are operated between 0 V to 20 V. Given an average resistance of 3.8 kΩ, this corresponds to a maximum power of 210.6 mW for one set of coupled rings. This leads to a tuning efficiency of $0.0047\,\mathrm{nm\,mW^{-1}}$.

The second stage was implemented using a 4×4 SiP switch-chip fabricated at the Institute of Microelectronics (IME-A*STAR) Singapore using a standard 220 nm thick SiP platform [45, 66]. The switch-chip consists of four directional-coupler-based Mach-Zehnder interferometers arranged in a butterfly topology as seen in Fig. 5.1(b). The switch-chip resulted in a fairly broadband spectrum of 30 nm with a central wavelength around 1560 nm. Each Mach-Zehnder interferometer is composed of two 3 dB couplers and two waveguides that nominally create a passive differential phase of $\Delta\phi = \pi/2$.

To switch an input port to an output port, each Mach-Zehnder interferometer utilizes one thermal resistive heater on each arm and one current injection phase shifter on each arm. To ensure that the losses are kept to a minimum, the thermal heating elements are only used to actively tune the phases of each of the Mach-Zehnder interferometers. The heating elements for each Mach-Zehnder interferometer were controlled over an I2C bus from a thermal power supply board. Overall, the thermal tuning for each Mach-Zehnder interferometer is limited by a 4 V range leading to a maximum power consumption of 80 mW.

Several features of these devices made them non-ideal for barrel shifting. First, the

FSR of the fabricated microrings was 850 GHz, but each coupled microring resonator was only required to have a channel spacing of 100 GHz. Second, the on-device heaters could not shift the wavelength smoothly across the FSR. This was caused in part by the large radii of the coupled microrings. The combination of these nonidealities limited the functionality of the device so that a complete barrel shift of all four channels was not possible. This limitation is not fundamental and is an artifact of low Q-factor microrings and limited tuning range of fabricated devices used for the experimental characterization.

Measuring multiple SiP chips using multiple signal channels for both devices in series also required aligning multiple fiber arrays, amplifying the optical signal, and then applying post-amplification noise filtering. Therefore, to simplify this process, the optical response for each device was measured separately. The normalized response for each device was then combined to assess the performance of the barrel shifter.

5.4.1 Methods

For the fabricated devices, each output spectrum was measured separately using a similar set-up. Each spectrum was collected from 1552 nm to 1562 nm. Both devices were mounted on separate PCBs to allow for control of their individual heaters.

For the coupled microring resonators, the measurement set-up included a tunable laser inline with an active polarization scrambler. The output from the scrambler was aligned to the input bus waveguide of the chip using a standard fiber array coupler. The active polarization scrambler incurred an additional 3 dB loss and the fiber array used for the coupled microring resonator had an estimated coupling loss of 10 dB/facet. The Drop Port outputs were coupled back into the same fiber array and measured with a photodetector.

The on-chip heaters were wire-bonded such that each set of coupled microrings were tuned separately using a voltage source. Separate tuning was required in order to offset the overlapping spectral responses of the microrings. The voltages applied to each set of coupled

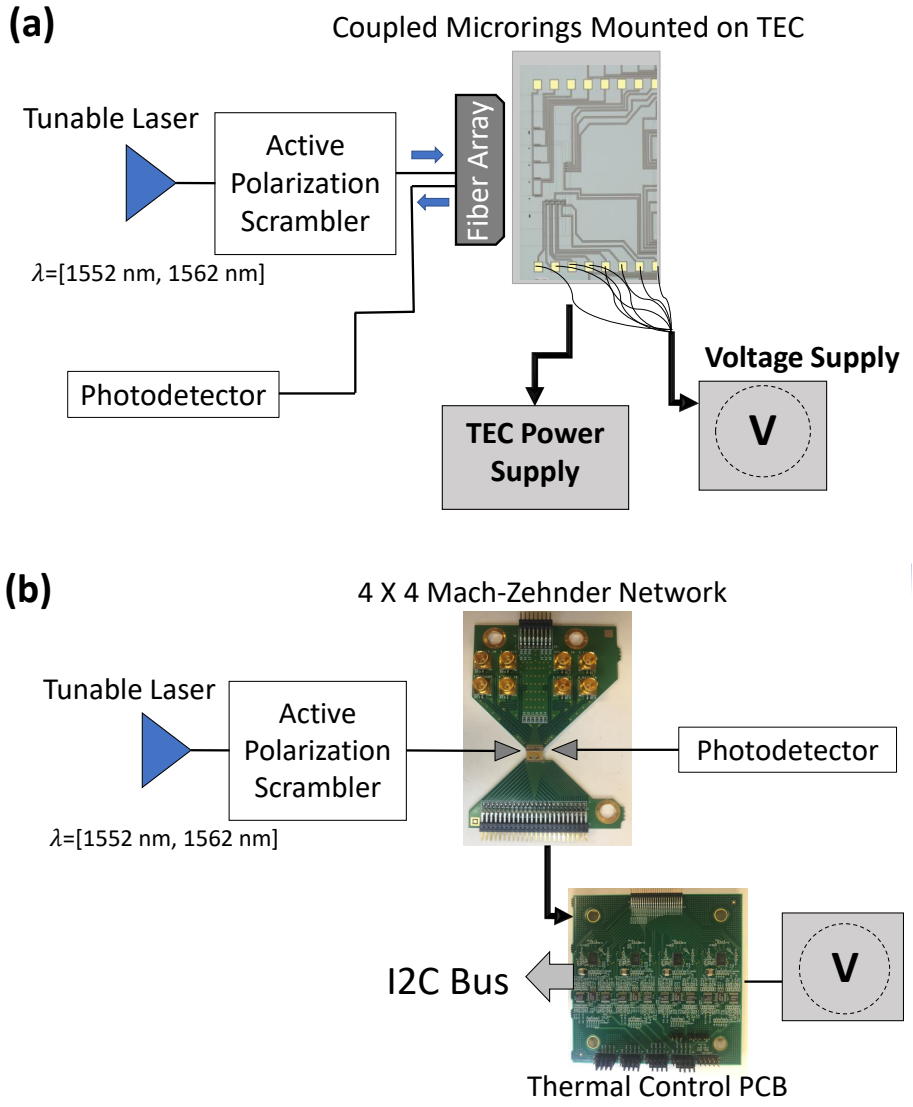

Figure 5.10: (a) Measurement set-up for the four-channel coupled microring resonators; (b) measurement set-up for 4×4 Mach-Zehnder spatial multiplexer.

microrings were 0 V, 10 V, 0 V and 20 V. The overall shift of the resonances was completed by externally heating the chip with a thermo-electric cooler (TEC). The estimated change in temperature inside each coupled microring for a complete barrel shift was $\Delta T \approx 50.57$ K. The calculation for the estimated change in temperature inside the coupled microrings is shown in Appendix F.

The 4×4 Mach-Zehnder spatial multiplexer was measured in the same manner. The major difference in set-up was a lensed fiber is edge-coupled to the input and output ports. For each input of the Mach-Zehnder 4×4 spatial multiplexer in the barrel-shifting configuration, all four outputs were measured. This results in 16 wavelength resolved spectra. The device was actively tuned to reverse shift using an I2C bus to control the thermal heating element on a PCB. The power applied to the Mach-Zehnders' heaters varied from 31 mW to 80 mW. The separate experimental characterization of each device was combined to assess the performance of the barrel shifter and to determine required device characteristics for barrel shifting. This was accomplished by using the normalized output spectrum of the 4×4 Mach-Zehnder spatial multiplexer as a filter placed after the barrel-shifted spectrum from the coupled microring resonators.

5.4.2 Results

The normalized spectrum from the coupled microrings before shifting, the barrel-shifted spectrum from the coupled microrings after shifting, and the spectrum after the 4×4 Mach-Zehnder spatial multiplexer are shown in Fig. 5.11. Slightly more loss was seen on the barrel-shifted spectrum. The normalized optical response of the 4×4 Mach-Zehnder spatial multiplexer in the barrel-shifting configuration is shown in Fig. 5.12. The measured crosstalk from the fabricated 4×4 Mach-Zehnder spatial multiplexer was used for the simulated Mach-Zehnder 4×4 spatial multiplexer.

The combined results of the normalized barrel shifted spectrum and the normalized filter response of the 4×4 Mach-Zehnder spatial multiplexer is shown in Fig. 5.11(c). An additional

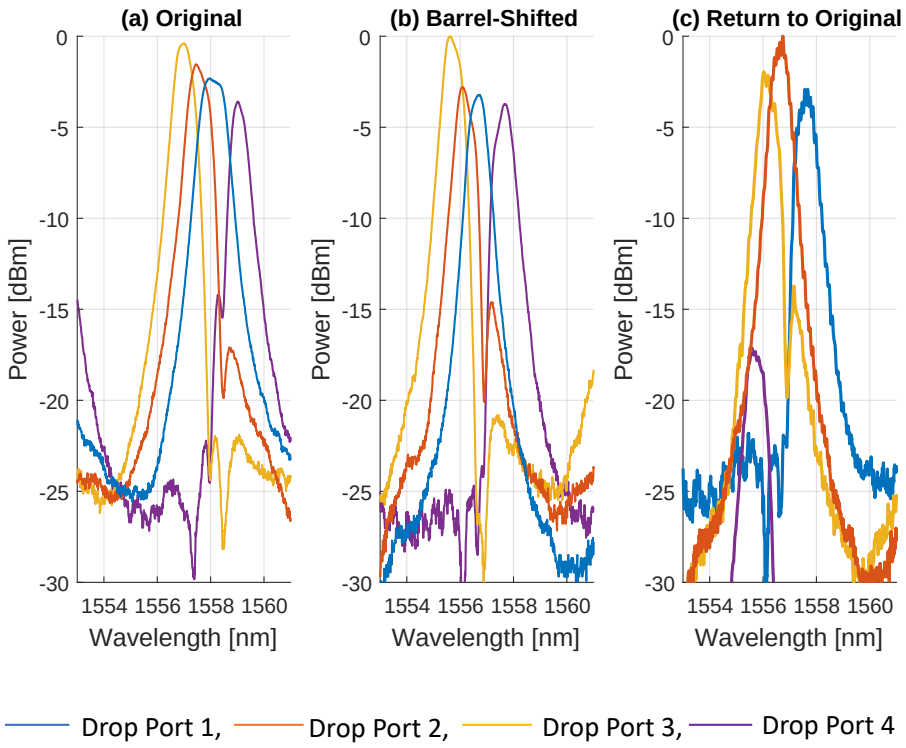

Figure 5.11: Measured four-channel barrel-shifted spectra for: (a) the original spectrum after the microring resonators, (b) the barrel-shifted spectrum after the microring resonators, and (c) the combined spectrum after the 4×4 Mach-Zehnder spatial multiplexer.

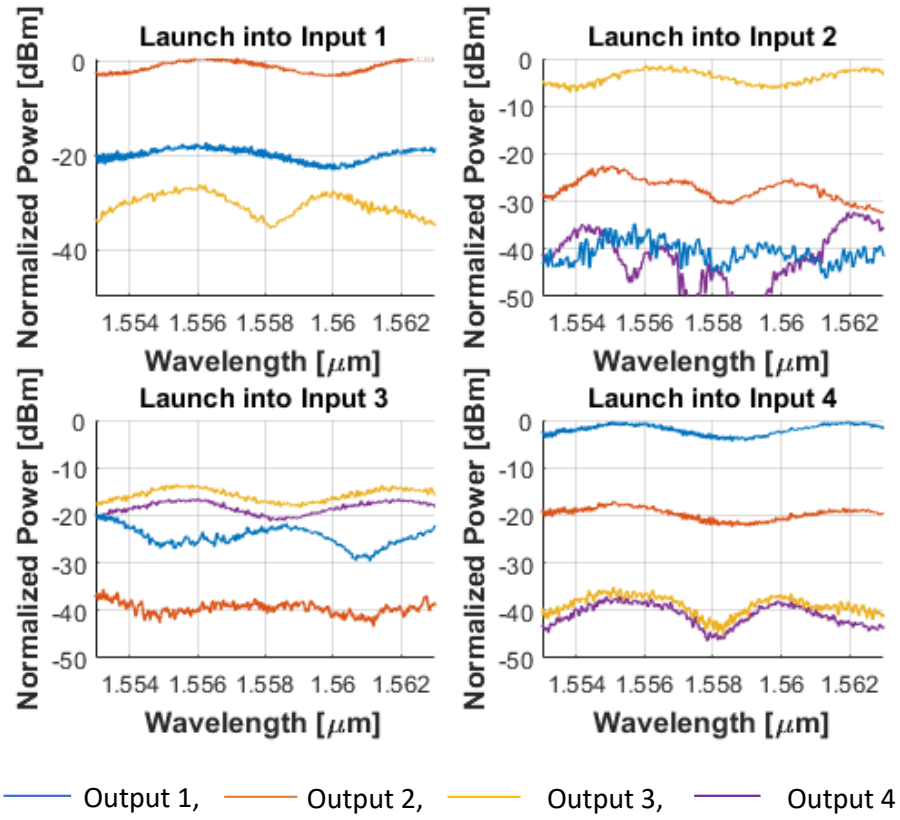

Figure 5.12: Measured normalized power spectrum of 4×4 Mach-Zehnder spatial multiplexer in the configuration that reverses the barrel shifting.

loss of $-20\,\text{dB}$ occurs on Output 4 of the 4×4 Mach-Zehnder spatial multiplexer, which results in Drop Port 4 having a significant loss as seen in Fig. 5.11(c).

The measurements of the fabricated devices are used in the next section to determine the required device characteristics to implement a practical all-optical barrel shifter utilizing both wavelength and spatial multiplexing.

5.5 Discussion

The unique functionality of barrel shifting presented in the previous section combines features of spatial multiplexing using Mach-Zehnder interferometers with the wavelength-selectivity of microrings. Three aspects of the simulated barrel shifter and the experimental characterization of SiP devices used to implement barrel shifting are discussed in this section. First, the crosstalk of the barrel shifters is discussed. Next, the scalability of the barrel-shifter architecture using a combination of microrings and Mach-Zehnder spatial multiplexer is compared to an alternative all-optical barrel shifter that is based on an all Mach-Zehnder interferometer spatial-multiplexed structure. Finally, the required device characteristics for a practical barrel shifter are discussed.

5.5.1 Crosstalk

The crosstalk of the simulated barrel shifter and the crosstalk of the fabricated device are discussed in this section. The crosstalk presented here is the combined crosstalk after the Mach-Zehnder network on each signal channel. The four-channel's simulated crosstalk is shown in Fig. 5.13. The eight-channel's simulated crosstalk is shown in Fig. 5.14. The crosstalk of the fabricated SiP device used to barrel shift is shown in Fig. 5.15.

As expected, the crosstalk of the simulated four-channel barrel shifter showed the best performance. When operating on resonance, the interchannel crosstalk varied from $-40\,\text{dB}$ to less than $-50\,\text{dB}$ over a $40\,\text{GHz}$ range about the resonance. The crosstalk was limited by the

spectral linewidth of the signal channel. When the device is operated off resonance, the crosstalk significantly increases. The maximum off-resonance crosstalk was $-25\,\text{dB}$ when the device was significantly off resonance. The sensitivity of the crosstalk to a tuning error can be reduced by using a flat-top filter as discussed in Section 5.2.

The crosstalk of the simulated eight-channel barrel shifter is slightly worse that the four-channel device. This is to be expected because more devices are used in the eight-channel design. When operating on resonance, the interchannel crosstalk varied from $-32.5\,\text{dB}$ to less than $-43\,\text{dB}$ over a $40\,\text{GHz}$ range about the resonance. The maximum off-resonance crosstalk was $-20\,\text{dB}$. Larger variation in the crosstalk for the simulated eight-channel barrel shifter is seen. This is due in part to the higher crosstalk in the 8×8 Mach-Zehnder spatial multiplexer.

Using a dilated Beneš topology or other strictly non-blocking, optical-switch topologies [104, 110] for the Mach-Zehnder-based spatial multiplexer would increase the device isolation and reduce the crosstalk. The trade-off to using these topologies compared to a blocking topology is the increased number of switch components. This increases the overall power consumption and insertion loss of the device.

The crosstalk using the fabricated SiP devices is shown in Fig. 5.15. The normalized crosstalk of the two devices varied between $-13\,\text{dB}$ to $-39\,\text{dB}$ over $40\,\text{GHz}$ about the resonance. This variation is caused by the spectral overlap of the optical resonances between the microrings. Proper separation of the signal channel resonances through a combination of smaller linewidths, using a flat-top filter response, and better thermal tuning should improve the crosstalk in such a device.

5.5.2 Scalable Designs

This section discusses the scalability of several all-optical SiP barrel shifter designs to large port-count systems. To assess the scalability, the simulated barrel shifter was compared to a non-blocking Beneš topology composed of 2×2 SiP Mach-Zehnder switch compo-

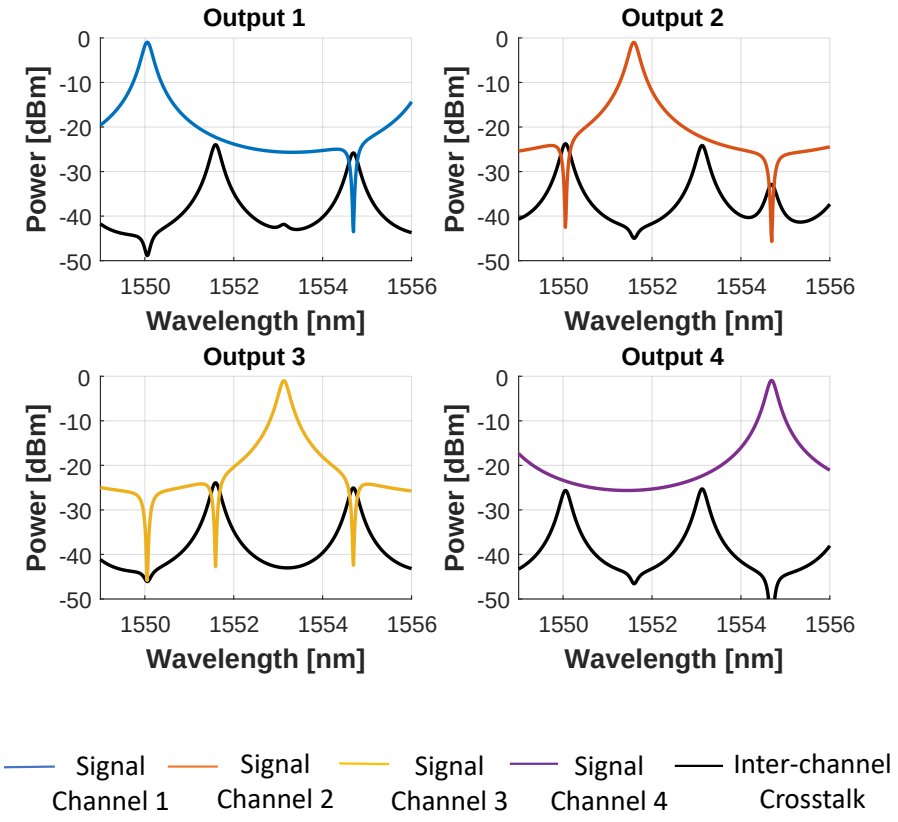

Figure 5.13: Simulated crosstalk for each output signal channel of a four-channel barrel shifter.

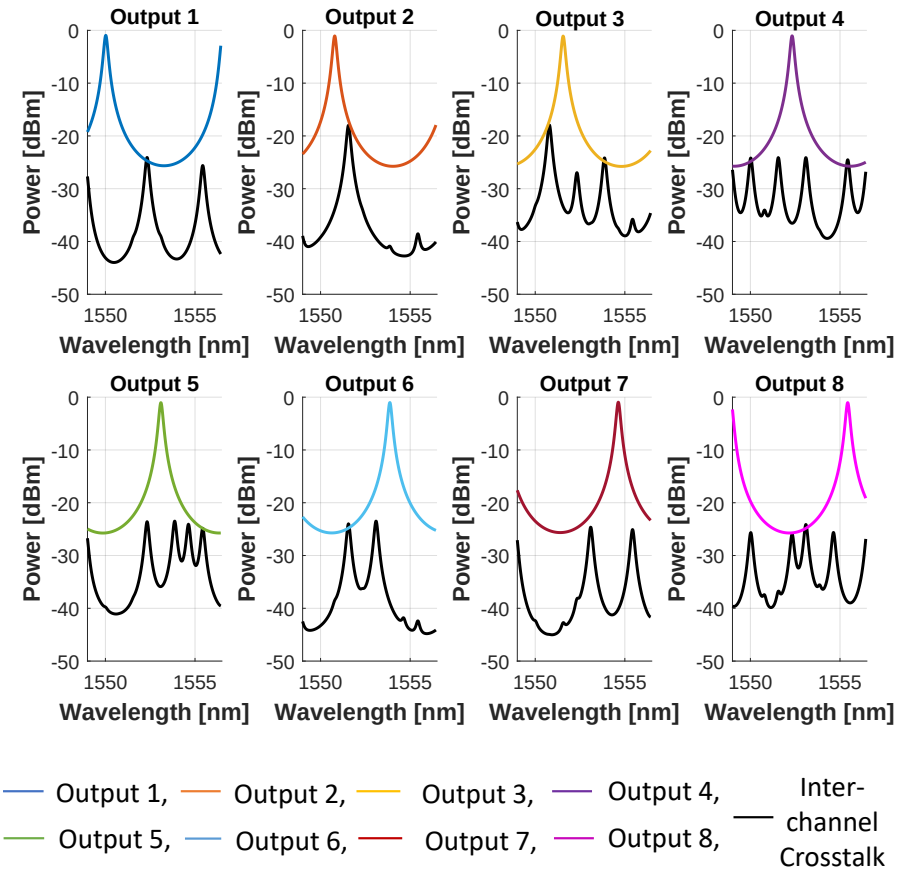

Figure 5.14: Simulated crosstalk for each output signal channel of an eight-channel barrel shifter.

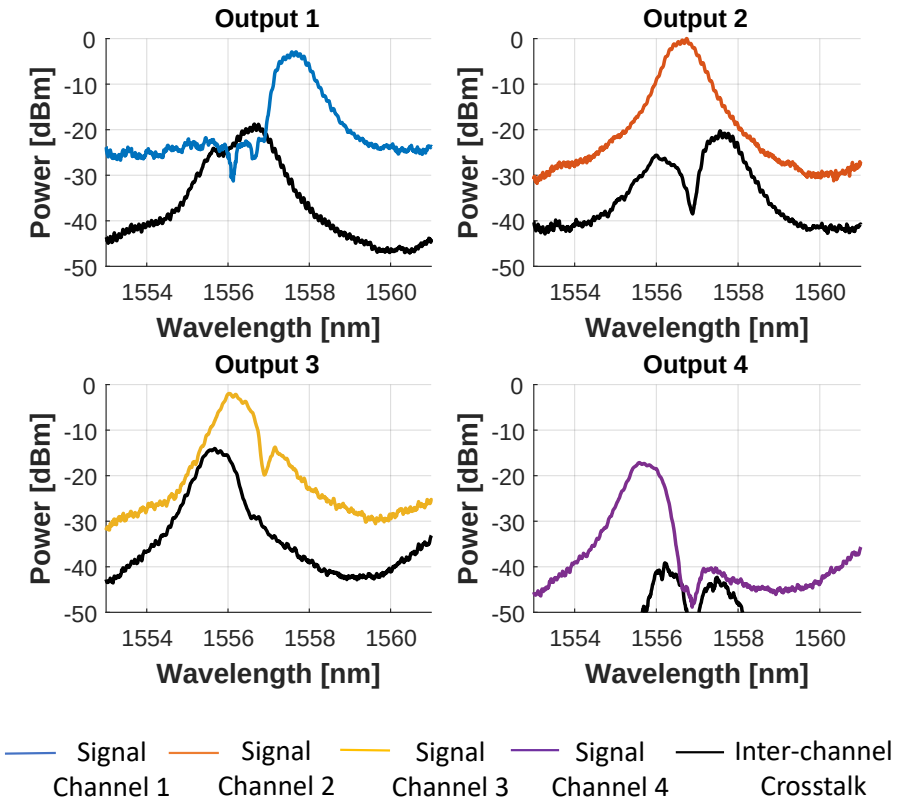

Figure 5.15: Measured crosstalk for each output signal channel of the barrel shifter based on fabricated SiP devices.

nents [104, 109, 110]. A non-blocking Beneš switch was deemed the most competitive choice because it offers minimal switch count and low-insertion loss. Using the same Mach-Zehnder interferometers and waveguide crossings that were used for the simulated barrel shifter, an 8×8 non-blocking Beneš switch was simulated in Lumerical. The insertion loss, switch count, worst-case crosstalk and waveguide crossing count for the eight-channel barrel shifter and the 8×8 non-blocking Beneš switch are compared in Table 5.1.

Table 5.1: A comparison of key proprieties for an 8×8 non-blocking Beneš switch versus the 8 channel (Ch.) barrel shifter

Property	8×8 Non-Blocking Beneš	8 Ch. Barrel Shifter
Insertion Loss	$-0.3\,$dB	$-1\,$dB
Switch Count	20	17
Worst-case crosstalk	$-16\,$dB	$-32.5\,$dB
Waveguide Crossing Count	16	8

Referring to Table 5.1, the simulated barrel shifter has three times the loss compared to the Beneš structure because of the insertion loss of the microrings. The barrel shifter has a lower switch count because the microring resonators are treated as one switch component which are set to all-off or all-on. The non-blocking Beneš has a much larger bandwidth of 30 nm compared to the 0.2 nm bandwidth of an isolated microring for an eight-channel design. This is offset by the microrings ability to tune the optical response over a larger wavelength range. The barrel shifter also has half the required waveguide crossings compared to a non-blocking Beneš switch. This leads to significantly less crosstalk when on resonance compared to the Beneš topology. This lower crosstalk is attributed to each microrings' capability to effectively isolate the desired wavelength from other wavelengths. In comparison, the signal to crosstalk ratio (SXR) in decibels (dB) for a non-blocking Beneš topology goes as

$$SXR \approx -X - 10\log_{10}(2\log_2 N - 1), \tag{5.2}$$

where X is the crosstalk for a single 2×2 component and N is the number of signal chan-

nels [104]. The signal to crosstalk ratio for the barrel shifter using the worst-case crosstalk goes as

$$SXR \approx -(X + CP) - 10\log_{10}(2\log_2 N - 2), \tag{5.3}$$

where CP in decibels (dB) is the crossover point between the spectral response of two microrings.

Experimental evidence of the enhanced isolation of a microring compared to a Mach-Zehnder interferometer is shown in Fig. 5.15(c). The crossover points for the measured barrel-shifter in Fig. Fig. 5.15(c) are -7 dB between Drop Port 1 and Drop Port 2, -15 dB between Drop Port 1 and Drop Port 3, and -3 dB between Drop Port 3 and Drop Port 2. This resulted in Drop Port 1 contributing -35 dB of on-resonance crosstalk to Signal Channel 2, Drop Port 2 contributing -40 dB of on-resonance crosstalk to Signal Channel 1, Drop Port 1 contributing -60 dB of on-resonance crosstalk to Signal Channel 3, Drop Port 3 contributing -55 dB of on-resonance crosstalk to Signal Channel 1, Drop Port 2 contributing -36 dB of on-resonance crosstalk to Signal Channel 3 and Drop Port 3 contributing -40 dB of on-resonance crosstalk to Signal Channel 2. Drop Port 4 was altered by a defect in the Mach-Zehnder network that resulted in Drop Port 4 having a lower output power. This resulted in Drop Port 4 being completely overlapped by Drop Port 3. Thus, Drop Port 4 contributes -15 dB of on-resonance crosstalk to Signal Channel 3.

These results suggest that for the same barrel shifter, a properly-designed microring architecture with a large turning range and good spectral isolation has significant advantages for large port-count systems compared to an architecture based on a Beneš topology. The practical realization of these advantages is driven by the required device characteristics.

5.5.3 Required Device Characteristics

Because the proposed barrel shifter design implements both wavelength demultiplexing and spatial multiplexing, a practical implementation of an all-optical barrel shifter in silicon photonics requires specific device characteristics. Applying practical constraints to these characteristics leads to design trade-offs. This section discusses some of these trade-offs.

With regard to the microrings, the characteristics of the coupled microring resonators used in the experimental characterization were far from ideal for the functionality of barrel shifting. The coupled microring resonators suffered from high insertion loss, poor channel isolation, and a limited wavelength tuning range.

The insertion loss of a SiP chip is due to a combination of factors that can be controlled during the design process and factors that may not be readily controllable with CMOS processing. One significant design characteristic that affects the insertion loss is the required number of ring elements. Fewer ring elements lead to lower loss, but may reduce the channel isolation resulting in increased crosstalk compared to using higher-order coupled microrings that have better channel isolation.

To improve the channel isolation, the required characteristics of the microring design include using an appropriate FSR and perhaps higher-order coupled microrings. Better channel isolation will reduce the spectral crossover point. Moreover, an appropriately designed FSR will improve barrel shifting functionality. We propose an FSR$= \Delta\lambda(N-1)$ is appropriate in order to reduce the required tuning between one resonance and a resonance in the next FSR over. In this case, $\Delta\lambda$ is the spacing between the resonant wavelengths and N is the number of desired channels. As discussed in Section 5.2, a higher-order microring filter offers a flat-top filter response that is less sensitive to random thermal tuning errors. However, this kind of filter has higher loss and is more sensitive to fabrication errors.

Implementing microring resonators with good thermal stability and a large tuning range is an outstanding issue for the entire field of silicon photonics [111]. This is true even when

an athermal design is used [112]. To improve the thermal tuning characteristics, the microring design used for the barrel shifter requires using metal-based heaters. These heaters have improved loss and tuning range. However, they have a slower response time compared to the implant-based heaters that were used in the fabricated devices. Thermal fluctuations from the heating also cause the Q-factor to degrade. This results in increased crosstalk and loss. For the simulated single microrings, the change in Q-factor as a function of temperature was calculated as $1.23\,\%/\mathrm{K}$. This large change as a function of the temperature shows the Q-factor of a single microring structure significantly degrades under a thermal load. In contrast, the coupled microring resonators are more resilient to thermal fluctuations but require more power to tune over a larger range.

5.6 Conclusion

Characterizing the class of functions that could be implemented optically is an important topic for the development of optimized SiP chips. This optimization can lead to higher bandwidth and lower power consumption compared to all-electronic solutions. This chapter has presented the design and simulation of one such function, which is a scalable all-optical barrel shifter implemented in silicon photonics using a combination of microrings and Mach-Zehnder interferometers. Both a four-channel and an eight-channel shifter were analyzed. The simulations indicate that a properly-designed hybrid barrel shifter has enhanced performance compared to a conventional design based on planar spatial multiplexers. Using appropriate SiP device characteristics, a barrel shifter can be designed to balance loss, thermal stability, and crosstalk. The experimentally validated device requirements for this functionality along with detailed simulations are a significant step towards establishing a general framework for co-optimized SiP chip solutions.

Chapter 5 in part, contains material, published in the following, of which the dissertation author

was the primary investigator:

H.R. Grant, S. Mookherjea and G. Papen, ”All-Optical Barrel Shifting using Silicon Photonics,” in-submission to *Journal of Lightwave Technology*, (2018).

Appendix A

Coupling Losses

There are two popular means of coupling light on and off silicon photonic (SiP) devices with optical fibers: grating-coupling or edge-coupling [113]. Coupling to free space optics and fiber tapers are other approaches, but these are not commonly used when packaging SiP devices for system-level applications [1]. Grating couplers use coherent periodic interfaces to couple light in and out of the top surface of the device. Typically, these structures are inherently limited in operational wavelength with high insertion losses and require non-planar packaging [1, 113]. The benefit of grating couplers is a relaxed alignment tolerance and the ability to implement them for wafer-scale testing. Edge couplers are the opposite. They are not spectrally-limited and allow for planar packaging. Edge-couplers do suffer from high sensitivity to misalignment and the inability to be readily used on wafer-scale testing. Given these attributes of these couplers, edge couplers are the primarily focus of this section.

This section will first overview optical edge-coupling on and off a SiP device using fibers and fiber arrays. The respective coupling losses for certain silicon-on-insulator (SIO) platforms are presented. While there are state-of-the-art optical coupling techniques, these techniques and components are not readily available in the market. This section purposely focuses on conventional coupling components for chip-level characterization.

A.1 Edge-coupling with Fibers

Fibers can be categorized as single mode fiber (SMF) or multimode fibers (MMF), polarization maintaining, connectors and spot-size converting mechanisms. In the context of Si-Photonics, most devices are fabricated for single mode operation, so multimode fibers are not considered in this section. There are polarization maintaining fibers which are more expensive. However, these maintain a specific polarization of the light propagating through the fiber. There are different connectors such as FC, which are common to found in photonic labs and LC, which are commonly found in datacenters [114].

Edge-coupling is when an optical mode from a fiber is coupled to the edge-facet of a waveguide [113]. In most cases, the waveguide is tapered at the edge of a SOI die. As mentioned this approach is not spectrally-limited and allows for the coupling optic to be glued to the facet of the device for on-axis packaging. However, major issues exist with edge-coupling that limit the stability and coupling losses. Typically issues arise with edge-coupling at the mode-field diameter of a typical single-mode fiber (SMF) is 9 µm, but the mode-field diameter of a waveguide is around 0.5 µm. This means there is an inherent mode-mismatch between the two optical components. Typically, the waveguides are tapered at the facet to increase the mode-field diameter, but this resolves a mode-field diameter of a few microns [1]. The optical mode-mismatch attributes to sensitivity in misalignment for edge-coupling. Improved fiber designs are used to match the mode-field diameter of the SiP facet and the fiber as discussed below.

The most important aspect of the optical fiber for the characterization of silicon photonic devices is the spot-size converting mechanisms. There are a few types of spot-size converting mechanisms used with optical fibers: conventional single-mode fibers, lensed fibers, tapered fibers, or high numerical aperture fibers. Both the conventional single-mode fibers and the high-numerical aperture fibers are cleaved surfaces. Lensed fibers have lenses at the tip of the optical fiber to reduce the optical mode size in the fiber. More commonly, lensed fibers are paired with

a tapered section to increase the amount of spot-size conversion. High numerical aperture fibers (HNA) use a high core-glass refractive index resulting in a mode-field diameter of 3 µm, which is close to the mode-field diameter of a reverse taper at the facet of a SiP device [115–117]. Table A.1 shows experimental coupling losses for various devices using either a lensed fiber, a lensed tapered fiber or a higher numerical aperture fiber. The devices' SOI thickness, facet quality and tapered waveguide width are listed. Conventional SMF are not listed as they are not commonly used for chip level characterization because of high coupling losses.

Table A.1: A comparison of coupling losses for different fibers to different SiP devices

Fiber Type	SOI Platform	Facet Quality	Tapered Waveguide Width	Coupling Loss
Lensed Tapered Fiber	220 nm	Polished	N/A	3 dB/facet
Lensed Tapered Fiber	230 nm	Botch-etched	190 nm	4 dB/facet
Lensed Fiber	E-beam 220 nm	Diced	150 nm	5 dB/facet
HNA [117]	230 nm	Diced	180 nm	7 dB

A.2 Edge-Coupling with Fibers arrays

Optical Fiber arrays are also increasingly more common with SiP devices. These components are a solution to coupling light off and on a device with multiple port counts. Fiber arrays were first introduced in the 1980s [118]. the ability to etch v-grooves into silicon was a major innovation for this technology [119, 120]. As Silicon Photonics grows, the development of these products to allow for robust packaging is an ever growing field [35].

There are different types of fiber arrays. Some are commonly standardized while others a less likely. As mentioned, the use of V-grooves etched into a substrate (silicon or glass) has been the standard way of fabricating fiber arrays. An example of a v-groove fiber array with a 127 µm pitch on a silicon substrate is shown in the left-hand side of Fig. A.1. The cross-section of a similar v-groove fiber array on a glass substrate is presented in the right-hand side of Fig A.1. Individual fibers placed into individual grooves that are shaped like a V are shown with a

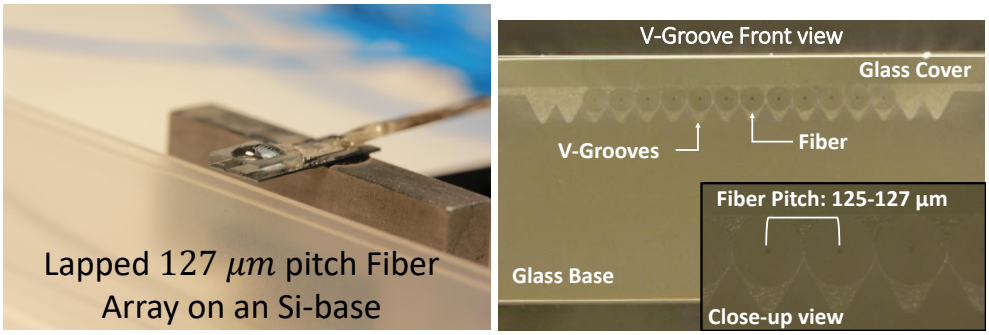

Figure A.1: V Groove array

glass lid. The fiber array presented in this image was an OZ Optics Fiber array and a full picture of a similar fiber array but on a Si substrate is shown in Fig. The fibers used are conventional SMF-28, but polarization maintaining fibers can be used in fiber arrays for a significant cost increase. For a 230 nm SI platform from Sandia National Labs with tapered waveguides at the edge of the device, the coupling losses using these fiber arrays were shown to be 10 dB/facet.

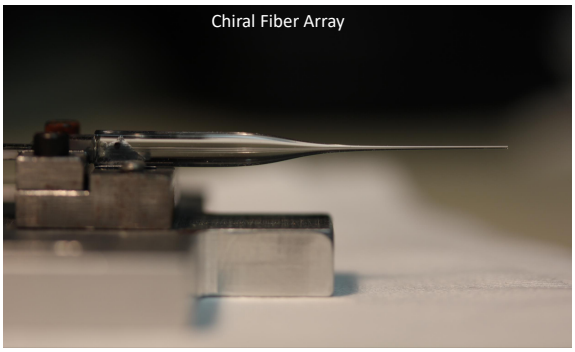

Figure A.2: Chiral array

There are other less conventional edge-coupling fiber arrays. Presented in Fig. A.2 is a Chiral Optics Pitch Reducing Fiber array that takes fibers at a 225 µm spacing and reduced the fiber spacing to 25 µm [74]. Using a standard 220 nm platform from IME with a tapered waveguide width of 180 nm, these coupling losses were reported at 5 dB/facet – 6 dB/facet.

The coupling losses for these devices present a significant disadvantage to fiber arrays without considering the alignment complexity. With standard fiber arrays, a mode mismatch between the individual fibers and the individual waveguides is usually present. Additionally,

fabrication variations and misalignment can occur that will only heighten the modal mismatch presented.

Appendix B

Parameterized Average Coupling Coefficient

The numerical solution for the average coupling coefficient can be parameterized by the following equation [121]

$$L_C(\lambda) \doteq (a(\lambda - \lambda_o) + b) \exp\left[\frac{g}{c(\lambda - \lambda_o) + d}\right]. \tag{B.1}$$

There are four empirical coefficients a, b, c, and d as well as the gap g of the coupler and the wavelength λ_0 for which the coupled power in each arm is equal. This wavelength λ_0 is called the 3 dB coupling wavelength. Because the device is designed such that each coupler operates as a 3 dB splitter, the interaction length L is designed such $\kappa(\lambda_0)_{\text{avg}} = 1/2$. This means on average, $L/L_C = 1/2$. To verify this approximation, the ratio of L/L_C was used as a fit parameter. The resulting fit gave $L/L_C = 1/2.07$, which is close to the presumed value of $1/2$. Therefore, the number of parameters describing $\kappa(\lambda)_{\text{avg}}$ can be simplified by reducing absolute numbers to the ratios a/b, c/d, and g/d so that

$$\kappa(\lambda)_{\text{avg}} = \sin\left(\frac{\pi}{4}\frac{1}{a/b(\lambda-\lambda_0)+1} \times \exp\left(g/d\frac{c/d(\lambda-\lambda_0)}{c/d(\lambda-\lambda_0)+1}\right)\right)^2. \tag{B.2}$$

Appendix C

Linear Dependence of the Differential Phase

The linear dependence of the differential phase with respect to wavelength is approximated by a power series expansion of the $\Delta\phi(\lambda) = 2\pi n(\lambda)\Delta L\Gamma/\lambda$ about a central wavelength λ_0, where $f(\lambda) = \Delta\phi(\lambda)$. The wavelength dependence of the index is considered to be dominated by the inverse wavelength dependence of the phase with other terms treated as constants.

Expanding $\Delta\phi(\lambda) = 2\pi n\Delta L\Gamma/\lambda$ in a power series gives

$$\phi(\lambda_0 + \Delta\lambda) = \frac{2\pi n\Delta L\Gamma}{\lambda_0} - \left[\frac{2\pi n\Delta L\Gamma}{\lambda_0^2}\right](\Delta\lambda),$$

which simplifies to

$$\phi(\lambda_0 + \Delta\lambda) = \Delta\phi(\lambda_0)\left(1 - \frac{\Delta\lambda}{\lambda_0}\right). \tag{C.1}$$

For $\lambda_0 = 1560\,\text{nm}$ and a range of wavelength of $\lambda_0 \pm 50\,\text{nm}$ about λ_0, the relative error in using a linear approximation is .11%

Appendix D

Determination of Parameter Bounds

In order to establish reasonable bounds for each parameter of the model prior to running a fit, m test fits each with a set of random initial estimates are run with every parameter varied at once for $m \leq 1000$. For each run, the bounds on the parameters are relaxed until a solution converges within the range defined by those bounds. This procedure is used for the coupling coefficient and $\mathrm{d}\phi/\mathrm{d}\lambda$.

The bounds on others parameters are determined using the physical properties of the parameter. This is the case for the excess loss α_n, where the transmission cannot be greater than the input power of 1 mW, or the differential phase, which is bounded by $[0, 2\pi]$.

D.1 Coupling Coefficient

For the average coupling coefficient $\kappa(\lambda)$ as given in Equation B.2, there are four parameters: the 3 dB coupling wavelength, λ_0, and three weighting coefficients, a/b, c/d and g/d. An initial estimate of 1560 nm for the 3 dB wavelength λ_0 can be obtained from the passive switch-state measurements shown in Figure 4.3. This value for λ_0 is left as a fixed value in the model. The initial estimates for the three other coupling coefficient terms are chosen from the initial device design.

D.2 Differential Phase

The four measured output powers for each passive input shown in Figure 4.3 are used to determine the initial estimate for the passive differential phase term $\Delta\phi_0$ for the nth MZi. Going in numerical order of MZis as shown in Figure 4.1, MZi_1 is in its through state, with $\Delta\phi_1 = \pi$. This state for MZi_1 is assumed since the maximum output powers for Input 1 are at Outputs 1 and 2 and the maximum output power for Input 2, are Outputs 3 and 4. The same reasoning for MZi_1 can be applied to MZi_2. This similar reasoning shows MZi_2 to be in its cross state, $\Delta\phi_2 = 0$, where Input 4 shows the highest power transfer to Outputs 1 and 2 while Input 3 shows the highest power transfer to Output 3. Next, MZi_3 is likely in its quadrature point where $\Delta\phi_3 = \pi/2$. This assumption can be made on the fact that Outputs 1 and 2 are always at the same output power. A defect of about -20 dB is noticed on Output 4, which affects the initial estimate for MZi_4, but it was estimated to be near the quadrature point with $\Delta\phi_4 = \pi/2$. The initial estimates for $\Delta\phi_n$ are shown in Table 4.2. This defect is a fit parameter α_{Output4}.

The initial estimates for the rate of change in the differential phase with respect to the wavelength $d\phi/d\lambda$ is extracted from modeling a passive waveguide cross-section in Lumerical [24]. This model does not include the active components such as the resistive heaters or PIN phase shifters.

D.3 Loss

Since the straight-waveguide is used to characterize the on-off chip loss, α_n is used to determine the structure-dependent excess loss for each MZi. This value is assumed to be less than the on-off chip loss.

D.4 Active Parameters

The device is biased so that the differential active phase terms are are close to the quadrature point such that $\Delta\phi_0(V) = \pi/2$. Because the dispersion in silicon as a function of temperature is small [122], the rate of change of the active switch-state differential phase $d\phi_n(V)/d\lambda$ for the active state is nearly the rate of change of the passive switch-state differential phase $d\phi/d\lambda$ of the passive switch-state.

Appendix E

Calculations of Quality Factor Versus Temperature

As mentioned in Chapter 5, the worst case change in quality factor (Q-factor) as a function of temperature was calculated for a single add/drop microring resonator. The microrings had a passive power coupling coefficient of $\kappa^2 = .1$ and a waveguide loss of $3\,\mathrm{dB\,cm^{-1}}$. The Q-factor was calculated for FSRs of 1 nm, 2 nm, 6 nm, and 10 nm. The calculations used simulations from Chapter 5.

First, the effective index n_{eff} and group index n_g as a function of temperature are extracted using Lumerical Mode. The details of this simulation is shown in Chapter 5. The extracted $n_{\mathrm{eff}}(T)$ and $n_g(T)$ are shown in Fig. E.1.

To determine the quality factor, the transmission coefficient t of the coupling regions as a function of temperature first needs to be determined. The transmission coefficient t_O when no temperature is applied is given as

$$t_O^2 + \kappa^2 = 1 \tag{E.1}$$

and κ is the coupling coefficient [1, 57]. Using an eigenmode expansion method, the transmission coefficient as a function of index can calculated as [1, 57]

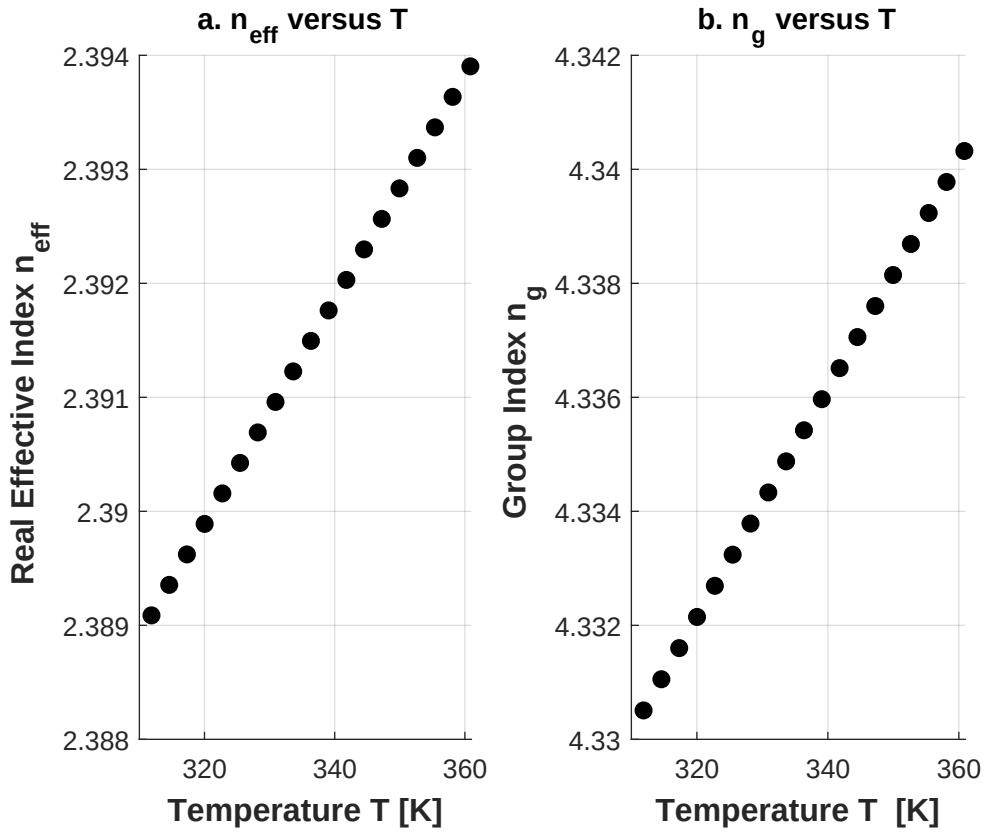

Figure E.1: Extracted effective index n_{eff} and group index n_g used in the Q-factor versus temperature calculations.

$$t^2 = \cos^2 \frac{\pi * \Delta n}{\lambda} L \tag{E.2}$$

where Δn is the difference in effective indices between the two supermodes of a coupling region, λ is the operating wavelength and L is the physical length of the coupling regions. In this case, $L = 10\,\mu\text{m}$. Knowing t_O, λ and L, a passive Δn can be calculated.

Next, a temperature dependent transmission coefficient is then determined. This is done by using the calculated passive Δn and the change in $n_{\text{eff}}(T)$ as a function of temperature to calculate $t(T)$. This can be shown as

$$t(T)^2 = \cos^2 \frac{\pi(\Delta n + \Delta n(T)}{\lambda} L \tag{E.3}$$

where $\Delta n(t)$ is the change in index as a function of temperature being added to the passive Δn to account for the change in index from thermal fluctuations. It should be noted that this is for the worst case scenario where the index inside the ring is only altered by the change in temperature and not the waveguide the ring couples with.

Finally, the temperature dependent group index $n_g(T)$ and the temperature dependent transmission coefficient $t(T)$ are used to calculate the Q-factor as a function of temperature. The functional form of the Q-factor [1] was augmented to depend on $n_g(T)$ and $t(T)$. This is done by calculating an intrinsic Q-factor $Q_i(T)$ as given by

$$Q_i(T) = \frac{2\pi n_g(T)}{\lambda \alpha} \tag{E.4}$$

where α is the propagation loss in m^{-1} and a coupling-dependent Q-factor $Q_c(T)$ as given by

$$Q_c(T) = -\frac{\pi L_{\text{rt}} n_g(T)}{\lambda \ln |t(T)|} \tag{E.5}$$

where L_{rt} is the round-trip length of the microring resonator. This is determined by the resonance condition for the specified FSRs where $L_{\text{rt}} = \lambda^2/(n_g * FSR)$. For simplicity reasons, L_{rt} was not varied as a function of thermal expansion. From here, a total Q-factor ($Q_{\text{total}}(T)$) is calculated a combination of $Q_i(T)$ and $Q_c(T)$ as given by

$$\frac{1}{Q_{\text{total}}(T)} = \frac{1}{Q_c(T)} + \frac{1}{Q_i(T)}. \tag{E.6}$$

Using Eq. E.6, the Q-factor as a function of temperature is calculated and plotted for each specified FSR. These Q-factors are shown in Fig. E.2.

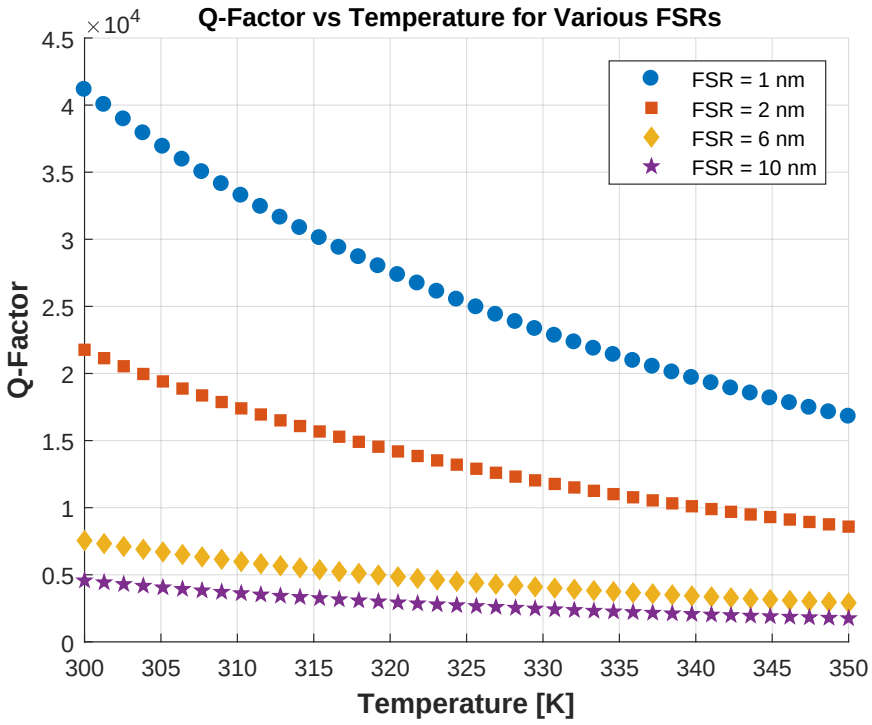

Figure E.2: Simulated Q-factor of a microring resonator that is heated by $\Delta T = 50\,\%$ with respect to various microring FSRs

Appendix F

Calculation of the Thermal Shift in a Microring Resonator

This appendix will demonstrate the calculations for the temperature inside a microring resonator when heated by an external source as reported in Chapter 5. This calculation relies on the difference in the propagation coefficients $\Delta\beta$ for a resonant condition.

To calculate the temperature inside a resonant structure when heated by an external source, the effective index of the waveguide at the applied temperature is first estimated. In this case, a cross-section of a fully-etched 500 nm wide waveguide on a 230 nm SOI platform is simulated in Lumerical Mode to extract the effective index n_1. In this case, $n_1 = 2.457$. Since $\beta = 2\pi n/\lambda$, the difference in β between the first resonance and the shifted resonance can be used to calculate the shift in index. In this case, $\Delta\beta = 0$ is assumed for a shifted resonance. This assumes the next resonance is shifted to be the same order of the roundtrip phase. With this assumption, a relation for the change in index Δn can be determined as given by

$$\Delta n = \Delta\lambda \frac{n_1}{\lambda_1}. \tag{F.1}$$

Where $\Delta\lambda$ is the shift in wavelength and $lambda_1$ is the initial wavelength. Given the

FSR of the rings $\Delta\lambda = 7\,\text{nm}$ with $\lambda_1 = 1559\,\text{nm}$, Δn can be calculated.

Using the relation for the change in index in silicon as a function of temperature, $dn/dT = 1.87 \times 10^{-4}\,\text{K}^{-1}$ for silicon, the temperature inside the ring can be estimated to be

$$\Delta T = \frac{\Delta n}{\frac{dn}{dT}} \approx 50.57K. \tag{F.2}$$

Bibliography

[1] L. Chrostowski and M. Hochberg, *Silicon Photonics Design: From Devices to Systems*. Cambridge University Press, 2015.

[2] R. Aguinaldo, A. Forencich, C. DeRose, A. Lentine, D. C. Trotter, Y. Fainman, G. Porter, G. Papen, and S. Mookherjea, "Wideband silicon-photonic thermo-optic switch in a wavelength-division multiplexed ring network," *Opt. Express*, vol. 22, pp. 8205–8218, Apr 2014.

[3] M. Hochberg and T. Baehr-Jones, "Towards fabless silicon photonics," *Nature Photonics*, vol. 4, pp. 492 EP –, Aug 2010.

[4] B. G. Lee, A. V. Rylyakov, W. M. Green, S. Assefa, C. W. Baks, R. Rimolo-Donadio, D. M. Kuchta, M. H. Khater, T. Barwicz, C. Reinholm, E. Kiewra, S. M. Shank, C. L. Schow, and Y. A. Vlasov, "Monolithic silicon integration of scaled photonic switch fabrics, CMOS logic, and device driver circuits," *Journal of Lightwave Technology*, vol. 32, no. 4, pp. 743–751, 2014.

[5] W. Bogaerts, R. Baets, P. Dumon, V. Wiaux, S. Beckx, D. Taillaert, B. Luyssaert, J. V. Campenhout, P. Bienstman, and D. V. Thourhout, "Nanophotonic waveguide in silicon-on-insulator fabricated with cmos technology," *J. Lightwave Technol.*, vol. 23, no. 1, pp. 401–412, 2005.

[6] C. Doerr and K. Okamoto, "Advances in silica planar lightwave circuits," *J. Lightwave Technol.*, vol. 24, no. 12, pp. 4763–4789, 2006.

[7] R. Soref, "The past, present, and future of silicon photonics," *IEEE Journal of Selected Topics in Quantum Electronics*, vol. 12, no. 6, pp. 1678–168, 2006.

[8] M. Heck, "Hybrid silicon photonic integrated circuit technology," *IEEE Journal of Selected Topics in Quantum Electronics*, vol. 20, no. 4, 2014.

[9] W. Bogaerts, M. Fiers, and P. Dumon, "Design challenges in silicon photonics," *IEEE Journal of Selected Topics in Quantum Electronics*, vol. 20, no. 4, 2014.

[10] Cisco, "Cisco visual networking index: Global mobile data traffic forecast update, 20162021 white paper," 2017.

[11] M. Taubenblatt, "Optical interconnects for high-performance computing," *J. Lightwave Technol.*, vol. 30, no. 4, pp. 448–458, 2012.

[12] A. Wilner, "All-optical signal processing," *J. Lightwave Technol.*, vol. 32, no. 4, 2014.

[13] U. Y., N. T., and A. Y., "Silicon optical interposers for high-density optical interconnects," in *Silicon Photonics III* (P. L. and L. D., eds.), ch. 1, pp. 266–290, Berlin, Heidelberg: Springer, 2016.

[14] D. F. Feng, J. L. Luff, S. Jatar, and M. Asghari, "Micron-scale silicon photonic devices and circuits," in *Optical Fiber Communication Conference*, p. Th4C.1, Optical Society of America, 2014.

[15] C. Doerr, L. Chen, D. Vermeulen, T. Nielsen, S. Azemati, S. Stulz, G. McBrien, X. M. Xu, B. Mikkelsen, M. Givehchi, C. Rasmussen, and S. Y. Park, "Single-chip silicon photonics 100-gb/s coherent transceiver," in *OFC 2014*, pp. 1–3, March 2014.

[16] F. Boeuf, S. Cremer, E. Temporiti, M. Fere, M. Shaw, N. Vulliet, B. Orlando, D. Ristoiu, A. Farcy, T. Pinguet, A. Mekis, G. Masini, P. Sun, Y. Chi, H. Petiton, S. Jan, J. R. Manouvrier, C. Baudot, P. Le Maitre, J. F. Carpentier, L. Salager, M. Traldi, L. Maggi, D. Rigamonti, C. Zaccherini, Elemi, B. Sautreuil, and L. Verga, "Recent progress in silicon photonics r amp;d and manufacturing on 300mm wafer platform," in *2015 Optical Fiber Communications Conference and Exhibition (OFC)*, pp. 1–3, March 2015.

[17] K. Bergman, "Silicon photonics for high performance interconnection networks," in *Optical Fiber Communication Conference*, p. Tu3F.1, Optical Society of America, 2018.

[18] E. Anderson, A. Gazman, Z. Zhu, M. Hattink, and K. Bergman, "Reconfigurable silicon photonic platform for memory scalability and disaggregation," in *Optical Fiber Communications Conference (OFC)*, p. Tu3F.3, OSA, 2018.

[19] Y. Shen, A. Gazman, Z. Zhu, M. Y. Teh, M. Hattink, S. Rumley, P. Samadi, and K. Bergman, "Autonomous dynamic bandwidth steering with silicon photonic-based wavelength and spatial switching for datacom networks," in *Optical Fiber Communication Conference*, p. Tu3F.2, Optical Society of America, 2018.

[20] C. V. Poulton, A. Yaacobi, D. B. Cole, M. J. Byrd, M. Raval, D. Vermeulen, and M. R. Watts, "Coherent solid-state lidar with silicon photonic optical phased arrays," *Opt. Lett.*, vol. 42, pp. 4091–4094, Oct 2017.

[21] R. Aguinaldo, *Silicon photonics with applications to data center networks*. PhD thesis, University of California San Diego, 2014.

[22] S. Assefa, "Monolithic integration of cmos and silicon nanophotonics for optical interconnects," in *Frontiers in Optics 2012/Laser Science XXVIII*, p. FTu2A.1, Optical Society of America, 2012.

[23] COMSOL, "Understand, predict, and optimize engineering designs with the comsol multiphysics®software," 2018.

[24] Lumerical, "Silicon photonics and integrated optics," 2018.

[25] R. Cao, J. Billoudet, J. Ferguson, L. Couder, J. Cayo, A. Arriordaz, and I. O'Connor, "Lvs check for photonic integrated circuits 2014 curvilinear feature extraction and validation," in *2015 Design, Automation Test in Europe Conference Exhibition (DATE)*, pp. 1253–1256, March 2015.

[26] Cadence, "Photonics integrated electronics/photonic design automation environment," 2018.

[27] M. Bahadori, S. Rumley, H. Jayatilleka, K. Murray, N. A. F. Jaeger, L. Chrostowski, S. Shekhar, and K. Bergman, "Crosstalk penalty in microring-based silicon photonic interconnect systems," *J. Lightwave Technol.*, vol. 34, pp. 4043–4052, Sep 2016.

[28] S. Nakamura, S. Yanagimachi, H. Takeshita, A. Tajima, T. Hino, and K. Fukuchi, "Optical switches based on silicon photonics for roadm application," *IEEE Journal of Selected Topics in Quantum Electronics*, vol. 22, pp. 185–193, Nov 2016.

[29] M. A. Popovíc, T. Barwicz, M. R. Watts, P. T. Rakich, L. Socci, E. P. Ippen, F. X. Kärtner, and H. I. Smith, "Multistage high-order microring-resonator add-drop filters," *Opt. Lett.*, vol. 31, pp. 2571–2573, Sep 2006.

[30] D. A. Miller, "Are optical transistors the logical next step?," *Nature Photonics*, vol. 4, no. 3, 2010.

[31] P. G.B., *Silicon Photonics Packaging Automation: Problems, Challenges, and Considerations*, ch. 8, pp. 237–259. Berlin, Heidelberg: Springer Berlin Heidelberg, 2016.

[32] L. Carroll, J.-S. Lee, C. Scarcella, K. Gradkowski, M. Duperron, H. Lu, Y. Zhao, C. Eason, P. Morrissey, M. Rensing, S. Collins, H. Hwang, and P. O'Brien, "Photonic Packaging: Transforming Silicon Photonic Integrated Circuits into Photonic Devices," *Applied Sciences*, vol. 6, no. 12, p. 426, 2016.

[33] D. Thomson, A. Zilkie, J. Bowers, T. Komljenovic, G. Reed, L. Vivien, D. Marris-Morini, E. Cassan, L. Virot, J. Fdli, J. Hartmann, J. Schmid, D. Xu, F. Boeuf, P. OBrien, G. Z. Mashanovich, and M. Nedeljkovic, "Roadmap on silicon photonics," *Journal of Optics*, vol. 18, no. 7, p. 073003, 2016.

[34] H. Y. Hwang, J. S. Lee, T. J. Seok, A. Forencich, H. R. Grant, D. Knutson, N. Quack, S. Han, R. S. Muller, G. C. Papen, M. C. Wu, and P. O'Brien, "Flip chip packaging of digital silicon photonics mems switch for cloud computing and data centre," *IEEE Photonics Journal*, vol. 9, pp. 1–10, June 2017.

[35] P. O'Brien, L. Carrol, C. Eason, and J. S. Lee, *Packaging of Silicon Photonic Devices*, pp. 217–236. Berlin, Heidelberg: Springer Berlin Heidelberg, 2016.

[36] Mellanox, "Inside the silicon photonics transceiver," 2015.

[37] Chiral, "Fiber coupler overview," 2016.

[38] T. Barwicz, Y. Taira, T. W. Lichoulas, N. Boyer, Y. Martin, H. Numata, J. W. Nah, S. Takenobu, A. Janta-Polczynski, E. L. Kimbrell, R. Leidy, M. H. Khater, S. Kamlapurkar, S. Engelmann, Y. A. Vlasov, and P. Fortier, "A novel approach to photonic packaging leveraging existing high-throughput microelectronic facilities," *IEEE Journal on Selected Topics in Quantum Electronics*, vol. 22, no. 6, 2016.

[39] T. Barwicz, A. Janta-Polczynski, S. Takenobu, J.-F. Morissette, B. Peng, Y. Taira, H. Numata, S. Kamlapurkar, S. Engelmann, P. Fortier, and N. Boyer, "A compliant polymer interface with 1.4db loss between standard fibers and nanophotonic waveguides," in *Frontiers in Optics 2016*, p. FTu1D.2, Optical Society of America, 2016.

[40] S. Lin, *Demonstration of an Optical Chip-to-Chip Link in a 3D Integrated Electronic-Photonic Platform*. PhD thesis, University of California at Berkeley, 2017.

[41] E. R. H. Fuchs, E. J. Bruce, R. J. Ram, and R. E. Kirchain, "Process-based cost modeling of photonics manufacture: the cost competitiveness of monolithic integration of a 1550-nm dfb laser and an electroabsorptive modulator on an inp platform," *Journal of Lightwave Technology*, vol. 24, pp. 3175–3186, Aug 2006.

[42] D. Celo, D. J. Goodwill, J. Jiang, P. Dumais, C. Zhang, F. Zhao, X. Tu, C. Zhang, S. Yan, J. He, M. Li, W. Liu, Y. Wei, D. Geng, H. Mehrvar, and E. Bernier, "32×32 silicon photonic switch," in *2016 21st OptoElectronics and Communications Conference (OECC) held jointly with 2016 International Conference on Photonics in Switching (PS)*, pp. 1–3, July 2016.

[43] S. Suda, H. Matsuura, K. Tanizawa, K. Suzuki, K. Ikeda, H. Kawashima, and S. Namiki, "Fast and accurate automatic calibration of a 32×32 silicon photonic strictly-non-blocking switch," in *Advanced Photonics 2017 (IPR, NOMA, Sensors, Networks, SPPCom, PS)*, p. PTu3C.5, Optical Society of America, 2017.

[44] H. R. Grant, G. Papen, S. Mookherjea, B. G. Lee, and L. Schares, "Heuristic characterization of si-photonic switches," in *Advanced Photonics 2017 (IPR, NOMA, Sensors, Networks, SPPCom, PS)*, p. PTu3C.1, Optical Society of America, 2017.

[45] H. R. Grant, A. Forencich, G. Papen, N. Dupuis, L. Schares, R. A. Budd, and B. G. Lee, "Bit error rate measurements of a 4×4 si-photonic switch using synchronous and asynchronous data," in *2016 IEEE Optical Interconnects Conference (OI)*, pp. 32–33, May 2016.

[46] J. Networks, "100-gigabit ethernet 100gbase-r optical interface specifications," 2017.

[47] D. A. B. Miller, "Device requirements for optical interconnects to silicon chips," *Proceedings of the IEEE*, vol. 97, pp. 1166–1185, July 2009.

[48] A. V. Krishnamoorthy, R. Ho, X. Zheng, H. Schwetman, J. Lexau, P. Koka, G. Li, I. Shubin, and J. E. Cunningham, "Computer systems based on silicon photonic interconnects," *Proceedings of the IEEE*, vol. 97, pp. 1337–1361, July 2009.

[49] A. Vahdat, H. Liu, X. Zhao, and C. Johnson, "The emerging optical data center," in *Optical Fiber Communication Conference/National Fiber Optic Engineers Conference 2011*, p. OTuH2, Optical Society of America, 2011.

[50] G. Wang, D. G. Andersen, M. Kaminsky, K. Papagiannaki, T. E. Ng, M. Kozuch, and M. Ryan, "c-through: Part-time optics in data centers," in *Proceedings of the ACM SIGCOMM 2010 Conference*, SIGCOMM '10, (New York, NY, USA), pp. 327–338, ACM, 2010.

[51] N. Farrington, *Optics in data center network architecture*. PhD thesis, UC San Diego, 2012.

[52] A. Singh, J. Ong, A. Agarwal, G. Anderson, A. Armistead, R. Bannon, S. Boving, G. Desai, B. Felderman, P. Germano, A. Kanagala, J. Provost, J. Simmons, E. Tanda, J. Wanderer, U. Hölzle, S. Stuart, and A. Vahdat, "Jupiter rising: A decade of clos topologies and centralized control in google's datacenter network," in *Proceedings of the 2015 ACM Conference on Special Interest Group on Data Communication*, SIGCOMM '15, (New York, NY, USA), pp. 183–197, ACM, 2015.

[53] Cisco, "Data center power and cooling white paper," 2017.

[54] Oclaro, "1310nm 400gbe 2km transceiver," 2018.

[55] B. Latency and the New Data Center Network, "Compass data centers," 2016.

[56] Facebook, "Introducing data center fabric, the next-generation facebook data center network," 2014.

[57] A. Yariv and P. Yeh, *Photonics: Optical Electronics in Modern Communications*. New York, NY: Oxford University Press, 2007.

[58] R. Soref and B. Bennett, "Electrooptical effects in silicon," *IEEE Journal of Quantum Electronics*, vol. 23, pp. 123–129, January 1987.

[59] M. Papes, P. Cheben, D. Benedikovic, J. H. Schmid, J. Pond, R. Halir, A. O.-M. nux, G. Wangüemert-Pérez, W. N. Ye, D.-X. Xu, S. Janz, M. Dado, and V. Vašinek, "Fiber-chip edge coupler with large mode size for silicon photonic wire waveguides," *Opt. Express*, vol. 24, pp. 5026–5038, Mar 2016.

[60] R. Marchetti, C. Lacava, A. Khokhar, X. Chen, I. Cristiani, D. J. Richardson, G. T. Reed, P. Petropoulos, and P. Minzioni, "High-efficiency grating-couplers: Demonstration of a new design strategy," *Scientific Reports*, vol. 7, no. 1, pp. 1–8, 2017.

[61] M. R. Watts, W. A. Zortman, D. C. Trotter, G. N. Nielson, D. L. Luck, and R. W. Young, "Adiabatic resonant microrings (arms) with directly integrated thermal microphotonics," in *2009 Conference on Lasers and Electro-Optics and 2009 Conference on Quantum electronics and Laser Science Conference*, pp. 1–2, June 2009.

[62] M. R. Watts, J. Sun, C. DeRose, D. C. Trotter, R. W. Young, and G. N. Nielson, "Adiabatic thermo-optic mach-zehnder switch," *Opt. Lett.*, vol. 38, pp. 733–735, Mar 2013.

[63] N. Sherwood-Droz, H. Wang, L. Chen, B. G. Lee, A. Biberman, K. Bergman, and M. Lipson, "Optical 4×4 hitless silicon router for optical networks-on-chip (noc)," *Opt. Express*, vol. 16, pp. 15915–15922, Sep 2008.

[64] N. Dupuis, B. G. Lee, A. V. Rylyakov, D. M. Kuchta, C. W. Baks, J. S. Orcutt, D. M. Gill, W. M. J. Green, and C. L. Schow, "Modeling and characterization of a nonblocking 4×4 mach-zehnder silicon photonic switch fabric," *Journal of Lightwave Technology*, vol. 33, pp. 4329–4337, Oct 2015.

[65] Z. Su, E. Timurdogan, J. Sun, M. Moresco, G. Leake, D. D. Coolbaugh, and M. R. Watts, "An interior-ridge silicon microring switch with integrated thermal tuner," in *Advanced Photonics 2015*, p. IM2B.5, Optical Society of America, 2015.

[66] N. Dupuis, B. G. Lee, A. V. Rylyakov, D. M. Kuchta, C. W. Baks, J. S. Orcutt, D. M. Gill, W. M. J. Green, and C. L. Schow, "Modeling and characterization of a nonblocking 4×4 mach-zehnder silicon photonic switch fabric," *Journal of Lightwave Technology*, vol. 33, pp. 4329–4337, Oct 2015.

[67] K. Suzuki, G. Cong, K. Tanizawa, S.-H. Kim, K. Ikeda, S. Namiki, and H. Kawashima, "Ultra-high-extinction-ratio 2×2 silicon optical switch with variable splitter," *Opt. Express*, vol. 23, pp. 9086–9092, Apr 2015.

[68] N. Dupuis, A. V. Rylyakov, C. L. Schow, D. M. Kuchta, C. W. Baks, J. S. Orcutt, D. M. Gill, W. M. J. Green, and B. G. Lee, "Nanosecond-scale mach zehnder-based cmos photonic switch fabrics," *Journal of Lightwave Technology*, vol. 35, pp. 615–623, Feb 2017.

[69] A. W. Poon, X. Luo, F. Xu, and H. Chen, "Cascaded microresonator-based matrix switch for silicon on-chip optical interconnection," *Proceedings of the IEEE*, vol. 97, pp. 1216–1238, July 2009.

[70] X. Luo, J. Song, S. Feng, A. W. Poon, T.-Y. Liow, M. Yu, G.-Q. Lo, and D.-L. Kwong, "Silicon High-Order Coupled-Microring-Based Electro-Optical Switches for On-Chip Optical Interconnects," *IEEE Photonics Technology Letters*, vol. 24, pp. 821–823, may 2012.

[71] I.-T. R. G.694.1, "Spectral grids for wdm appications: Dwdm frequency grid," *Internation Telecommunication Union*, 2012.

[72] J. K. S. Poon, J. Scheuer, S. Mookherjea, G. T. Paloczi, Y. Huang, and A. Yariv, "Matrix analysis of microring coupled-resonator optical waveguides," *Opt. Express*, vol. 12, pp. 90–103, Jan 2004.

[73] R. Aguinaldo, H. Grant, C. Derose, D. Trotter, A. Pomerene, A. Starbuck, A. Lentine, and S. Mookherjea, "Silicon photonic integrated components for add, drop, and voa in a 4-channel data-center network," in *2014 IEEE Photonics Conference*, pp. 1–2, Oct 2014.

[74] F. Doany, B. Lee, S. Assefa, W. Green, M. Yang, C. Schow, C. V. Jahnes, S. Zhang, J. Singer, V. Kopp, J. Kash, and Y. Vlasov, "Multichannel high-bandwidth coupling of ultradense silicon photonic waveguide array to standard-pitch fiber array," *J. Lightwave Technol.*, vol. 29, pp. 475–482, Feb 2011.

[75] T. Baehr-Jones, T. Pinguet, S. Lo Guo-Qiang, P. andd Danziger, D. Prather, and M. Hochberg, "Myths and rumors of silicon photonics," *Nature Photonics*, vol. 8, pp. 579–582, 2014.

[76] G. Betts, L. Walpita, W. Chang, and R. Mathis, "On the linear dynamic range of integrated electrooptical modulators," *IEEE Journal of Quantum Electronics*, vol. 22, pp. 1009–1011, Jul 1986.

[77] C. T. Lin, J. Chen, S. P. Dai, P. C. Peng, and S. Chi, "Impact of nonlinear transfer function and imperfect splitting ratio of mzm on optical up-conversion employing double sideband with carrier suppression modulation," *Journal of Lightwave Technology*, vol. 26, pp. 2449–2459, Aug 2008.

[78] C. M. Sorace, A. Khilo, and F. Kaertner, "Broadband linear silicon mach-zender modulators," in *Integrated Photonics Research, Silicon and Nanophotonics and Photonics in Switching*, p. IWA4, Optical Society of America, 2010.

[79] F. Xia, L. Sekaric, and Y. Vlasov, "Mode conversion losses in silicon-on-insulator photonic wire based racetrack resonators," *Opt. Express*, vol. 14, pp. 3872–3886, May 2006.

[80] J. Scheuer, "Fabrication and characterization of low-loss polymeric waveguides and micro-resonators," in *Integrated Photonics and Nanophotonics Research and Applications / Slow and Fast Light*, p. ITuA3, Optical Society of America, 2007.

[81] W. R. McKinnon, D.-X. Xu, C. Storey, E. Post, A. Densmore, A. Delâge, P. Waldron, J. H. Schmid, and S. Janz, "Extracting coupling and loss coefficients from a ring resonator," *Opt. Express*, vol. 17, pp. 18971–18982, Oct 2009.

[82] R. Aguinaldo, Y. Shen, and S. Mookherjea, "Large dispersion of silicon directional couplers obtained via wideband microring parametric characterization," *IEEE Photonics Technology Letters*, vol. 24, pp. 1242–1244, July 2012.

[83] M. A. Tran, T. Komljenovic, J. C. Hulme, M. L. Davenport, and J. E. Bowers, "A robust method for characterization of optical waveguides and couplers," *IEEE Photonics Technology Letters*, vol. 28, pp. 1517–1520, July 2016.

[84] A. Yariv and P. Yeh, *Photonics: Optical Electronics in Modern Communications (The Oxford Series in Electrical and Computer Engineering)*. New York, NY, USA: Oxford University Press, Inc., 2006.

[85] I. . MathWorks, "lsqnonlin (r2017a)," 2017.

[86] F. E. Doany, B. G. Lee, S. Assefa, W. M. J. Green, M. Yang, C. L. Schow, C. V. Jahnes, S. Zhang, J. Singer, V. I. Kopp, J. A. Kash, and Y. A. Vlasov, "Multichannel high-bandwidth coupling of ultradense silicon photonic waveguide array to standard-pitch fiber array," *Journal of Lightwave Technology*, vol. 29, pp. 475–482, Feb 2011.

[87] M. Pillmeier, "Barrel shifter design, optimization, and analysis," Master's thesis, Lehigh University, 2001.

[88] J. Palmer, B. W. Ravenel, and R. Nave, "Numeric data processor," July 1982. U.S. Patent 4,338,675.

[89] H. Niimi, "Barrel shifter circuit having rotation function," October 1992. U.S. Patent 5,155,698.

[90] E. Nishimura, "Barrel shifter," November 1995. U.S. Patent 5,465,223.

[91] H. Steel, *Interferometry*. New York, NY: Cambridge University Press, 1983.

[92] A. Cordero-Davila, J. Pedraza-Contreras, O. Cardona-Nunez, and A. Cornejo-Rodriguez, "Cyclic interferometers for optical testing," *Applied Optics*, vol. 22, no. 16, pp. 2478–2480, 1983.

[93] A. Lohmann, W. Stork, and G. Stucke, "Optical perfect shuffle," *Applied Optics*, vol. 25, no. 10, pp. 15130–1531, 1986.

[94] A. Ghosh, "Cyclic shifter: an all-optical implementation," *Applied Optics*, vol. 27, no. 27, pp. 4166–4167, 1988.

[95] K. Brenner and A. W. Lohmann, "Cyclic shifting for optical data processing," *Applied Optics*, vol. 27, no. 3, pp. 434–436, 1988.

[96] J. Jahns and W. Dschner, "Optical cyclic shifter using diffractive lenslet arrays," *Optics Communications*, vol. 79, no. 6, pp. 407–410, 1990.

[97] J. Jahns, "Integrated optical imaging system," *Applied Optics*, vol. 29, no. 14, pp. 1998–1998, 1990.

[98] P. Ramamoorthy, G. Govind, and S. Antony, "Optical implementation of systolic finite impulse response filters," *Optical Engineering*, vol. 26, no. 11, pp. 1169–1174, 1987.

[99] C. Chalfant, R. F. Kalman, and J. W. Goodman, "A sixteen channel acousto-fiber-optic barrel shifter," in *Proc. SPIE 2481, Photonic Device Engineering for Dual-Use Applications*, 1995. doi: 10.1117/12.212704.

[100] M. Georgas, J. Leu, B. Moss, C. Sun, and V. Stojanovi, "Addressing link-level design tradeoffs for integrated photonic interconnects," in *2011 IEEE Custom Integrated Circuits Conference (CICC)*, pp. 1–8, Sept 2011.

[101] E. Timurdogan, C. M. Sorace-Agaskar, S. J., E. S. Hosseini, A. Biberman, and M. R. Watts, "An ultralow power athermal silicon modulator," *Nature Communications*, vol. 5, no. 4008, 2014. 10.1038/ncomms5008.

[102] S. J. Emelett and R. Soref, "Design and simulation of silicon microring optical routing switches," *Journal of Lightwave Technology*, vol. 23, pp. 1800–1807, April 2005.

[103] X. Wang, A. Lentine, C. DeRose, A. L. Starbuck, D. Trotter, A. Pomerene, and S. Mookherjea, "Wide-range and fast thermally-tunable silicon photonic microring resonators using the junction field effect," *Opt. Express*, vol. 24, pp. 23081–23093, Oct 2016.

[104] T. S. El-Bawab, *Optical Switching*. Berlin, Heidelberg: Springer-Verlag, 2006.

[105] E. Shiles, T. Sasaki, M. Inokuti, and D. Y. Smith, "Self-consistency and sum-rule tests in the kramers-kronig analysis of optical data: Applications to aluminum," *Phys. Rev. B*, vol. 22, pp. 1612–1628, Aug 1980.

[106] L. Lu, S. Zhao, L. Zhou, D. Li, Z. Li, M. Wang, X. Li, and J. Chen, "16 x 16 non-blocking silicon optical switch based on electro-optic mach-zehnder interferometers," *Opt. Express*, vol. 24, pp. 9295–9307, May 2016.

[107] Y. Ma, Y. Zhang, S. Yang, A. Novack, R. Ding, A. E.-J. Lim, G.-Q. Lo, T. Baehr-Jones, and M. Hochberg, "Ultralow loss single layer submicron silicon waveguide crossing for soi optical interconnect," *Opt. Express*, vol. 21, pp. 29374–29382, Dec 2013.

[108] Y. Zhang, A. Hosseini, X. Xu, D. Kwong, and R. T. Chen, "Ultralow-loss silicon waveguide crossing using bloch modes in index-engineered cascaded multimode-interference couplers," *Opt. Lett.*, vol. 38, pp. 3608–3611, Sep 2013.

[109] Y. Liu, J. M. Shainline, X. Zeng, and M. A. Popović, "Ultra-low-loss cmos-compatible waveguide crossing arrays based on multimode bloch waves and imaginary coupling," *Opt. Lett.*, vol. 39, pp. 335–338, Jan 2014.

[110] N. Dupuis and B. G. Lee, "Impact of topology on the scalability of mach-zehnder-based multistage silicon photonic switch networks," *Journal of Lightwave Technology*, vol. 36, pp. 763–772, Feb 2018.

[111] K. Padmaraju and K. Bergman, "Resolving the thermal challenges for silicon microring resonator devices," *Nanophotonics*, vol. 3, no. 4-5, pp. 269–281, 2014.

[112] S. Namnabat, K.-J. Kim, A. Jones, R. Himmelhuber, C. T. DeRose, D. C. Trotter, A. L. Starbuck, A. Pomerene, A. L. Lentine, and R. A. Norwood, "Athermal silicon optical add-drop multiplexers based on thermo-optic coefficient tuning of sol-gel material," *Opt. Express*, vol. 25, pp. 21471–21482, Sep 2017.

[113] J. S. Lee, L. Carroll, C. Scarcella, N. Pavarelli, S. Menezo, S. Bernab, E. Temporiti, and P. O'Brien, "Meeting the electrical, optical, and thermal design challenges of photonic-packaging," *IEEE Journal of Selected Topics in Quantum Electronics*, vol. 22, pp. 409–417, Nov 2016.

[114] T. F. O. Association, "The fiber optic association - tech topics," 2015.

[115] S. Shibata, S. Mitachi, and S. Takahashi, "High numerical aperture multicomponent glass fiber," *Appl. Opt.*, vol. 19, pp. 1484–1488, May 1980.

[116] F. F. Roberts, "Topical meeting on optical fibre transmission ii — williamsburg, 22–24 february 1977," in *Optical Fiber Transmission II Technical Digest*, p. ThA3, Optical Society of America, 1977.

[117] Nufern, "Uhna-7 fiber," 2016.

[118] E. Murphy and T. Rice, "Low-loss coupling of multiple fiber arrays to single-mode waveguides," *Journal of Lightwave Technology*, vol. 1, pp. 479–482, September 1983.

[119] K. E. Petersen, "Silicon as a mechanical material," *Proceedings of the IEEE*, vol. 70, pp. 420–457, May 1982.

[120] C. M. Schroeder, "Accurate silicon spacer chips for an optical fiber cable connector," in *Optical Fiber Transmission II Technical Digest*, p. WA6, Optical Society of America, 1977.

[121] J. V. Campenhout, W. M. J. Green, and Y. A. Vlasov, "Design of a digital, ultra-broadband electro-optic switch for reconfigurable optical networks-on-chip," *Opt. Express*, vol. 17, pp. 23793–23808, Dec 2009.

[122] H. W. Icenogle, B. C. Platt, and W. L. Wolfe, "Refractive indexes and temperature coefficients of germanium and silicon," *Appl. Opt.*, vol. 15, pp. 2348–2351, Oct 1976.